Pristine and Doped Titanium Dioxide Studied by NC-AFM

Dissertation
to fulfill the requirements
for obtaining a PhD degree in physics
(Dr. rer. nat.)

by
Ralf Bechstein

Submitted to Fachbereich Physik

UNIVERSITÄT OSNABRÜCK

January 09, 2009

The PhD study has been carried out under the supervision of Angelika Kühnle at the Universität Osnabrück from February 2006 to January 2009.

Doctoral Advisor	Angelika Kühnle
2^{nd} Referee	Rubén Pérez

Submitted	09.01.2009
Oral Exam	26.01.2009

For Stefanie.

Contents

1 Introduction **1**

2 Experimental section **3**
- 2.1 NC-AFM basics 3
- 2.2 Improvement of the microscope 7
- 2.3 Scan regime and data processing 17

3 Rutile titanium dioxide **25**
- 3.1 Introduction to rutile TiO2(110) 25
- 3.2 Rutile TiO2(110) imaged by NC-AFM 29
  - 3.2.1 Hole mode and protrusion mode 30
  - 3.2.2 Neutral mode and all-inclusive mode 32

4 Doped titanium dioxide **41**
- 4.1 Chromium-doped TiO2(110) 43
- 4.2 TiO2(110) codoped with chromium and antimony 51
- 4.3 Antimony-doped TiO2(110) 61

5 Conclusion **69**

References **73**

Publications **79**

Conference contributions **81**

Acknowledgements **83**

1 Introduction

Titanium dioxide is a non-toxic, well-established and widely-used material. It consists of two elements only and exists in very stable forms, namely rutile, anatase and brookite.
Millions of tons of pigmentary TiO_2 are consumed annually worldwide to provide whiteness and opacity to products such as paints, coatings, plastics, papers, inks, pharmaceuticals as well as most toothpastes. Titania is used as corrosion-protective coating, optical coating, biocompatibility coating, and gate insulator. A detailed list of applications including references is found in [1].
Most important for the present thesis, titanium dioxide is a photocatalyst [2]. It is used for photo-assisted degradation of organic molecules, in self-cleaning coatings, in solar cells [3] and for water splitting by photoelectrolysis [4].

Titania has often been ascribed as prototypical system for transition-metal oxide surfaces or even model system for oxides in general. It became a dream of surface scientists to understand the chemistry at oxide surfaces in general by simply understanding the surface of titania.

"The surfaces of TiO_2 in particular have been studied in detail as they represent model systems with which to explore the physics and chemistry of oxide surfaces."
(Pang, 1998 [5])

The (110) surface of rutile titania is the most stable face and is, therefore, the most intensively studied surface of titania.

"Titanium dioxide is the most investigated single-crystalline system in the surface science of metal oxides." (Diebold, 2002 [1])

Understanding the (110) surface of rutile titanium dioxide from direct visualization by scanning probe techniques has been the focus of numerous publications in the last decade (e.g. [6–10]) since atomic resolution on oxides became a standard in scanning probe experiments. The focus of these publications was to gain insight into the surface structure, the contrast formation with scanning probe techniques and the reactivity of the surface. For the latter, the surface has been exposed to all kinds of simple test molecules like water, oxygen, hydrogen, nitrogen, ammonia, carbon dioxide, methane, carboxylates and various others (see e.g. [2, 9, 11, 12]).
Contradictory to what might be expected from such an overwhelming amount of studies of

this "well-characterized" [1] surface, various questions, regarding the nature and reactivity of this material are still under discussion. Furthermore, understanding contrast formation in scanning probe microscopy imaging is still in its infancy.

> *"There are still a number of mysteries regarding the exact nature of structure and reactivity at the surface. Many of these mysteries will be solved in the next few years, only to reveal deeper mysteries within the heart of this wonderful substance."*
> *(Bowker, 2006 [13])*

The present thesis reports on a non-contact atomic force microscopy (NC-AFM) study of the rutile titanium dioxide (110) surface. Contrast formation in NC-AFM imaging will be the focus of the first part, where atomically resolved images in various contrast modes are presented and discussed with respect to the tip-sample interaction mechanisms behind these contrasts.

In the second part of the thesis, I report on a first approach in imaging transition-metal-doped titanium dioxide with high-resolution NC-AFM. The influence of chromium and antimony doping on the surface structure of $TiO_2(110)$ at the atomic scale is discussed in detail. This is a step towards more realistic, application-oriented systems as chromium and antimony codoped titania is a very promising photocatalyst, sensitized for visible light.

2 Experimental section

In this study, I used NC-AFM operated in the so-called frequency-modulation mode. This chapter gives a brief introduction to the technique. A complete description of AFM [14] can be found elsewhere [15]. Furthermore, I will present essential improvements of our AFM setup that I performed to achieve utmost resolution.
Finally, general remarks on the scanning regime and data processing are given.

2.1 NC-AFM basics

NC-AFM is a scanning probe technique where a nanoscopic tip mounted at the end of an oscillating cantilever is used to probe forces. In the frequency-modulation mode (FM-AFM) the cantilever is driven at its current eigenfrequency while the oscillation amplitude is kept constant [16]. In close proximity to the surface, forces acting between tip and sample shift the eigenfrequency of the cantilever. This shift of the eigenfrequency (hereafter referred to as detuning or df) can be directly used as an imaging signal when scanning the cantilever at a fixed tip-surface distance (constant-height mode). Alternatively, the detuning can be kept constant to measure the height profile of equal detuning (referred to as topography).

Forces

"Non-contact" in the context of NC-AFM means that the cantilever movement can be described as weakly disturbed harmonic oscillator, even in close proximity to the surface [17]. Therefore, the magnitude of the forces between tip and sample $F_{ts}^{\max}$ must be small compared to the absolute value of the restoring force F_{r} of the cantilever

$$F_{ts}^{\max} \ll F_{\mathrm{r}} = k \cdot A \tag{2.1}$$

where A is the amplitude and k the spring constant of the cantilever. Typically, the forces acting between tip and sample are classified by their decay length. Long-range forces like van-der-Waals or electrostatic interactions are often a composition of the interaction of numerous atoms of both, tip and surface. Usually, these forces are not responsible for true atomic resolution as they average over a rather large surface area. In contrast, the main contribution to short-range forces ideally originates from the interaction of the last tip atom with the first surface atom. Thus, probing short-range forces is essential for achieving true atomic resolution. However, in the absence of short-range chemical interactions, atomic resolution has been obtained based on electrostatic [18] or van-der-Waals interaction [19, 20] solely. Short-range forces result from chemical interaction due to overlap of electronic orbitals. A detailed compendium of relevant forces can be found in [21].
Long-range van-der-Waals forces can be reduced by using atomically sharp tips with a

rather small curvature radius. This is only achieved by chance, as one has no direct influence on the nanoscopic structure of the tip. Long-range electrostatic potentials can be compensated by applying an adequate bias voltage to the tip (Kelvin probe technique) as described in [22].
The challenge in NC-AFM measurements is to approach the tip close enough to the surface to probe short-range forces - at best without undesired disturbance of the investigated system and at least without leaving the harmonic regime of cantilever movement.

Detuning

In each distance regime, attractive and repulsive forces may exist, which superimpose to form a tip-specific total force-distance curve $F_{ts}(z)$ at each surface point. From this force-distance curve the detuning at each tip-sample distance can be obtained by a simple weighted integration according to

$$df(z) = -\frac{f_0}{\pi k A^2} \int_{-A}^{A} F_{ts}(q+z+A) \cdot \frac{q}{\sqrt{A^2 - q^2}} \, \mathrm{d}q \tag{2.2}$$

where f_0 is the eigenfrequency of the unperturbed cantilever and z the lower turning point of the cantilever [17,23]. A realistic example based on a Morse potential is given in Fig. 2.1. Here, the detuning has been calculated[1] from the force-distance curve using Eq. 2.2 and typical parameters from the experiment ($f_0 = 300\,\mathrm{kHz}$, $k = 40\,\frac{\mathrm{N}}{\mathrm{m}}$ and $A = 10\,\mathrm{nm}$).

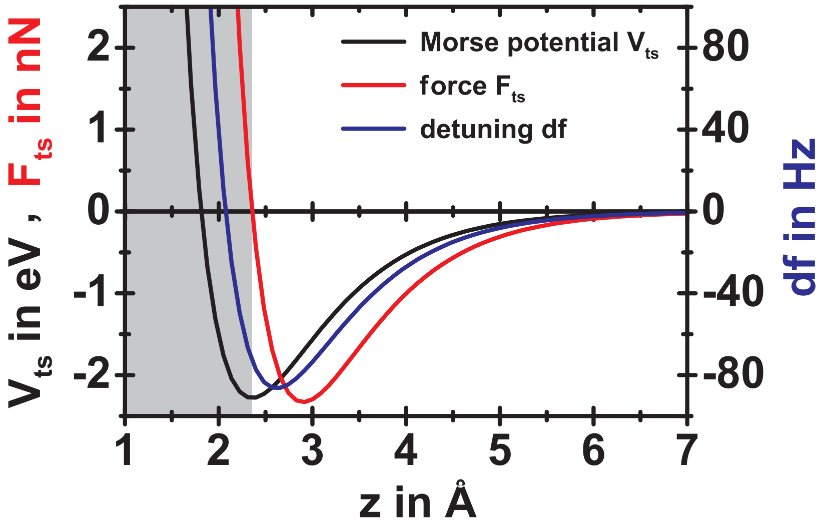

Figure 2.1: *Example of a tip-sample interaction potential V_{ts} (Morse potential for two silicon atoms with parameters as proposed in [24]), force F_{ts} and resulting detuning df. The detuning is obtained according to Eq. 2.2 using typical parameters from the experiment ($f_0 = 300\,kHz$, $k = 40\,\frac{N}{m}$ and $A = 10\,nm$). The region of repulsive interaction is marked by a grey box.*

Note that df is negative as long as the tip does not leave the attractive regime. However, higher negative detuning does neither mean higher attractive interaction, nor does it guarantee exclusively attractive interaction. Therefore, data interpretation can become rather delicate. A detailed discussion of this issue can be found in [25].

---

[1] calculations carried out by P. Rahe, Universität Osnabrück, Osnabrück (2008)

Feedback loops

The detection system will be described in Sec. 2.2. Here, I will only discuss the measuring signals in NC-AFM experiments. The original measuring signal in NC-AFM is the oscillation signal U_{osc}, representing the cantilever oscillation. Three feedback loops are needed for NC-AFM operation (see Fig. 2.2):

- The **amplitude feedback loop**, which determines the amplitude of the oscillation signal (hereafter referred to as amplitude signal; i.e. **not** the physical amplitude of the cantilever) and keeps it constant at a certain setpoint A_{setpoint}.
- The **phase-locked loop** (PLL), which ensures that the cantilever is excited at its current eigenfrequency.
- The **distance feedback loop**, which regulates the tip-sample distance to maintain df constant at a given setpoint $\mathrm{df}_{\mathrm{setpoint}}$.

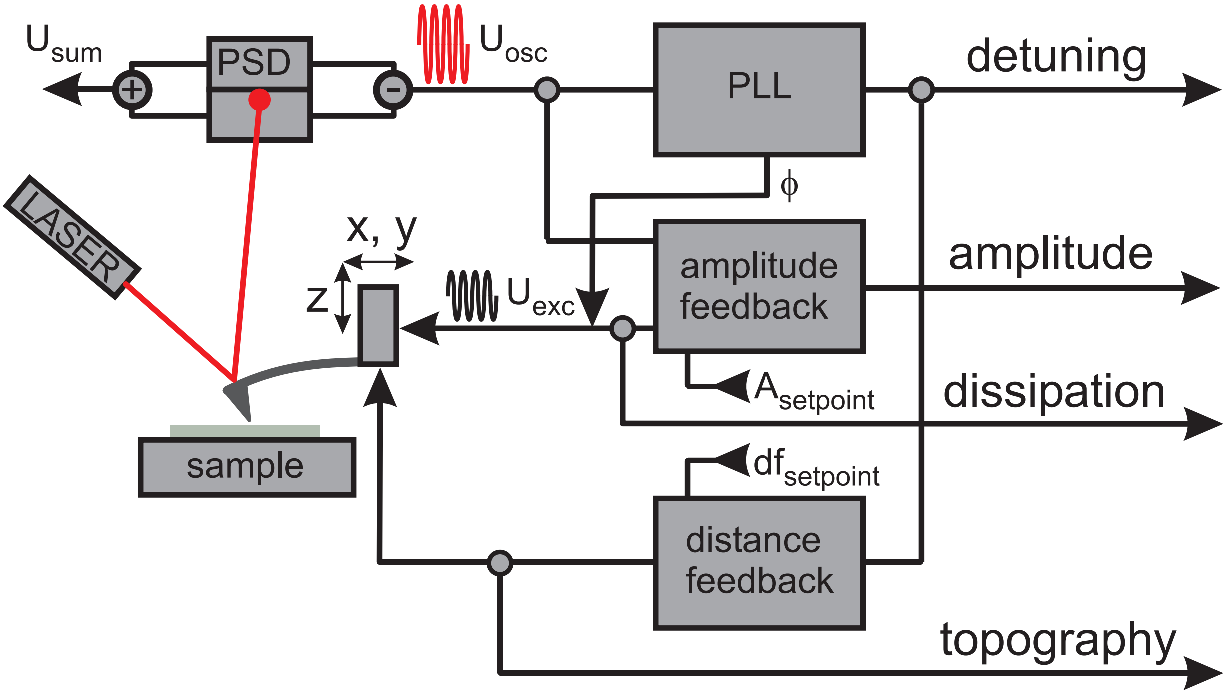

Figure 2.2: *Scheme of the interaction of the three feedback loops in NC-AFM. Description is given in the text. A detailed description of the signal detection at the photo-sensitive diode (PSD; see also Fig. 2.3) follows in Sec. 2.2.*

The PLL determines the frequency f of the oscillation signal. Comparing this frequency to the eigenfrequency of the freely oscillating cantilever f_0, the PLL generates the detuning according to

$$df = f - f_0 \; . \tag{2.3}$$

This is the primary imaging signal in NC-AFM.

The distance feedback loop settings determine whether the information about tip-sample interaction is given in the topography signal (fast distance feedback loop settings ⇒ constant detuning mode) or in the detuning signal (distance feedback loop switched off ⇒ constant height mode).

Amplitude feedback and PLL together provide an excitation signal U_{exc} of adequate amplitude and phase to excite the cantilever oscillation. The amplitude of the excitation signal is a direct measure for the energy lost due to friction in the cantilever and by dissipative tip-sample interaction. Hence, it is called dissipation signal Γ and can be scaled assuming that the dissipation signal of the unperturbed cantilever Γ_0 is caused by internal friction of the freely oscillating cantilever solely [26]. Then, the energy dissipated per oscillation cycle due to dissipative tip-sample interaction can be calculated from the dissipation signal via

$$E_{ts} = \left(\frac{\Gamma}{\Gamma_0} - 1\right)\frac{\pi k A^2}{Q} \tag{2.4}$$

where Q is the quality factor of the cantilever.

Thus, the following signals are typically recorded simultaneously in NC-AFM experiments:

- detuning signal
- topography signal
- dissipation signal
- amplitude signal (amplitude of the oscillation signal)

Remarks concerning feedback loop settings

The striking advantage of FM-AFM operated in constant-height compared to constant-detuning mode is easy data interpretation. As long as the amplitude is kept constant and as long as the cantilever is a weakly disturbed harmonic oscillator, the detuning is the result of a simple weighted integration of the total conservative force (Eq. 2.2). Thus, potentials derived from theoretical calculations can be directly compared to experimental data. In addition, changes in the dissipation signal represent a direct measure of the dissipated energy (Eq. 2.4) and hence of dissipative tip-sample interaction.

Constant-height mode and constant-detuning mode are extreme cases that are in fact not accessible in the experiment. Constant-detuning mode would require an instantaneously reacting feedback loop. As every real feedback loop needs a finite reaction time, true constant-detuning results cannot be obtained. On the other hand, measurements in constant height mode (disabled distance feedback loop) are only suitable for flat, step-free surfaces and require a non-tilted sample as well as zero drift in z direction. Hence, to simply disable the distance feedback loop does not guarantee that the tip-sample distance actually remains constant.

In reality, every microscope is operated somewhere in between.

2.2 Improvement of the microscope

All measurements presented in this thesis are performed at room temperature in an ultra-high vacuum (UHV) system (see Fig. 2.4(a)) consisting of a chamber for sample preparation, a load-lock chamber and the AFM chamber. The typical base pressure was below 10^{-10} mbar.

Omicron setup and initial performance

Microscope The microscope is a commercial VT AFM 25 from Omicron (Omicron NanoTechnology GmbH, Taunusstein, Germany). In this setup, the upside-down fixed sample is probed by a cantilever, which is scanned over the surface. The cantilever is mounted to a piezo-tube scanner as shown in Fig. 2.4(b). The silicon cantilever with the upwards pointing cantilever tip at the very end is fixed to a silicon chip. This chip has to be glued to a cantilever holder, which in turn can be plugged into the scanner tube. Both, cantilevers and samples can be easily exchanged via the load-lock chamber without breaking the vacuum.

Detection system The oscillation of the cantilever is measured by the beam deflection method as introduced by Meyer et al. [27, 28] (see also Fig. 2.2). Here, a laser beam is reflected at the back side of the cantilever and sensed by a segmented[2] photo-sensitive diode (PSD). Fig. 2.3 illustrates how the photocurrents emerging from the segments of the PSD (after convertion into voltage signals) are converted into the actual signals.

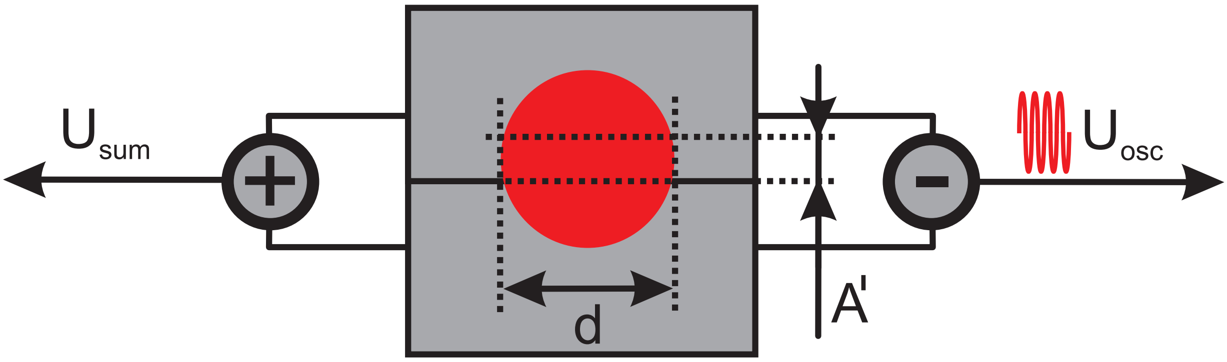

Figure 2.3: *Scheme of signal generation at the segmented PSD. The sum signal U_{sum} is derived by adding the signals from all segments, while the oscillation signal U^0_{osc} is the difference of the signals from top and bottom segment.*

The sum signal is proportional to the total light intensity detected by all segments of the PSD. Assuming a constant light power density p as well as a circular spot profile, the sum signal can be calculated by

$$U_{\mathrm{sum}} = \frac{\pi}{4} d^2 \cdot p \; . \tag{2.5}$$

---

[2] In the VT AFM 25 a quartered PSD is used, allowing for simultaneous detection of normal and lateral cantilever motion. As I never recorded lateral forces during my PhD study, I restrict this discussion to a halved PSD for simplicity.

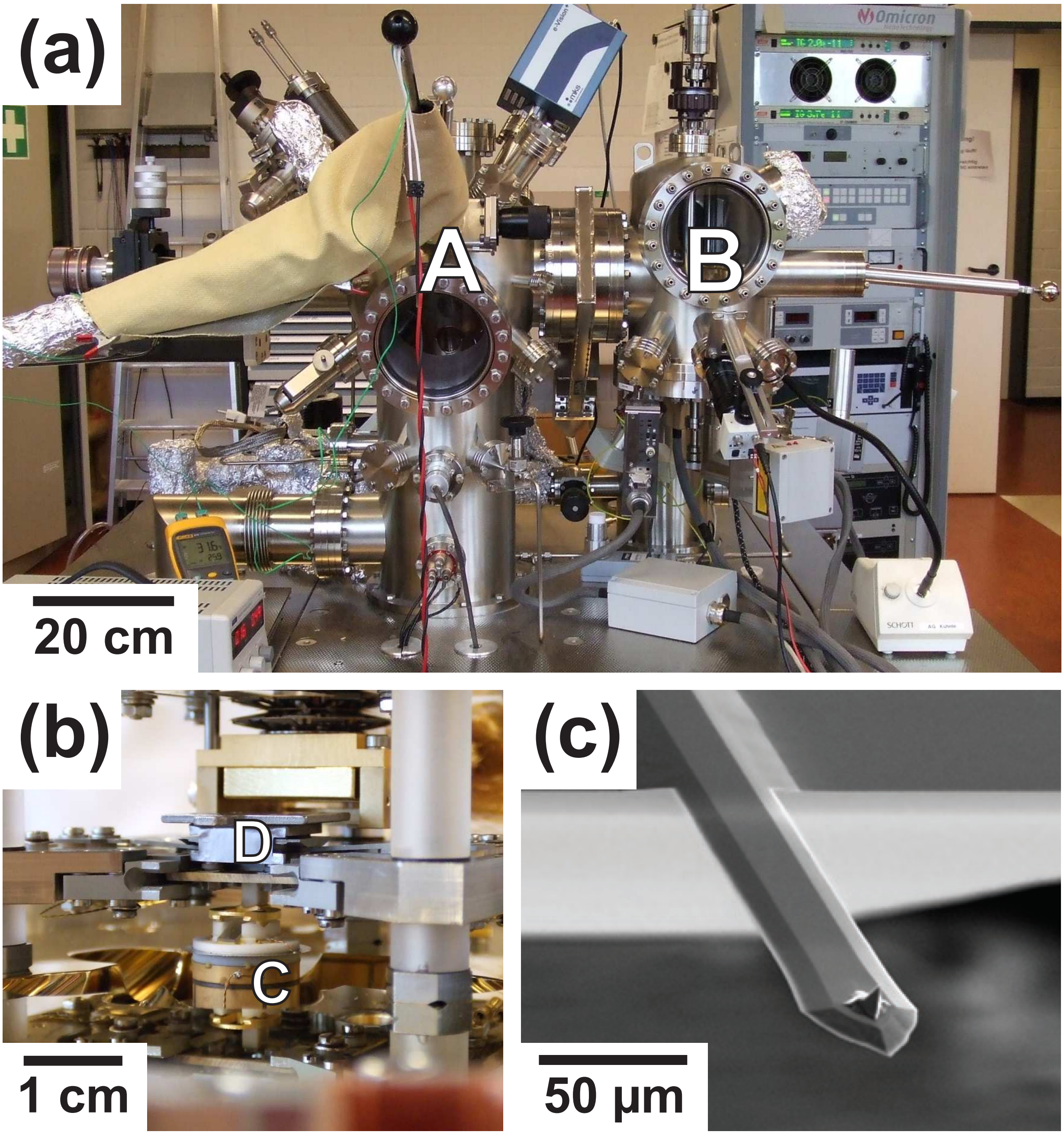

Figure 2.4: *Photographs of the entire UHV system (a) and the AFM (b). The system consists of a chamber for sample preparation (A), a load-lock chamber (at the backside) and the AFM chamber (B). The AFM consists of a piezo-tube scanner (C) carrying the cantilever chip with the cantilever tip pointing upwards. The sample is fixed in an upside-down positioned sample holder (D). (c) shows an electron microscopy image (courtesy of NanoWorld AG, http://www.nanoworld.com) of a silicon cantilever of NCH type as used in the present experiments. At the very end of the lever the upwards directed tip can be seen.*

The oscillation signal is derived by substraction of the signals from the two segments. Note that the oscillation signal is not normalized by division by the sum signal U_{sum} as sometimes applied in other systems. The advantage of the present setting is avoiding crosstalk of noise from the sum signal. The disadvantage is the dependence of the amplitude calibration on the sum signal as described in the following.
When the cantilever is at its rest position, the oscillation signal equals zero. For small enough elongations, the amplitude of the oscillation signal can be estimated by

$$U^0_{\mathrm{osc}} \approx A' \cdot d \cdot p \ . \tag{2.6}$$

where A' is proportional to the amplitude A. The ratio $\frac{A}{A'}$ is a fixed value for each microscope depending only on the geometry of the detection system. From the equations 2.5 and 2.6 one obtains the following relation

$$A' \approx \frac{\pi}{4} d \cdot \frac{U^0_{\mathrm{osc}}}{U_{\mathrm{sum}}} \tag{2.7}$$

between A', amplitude signal U^0_{osc} and sum signal U_{sum}. The amplitude signal can be calibrated as described e.g. in [29]. Note that each calibration is only valid for a fixed sum signal.

Performance The final installation of the system was completed by the end of February 2006. The image shown in Fig. 2.5 obtained on March 2nd 2006 depicts a typical example of the microscope performance in the setup proposed by Omicron (for parameters see Tab. 2.1).

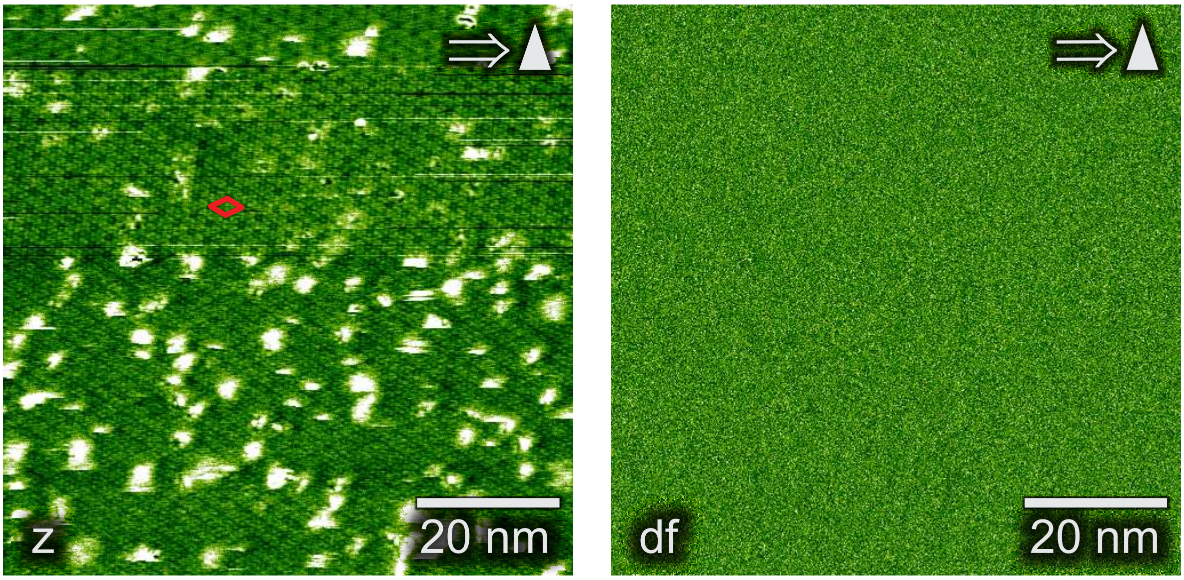

Figure 2.5: *Topography (z) and detuning (df) image of the Si(111)(7 × 7) surface [30] obtained in constant-detuning mode at a detuning setpoint of about -40 Hz. In the topography signal the unit cell (marked by a red rhombus) is clearly resolved. The corner holes are visible as well as a large number of bright flakes, which are dirt. In the detuning signal nothing can be identified but noise. The histogram of the df image is given in Fig. 2.6.*

A Si(111)(7 × 7) surface [30] has been investigated in constant-detuning mode. Corner holes are clearly resolved in the topography signal. In the detuning signal nothing but noise is visible. Thus, this image is appropriate to estimate the noise level of the detuning signal. In Fig. 2.6 a histogram of the detuning image presented in Fig. 2.5 is shown.

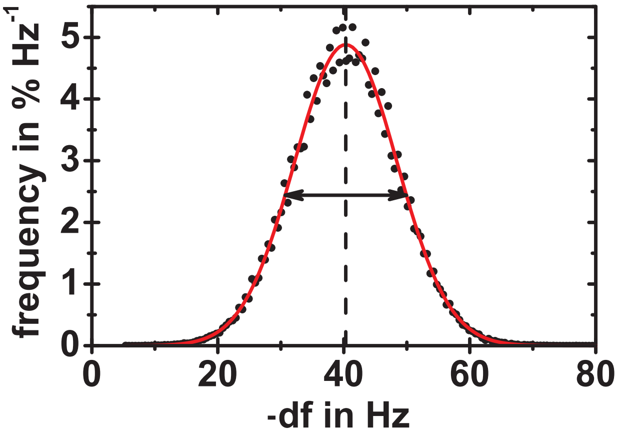

Figure 2.6: *Histogram of the detuning image of Fig. 2.5 recorded in the Omicron setup. The values of df are in good approximation normally distributed around the detuning setpoint of -40 Hz (dashed line) as indicated by the Gaussian bell curve fit (red line). The full width at half maximum (FWHM) was estimated to approximately 20 Hz (indicated by the arrow).*

The values of df are in good approximation normally distributed around the detuning setpoint and can therefore be fitted to a Gaussian curve. The full width at half maximum (FWHM) was estimated to approximately 20 Hz. This detuning variation is an appropriate measure of the noise level in the detuning signal.

In NC-AFM one intends to measure detunings of a few up to several -10 Hz. However, the *difference* in the detuning between certain surface sites (hereafter referred to as corrugation), which eventually gives the imaging contrast, is typically in the order of a few hertz or even below. If one aims at utmost resolution, a detuning noise level of less than 1 Hz is an absolute prerequisite.

Improvements

To understand and eventually eliminate the sources of noise in the instrument, the whole pathway of the measurement signal from its origin in the light unit to the output of the PLL has to be checked. Both, noise decrease and signal increase will be taken into account to eventually increase the signal-to-noise ratio (SNR).

It has to be mentioned that the instrument is very well protected against disturbances from acoustics or vibrations of the laboratory. The whole system is placed on damping legs and the AFM itself is suspended on springs and additionally protected by an eddy-current damping. Furthermore, all pumps using moving parts are usually switched off during measurement.

Light unit Stability of the light source is essential as the oscillation amplitude is inversely proportional to the sum signal[3] (see Eq. 2.7). The light unit of the VT AFM 25 most likely contains a laser diode or a superluminescence diode emitting in near infrared regime, although it is not specified in the manual. I measured the output power at the end of the fiber to be 820 µW at maximum. The output power is regulated by a software controller. The setpoint is called "intensity". The output power as function of "intensity" is depicted in Fig. 2.7. Besides, also the resulting sum signal in dependence on the used cantilever type is shown.

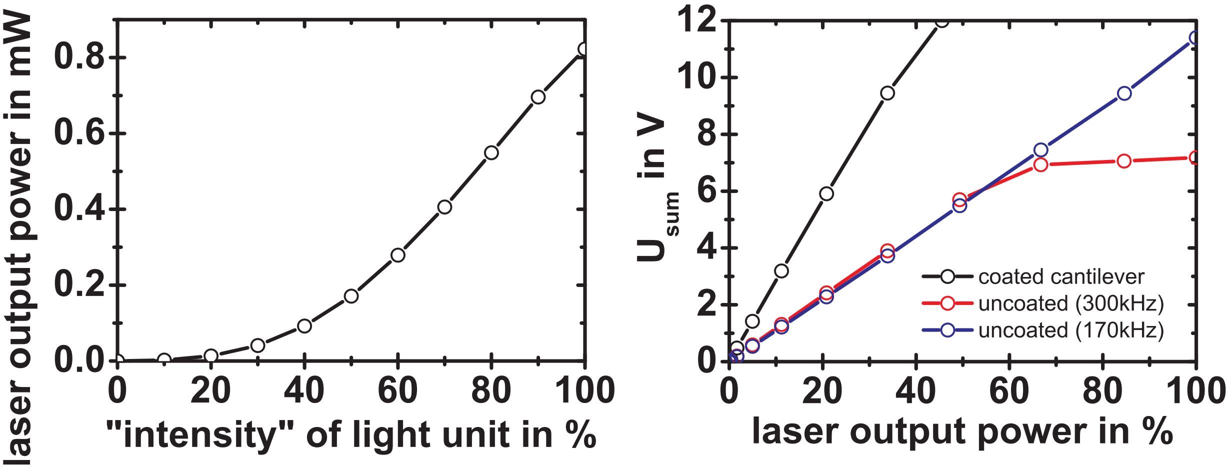

Figure 2.7: *Output power of the light unit in dependence on the "intensity" defined in the software (left). Resulting sum signal depending on the output power and the used cantilever type (right). All cantilever types are made of silicon, the coating is gold. Lines are guides to the eyes.*

The observed saturation at a sum signal of about 7 V when using uncoated 300 kHz cantilevers is caused by widening of the laser spot. At high output power values an increasing fraction of the laser spot misses the cantilever. This is not seen when using the 170 kHz cantilever as this type has a larger width.

I checked the stability and the noise level of the light unit at different output powers by recording the sum signal simultaneously during test measurements for several hours. The magnitude of fluctuations was found to be always below the detection limit of 1 ‰. In particular, fluctuations are much smaller than monotonic changes due to thermal drift. However, also changes due to drift of typically less than 5 $\frac{‰}{\mathrm{h}}$ are negligible in this discussion.

Thus, to increase the SNR one should use the maximum achievable sum signal. Hence, I increased the sum signal from 3 V as proposed (Omicron) to 6 V.

Cantilever A cantilever is characterized by its stiffness k, its eigenfrequency f_0 and its quality factor Q. These values can be measured as e.g. described in [29].

The total detuning noise δf is given by

---

[3] The original light unit delivered with the instrument in November 2005 was not accepted by A. Kühnle and had to be replaced by the improved version used in the present setup. The original light unit showed severe intensity fluctuations in the order of 1 %.

$$\delta f = \sqrt{\delta f_{\mathrm{th}}^2 + \delta f_{\mathrm{ds}}^2}\,. \tag{2.8}$$

It consists of the thermal noise δf_{th} of the cantilever

$$\delta f_{\mathrm{th}} = \sqrt{\frac{2\, f_0\, k_B T\, B}{\pi\, k\, Q\, A^2}} \tag{2.9}$$

and the noise of the detection system δf_{ds}

$$\delta f_{\mathrm{ds}} = \frac{n_{\mathrm{ds}}}{\pi\, A} B^{\frac{3}{2}}\,, \tag{2.10}$$

where k_B is the Boltzmann constant, T the temperature, B the bandwidth of the detection system and n_{ds} the spectral noise density of the detection system [16, 23, 31–33]. Hence, for large enough Q values the thermal noise of the cantilever is negligible and $\delta f = \delta f_{\mathrm{ds}}$. Omicron proposed the usage of gold coated cantilevers that are characterized by an eigenfrequency of about 300 kHz, a spring constant of approximately 40 $\frac{\mathrm{N}}{\mathrm{m}}$ and a quality factor of typically 10,000. The low Q values result from additional internal friction due to the reflex coating. As demonstrated in Fig. 2.7 the light source possesses enough power to use uncoated cantilevers as well. I decided to use uncoated silicon cantilevers (type PPP-NCH) from NanoWorld[4] (Neuchâtel, Switzerland) with an eigenfrequency of about 300 kHz, a spring constant of approximately 40 $\frac{\mathrm{N}}{\mathrm{m}}$ and a quality factor of typically 30,000.

Amplitude The absolute detuning value resulting from a certain tip-sample interaction depends on the cantilever properties as well as the amplitude as can be seen in Eq. 2.2. For large amplitudes [25] a normalized frequency shift $\gamma(z)$ has been introduced by Giessibl [23], which is independent of these parameters

$$\gamma(z) = \frac{k\, A^{\frac{3}{2}}}{f_0} \cdot df(z)\,. \tag{2.11}$$

Thus, the absolute detuning is proportional to $A^{-\frac{3}{2}}$. The detuning noise δf on the other hand, is proportional to A^{-1} as can be seen from Eq. 2.9 and Eq. 2.10. Consequently, the signal-to-noise ratio for large amplitudes

$$SNR = \frac{df}{\delta f} \propto \frac{A}{A^{\frac{3}{2}}} = \frac{1}{\sqrt{A}} \tag{2.12}$$

is poportional to $A^{-\frac{1}{2}}$. However, amplitude and stiffness of the cantilever cannot be chosen independently as already denoted by Eq. 2.1. The spring constant k has to be chosen as large as possible to allow for a small amplitude. For safety, we may estimate the maximum tip-sample interaction to be less than 1 % of the restoring force F_{r}. $F_{ts}^{\max}$ is usually in the order of a few nN (see Fig. 2.1). Hence, F_{r} should be chosen to be in the range of a few 100 nN. As k was already chosen to be $\approx 40\,\frac{\mathrm{N}}{\mathrm{m}}$, I increased the amplitude from 3 nm to 10 nm, although, this in turn decreases the SNR by a factor of $\sqrt{0.3}$.

The detuning of a harmonic oscillator, resulting from a constant force gradient k_{ts} is given by $df = \frac{f_0}{2k} \cdot k_{\mathrm{ts}}$. Thus, the minimum detectable force gradient can be estimated to be

---

[4] former Nanosensors™

$$k_{\mathrm{ts}}^{\min} = \frac{2k}{f_0} \cdot \delta f \, . \tag{2.13}$$

Hence, the eigenfrequency f_0 should be as large as possible to achieve a small $k_{\mathrm{ts}}^{\min}$.

Preamplifier The preamplifier converts the photocurrent signals from the segments of the PSD (see Fig. 2.3) into the oscillation signal and the sum signal as introduced in Eq. 2.6 and 2.5, respectively. The electronics workshop[5] designed and built a new, customized preamplifier. The main improvements of the electronic design are presented in [34].

The new preamplifier has a bandpass of 300 kHz ± 50 kHz customized for the used cantilever type, while the original preamplifier has no filter to allow for a wide range of operation modes. Furthermore, the gain of the amplifier stage had to be adjusted. To allow for using an amplitude of 10 nm at a preferably high amplitude signal U_{osc}^{0} and a high sum signal U_{sum} at the same time, the gain of the preamplifier was customized (see Eq. 2.7).

Finally, the noise level at the output of the preamplifier disconnected from the microscope was reduced from about 70 mV (Omicron preamplifier) to approximately 7 mV. Taking into account the reduced gain, the SNR was increased by a factor of about 4.

We[6] measured the spectral noise density n_{ds} of the detection system with the new preamplifier in dependence on the sum signal U_{sum}. The result is shown in Fig. 2.8.

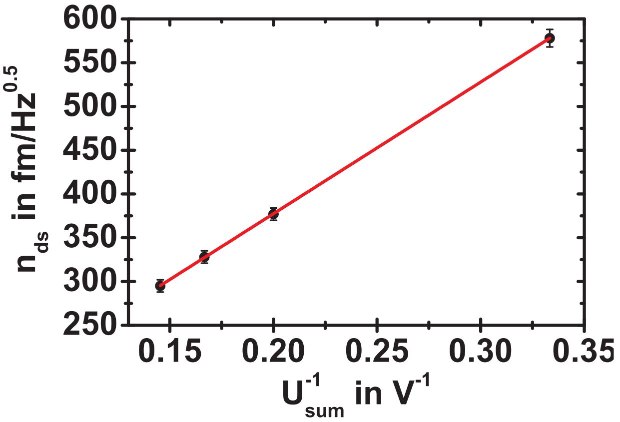

Figure 2.8: *Spectral noise density of the detection system with new preamplifier in dependence on the sum signal. The red, solid line represents a linear least squares fit to the data. The result is given in Eq. 2.14. Obviously, higher sum signals result in lower detection system spectral noise density values.*

From the linear, least squares fit of the data the following correlation was obtained

$$n_{\mathrm{ds}} = (77{\pm}1)\,\frac{\mathrm{fm}}{\sqrt{\mathrm{Hz}}} + \frac{(1504{\pm}4)\,\mathrm{V}\frac{\mathrm{fm}}{\sqrt{\mathrm{Hz}}}}{U_{\mathrm{sum}}} \, . \tag{2.14}$$

Using a sum signal of 6 V results in a spectral noise density of

$$n_{\mathrm{ds}} = (328{\pm}2)\,\frac{\mathrm{fm}}{\sqrt{\mathrm{Hz}}} \, . \tag{2.15}$$

---

[5] W. Schniederberend and D. Rathmann, electronics workshop, Universität Osnabrück, Osnabrück (2006)

[6] In cooperation with P. Rahe and S. Rode, Universität Osnabrück, Osnabrück (2008)

PLL The omicron electronics MATRIX does not contain a PLL at all. Instead, the frequency measurement is carried out by a simple demodulator. The main difference is that a demodulator only measures the AC part of the phase ϕ (the frequency) while the DC part ϕ_0 is a fixed value.

$$\phi = 2\pi\, f_0\, t + \phi_0 \tag{2.16}$$

The PLL determines the complete phase ϕ at any time.
We equipped the VT AFM 25 with an easy PLL Plus (Nanosurf, Liestal, Switzerland) for oscillation detection and signal demodulation. This instrument also contains a PI controller acting as amplitude feedback loop. Furthermore, it provides the excitation signal for the cantilever oscillation as well as the detuning signal for the distance feedback. Eventually, the MATRIX was only used to provide the high voltage signals for the piezos, for scan control, as distance feedback and for A/D conversion of the data signals.
A very important feature of the easy PLL Plus is an adjustable lowpass filter at the detuning signal output, which is directly recorded as detuning signal and used as input signal for the distance feedback loop. To avoid artifacts in the images a proper setting of this lowpass filter is mandatory. One has the choice between a cut-off frequency of 120 Hz, 400 Hz or 1300 Hz. The cut-off frequency (Nyquist frequency) of the sampling system is given by half of the sampling frequency. In other words, periodic structures must have a minimum wavelength of 2 pixel (pxl) to be resolved in the images. As I used a data aquisition time of $1\,\frac{\mathrm{ms}}{\mathrm{pxl}}$, the cut-off frequency of the scanner is always 500 Hz and a low pass filter setting of 1300 Hz does definitly not degrade the data information. Reducing the cut-off frequency of the lowpass filter to 400 Hz or even 120 Hz removes periodic features with a wavelength of up to 3 pxl or up to 8 pxl from the image, respectively. Hence, these settings are only appropriate for rather small pixel sizes.
The advantage of this lowpass filter is obviously noise reduction. As can be seen from Eq. 2.10, the detuning noise is proportional to $B^{\frac{3}{2}}$. As already mentioned, the sampling system itself acts as lowpass filter with $B = 500\,\mathrm{Hz}$. Thus, the noise level of the detuning signal can be reduced by a factor of 1.4 or 8.5 using the 400 Hz or the 120 Hz lowpass filter, respectively.

The thermal noise and the noise of the detection system calculated according to Eq. 2.9 and Eq. 2.10, respectively, using the parameters of the current setup as depicted in Tab. 2.1 are presented in Fig. 2.9. Furthermore, the resulting total detuning noise according to Eq. 2.8 is shown. The noise values are calculated in dependence on the quality factor Q for a bandwidth of 500 Hz (solid lines) and 120 Hz (dashed lines). As can be estimated from the graphs, for quality factors of at least 30,000 (500,000), the thermal noise is negligible when using a detection bandwidth of 500 Hz (120 Hz) together with the parameters depicted in Tab. 2.1.
Note that this calculation does not take into account noise originating from the demodulation process as well as from the A/D conversion.
Tab. 2.1 summarizes the experimental parameters in the setup proposed by Omicron and in the current setup as discussed in the text.

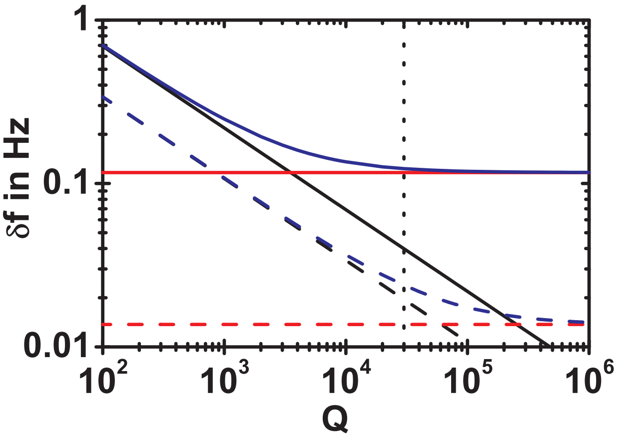

Figure 2.9: *Thermal noise (black), noise of the detection system (red) and resulting total detuning noise (blue), calculated according to Eq. 2.9, Eq. 2.10 and Eq. 2.8, respectively. The curves are presented for a bandwidth of $B = 500\,\mathrm{Hz}$ (solid lines) and $B = 120\,\mathrm{Hz}$ (dashed lines). The quality factor of 30,000 as typically used in the experiment is indicated by a dotted line. The other parameters of the current setup are chosen as depicted in Tab. 2.1.*

parameter	Omicron setup	current setup
f_0	300,000 Hz	
k	$40\,\frac{\mathrm{N}}{\mathrm{m}}$	
Q	10,000	30,000
A	3 nm	10 nm
U_{sum}	3 V	6 V
B	500 Hz	

Table 2.1: *Eigenfrequency f_0, stiffness k, quality factor Q and amplitude A as well as sum signal U_{sum} and detection bandwidth B in the setup proposed by Omicron and in the current setup.*

Current performance

A typical example illustrating the current performance of the microscope is presented in Fig. 2.10.

A part of an image obtained on rutile $TiO_2(110)$ using the 120 Hz lowpass filter is shown. Apparently, the corrugation is very small (about 0.20 Hz) in this particular experiment, nevertheless, the typical stripe-like structure of titania is clearly visible. The histogram of the df values is shown in Fig. 2.11. The Gaussian curve fit reveals a FWHM of about 0.35 Hz, being orders of magnitude smaller than that of the histogram in Fig. 2.6 (20 Hz). However, this FWHM is even too big to be a proper measure of the noise level as the corrugation is in the same order of magnitude as the FWHM: In fact, all detuning values obtained at equal surface sites are normally distributed with an FWHM, which would be the right measure for the detuning noise. All these individual Gaussian curves that are shifted according to the corrugation with respect to each other superimpose to form the histogram shown in Fig. 2.10. Hence, the real noise level can be estimated to be at maximum the difference between FWHM of the Gaussian curve in Fig. 2.10 and the

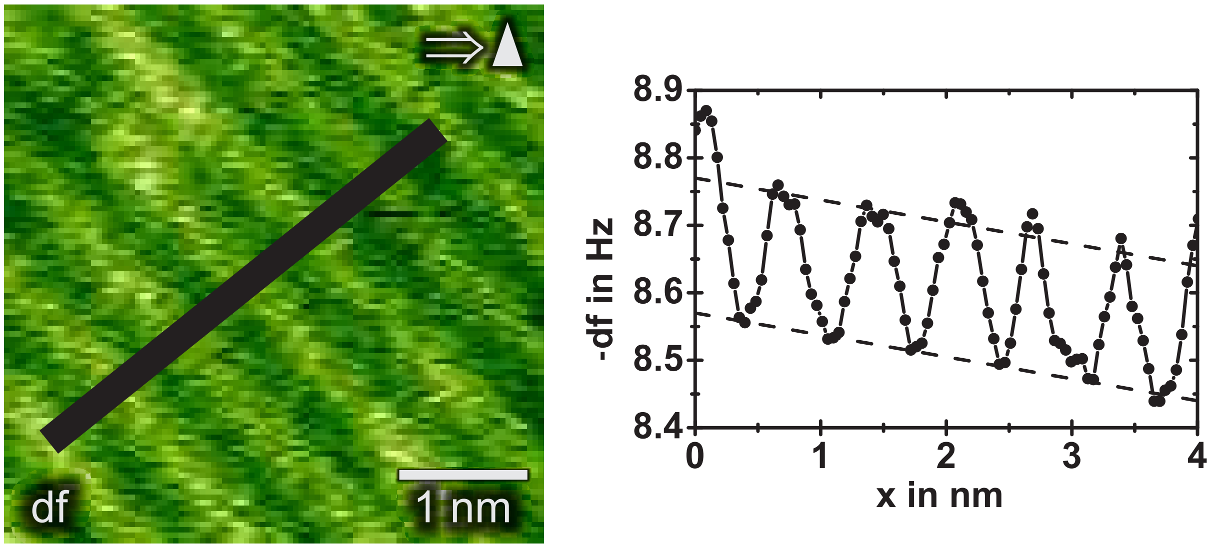

Figure 2.10: *Detuning image obtained on rutile* $TiO_2(110)$ *at a detuning setpoint of about -8.60 Hz using the 120 Hz lowpass filter. The typical parallel rows are resolved although the corrugation is only about 0.20 Hz as indicated by the line profile (5 pxl average) to the right (lines are guides to the eyes). The histogram of the df values is shown in Fig. 2.11.*

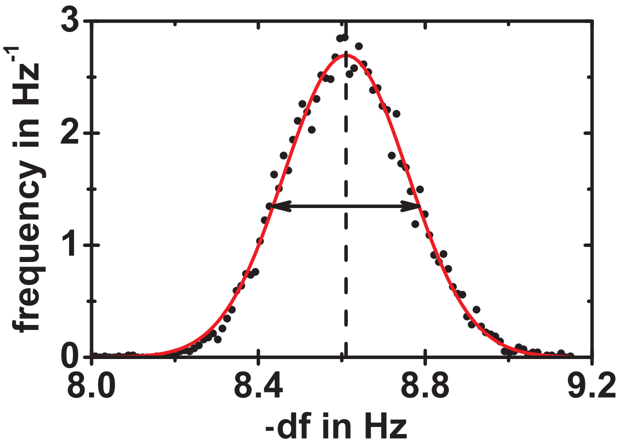

Figure 2.11: *Histogram of the df values of the detuning image presented in Fig. 2.10. The curve reveals a normal distribution of the detuning values. The fit by a Gaussian curve (red line) gives a FWHM of 0.35 Hz (indicated by arrow) which is orders of magnitude smaller than that in Fig. 2.6.*

associated corrugation. This gives an estimation of the noise level of about 0.15 Hz for detuning measurements using the 120 Hz lowpass filter. A similar estimation for images obtained with a bandwidth of 500 Hz reveals a noise level of about 0.5 Hz.

Summary A number of improvements were carried out to make utmost resolution possible with the VT AFM 25. The consequences of the improvements are as follows:

1. The measured detuning noise at a bandwidth of 500 Hz was massively decreased from
$$\delta f \approx \frac{FWHM}{2} = 10\,\mathrm{Hz}$$
to
$$\delta f \approx \frac{FWHM}{2} = 0.25\,\mathrm{Hz}\,.$$
2. The minimum detectable force gradient as can be calculated from Eq. 2.13 was decreased from
$$k_{\mathrm{ts}}^{\mathrm{min}} = 26.7{\cdot}10^{-4}\,\tfrac{\mathrm{N}}{\mathrm{m}}$$
to
$$k_{\mathrm{ts}}^{\mathrm{min}} = \ 0.7{\cdot}10^{-4}\,\tfrac{\mathrm{N}}{\mathrm{m}}\,.$$
3. The signal-to-noise ratio as introduced in Eq. 2.12 was increased by a factor of 6.6.
4. The restoring force of the cantilever was increased according to Eq. 2.1. Thus, the maximum detectable force was increased from
$$F_{ts}^{\mathrm{max}} \approx 0.01 \cdot F_{\mathrm{r}} = 1.6\,\mathrm{nN}$$
to
$$F_{ts}^{\mathrm{max}} \approx 0.01 \cdot F_{\mathrm{r}} = 4.0\,\mathrm{nN}\,.$$

As I aim for utmost resolution, these improvements are essential for my work.

2.3 Scan regime and data processing

All NC-AFM images presented in this thesis are raw data images. In the detuning images, higher negative detuning appears brighter while smaller negative or even positive detuning appears darker. The distance feedback loop was set in a way that the tip is approached towards the surface as long as $df - df_{setpoint}$ is a positive value.

All data were processed using the open source data processing software Gwyddion[7]. It is explicitly stated if an image was corrected for thermal drift.

The results presented in this thesis are obtained using a forward and backward, up and down lateral scanning regime as depicted in Fig. 2.12.

Forward and backward, the fast scan directions, are indicated by blue arrows. The slow scan directions, up or down, are indicated by yellow arrows. Note that, for simplicity, the identical coordinate system (hereafter referred to as forward-down-coordinate (FDC) system) is used for all images as the images are processed in this coordinate system by Gwyddion. Thus, the first pixel of an image does not necessarily coincide with the origin of the coordinate system as indicated by the red crosses in Fig. 2.12.

A single forward or backward image consists of 500 lines and 500 pxl per line. All images were obtained using a scan speed of 1 $\frac{\mathrm{ms}}{\mathrm{pxl}}$, which corresponds to an imaging time of 500 s per up or down image in total (forward and backward). Note that the Omicron scan electronics

---

[7] http://gwyddion.net

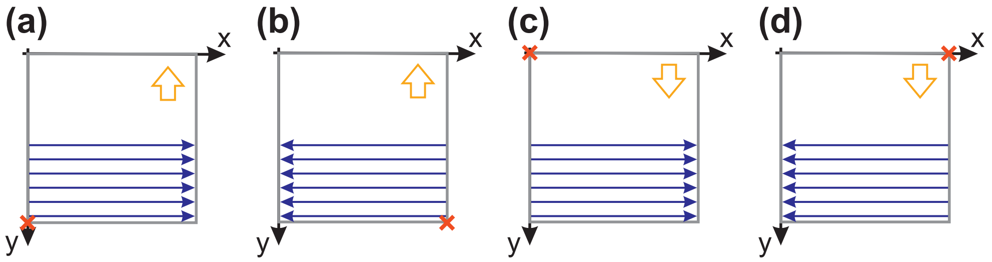

Figure 2.12: *Illustration of the lateral scanning regime. The fast scanning direction forward or backward is indicated by blue arrows. Up and down, the slow scan directions are marked by yellow arrows. Thus, four types of images are typically recorded: forward up (a), backward up (b), forward down (c) and backward down (d). The red crosses indicate the first pixel in each image. All image types are processed in a forward-down-coordinate (FDC) system by Gwyddion.*

MATRIX does expand the imaging time of an image per default by 60 s. Thus, the total aquisition time T of an up or down scanned image is

$$T = 560\,\mathrm{s}\,. \tag{2.17}$$

The origin of the delay is unclear to us.

Rescaling

The VT AFM 25 has been delivered with calibrated scan piezos. However, during the experiments it became obvious that lateral dimensions have to be corrected by a factor of

$$C_{\mathrm{lateral}} = 0.88 \pm 0.04 \tag{2.18}$$

for both, x and y direction. This factor has been reported before by Rahe [35] and was confirmed in experiments on Si(111)(7 × 7), $\mathrm{TiO_2}(110)$ and $\mathrm{CaCO_3}(10\bar{1}4)$[8]. Thus, all lateral dimensions reported in this thesis are rescaled by C_{lateral}.

Measurement and correction of vertical drift

Topography images are usually corrected for an arbitrary offset. In addition, a series of consecutively obtained topography images can be corrected for linear vertical drift.

In the most simple case, an untilted sample is imaged. To measure the drift velocity, height profiles along the slow scan direction (y direction) taken from consecutive up and down images are plotted as depicted by the blue lines in Fig. 2.13. In case of a positive (negative) drift velocity, these curves exhibit a monotonic increase (decrease) in z.

A constant difference in height $\Delta z = \dot{z} \cdot T$ between consecutive images can be measured if the drift velocity is constant. For simplicity, here, the average values of the images were plotted versus the aquisition time T. This, furthermore, allows to use images of different size and reduces the influence of the image corrugation and of statistical outliers. The vertical drift velocity $\dot{z}$ can be derived from a linear least squares fit of the average values. The slope of the resulting curve equals to $\dot{z}$. An example is shown in Fig. 2.14, where the

---

[8] J. Schütte, Universität Osnabrück, Osnabrück (2008)

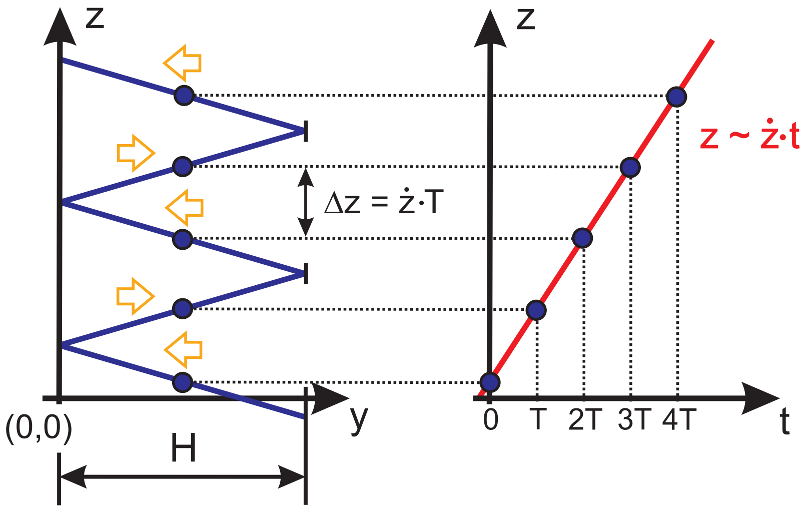

Figure 2.13: *Vertical drift correction scheme in case of an untilted sample. Line plots along the slow scan direction (image size H) taken from consecutive up and down images are depicted to the left. The average values are indicated by blue circles. The height difference between these values correspond to $\dot{z} \cdot T$. A plot of the average values versus aquisition time reveals a curve with constant slope $\dot{z}$.*

average values of 19 consecutively obtained topography images are plotted. The image size is indicated in the graph.

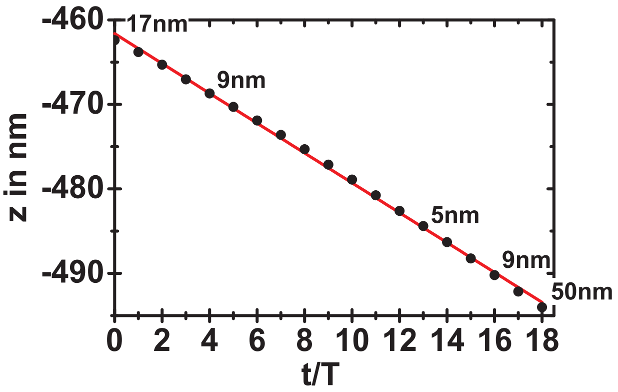

Figure 2.14: *Average values of 19 consecutively obtained topography images. The image size was changed as indicated by the values in the graph. The linear, least squares fit to the data reveals a slope of $\dot{z} = -(3.15 \pm 0.03)\,\frac{pm}{s}$. The total aquisition time of this image series was 3 h.*

Usually, the surface normal vector is not parallel to the scanner tube. The crystal often has a miscut in the order of 0.1°. Furthermore, misalignment of the cantilever during the glueing process is virtually unavoidable. Most importantly, the sample surface might not be planar per default. Surfaces can consist of vicinal facets or of terraces of different crystallographic face.

These variations result in a tilted sample surface, which has to be compensated by the distance feedback loop. A surface tilt by an angle β results in an additional height difference of $\pm H \cdot \tan\beta$ along the slow scan direction of an up or down image of lateral size H, respectively. This situation is depicted in Fig. 2.15. Thus, the total height differences in

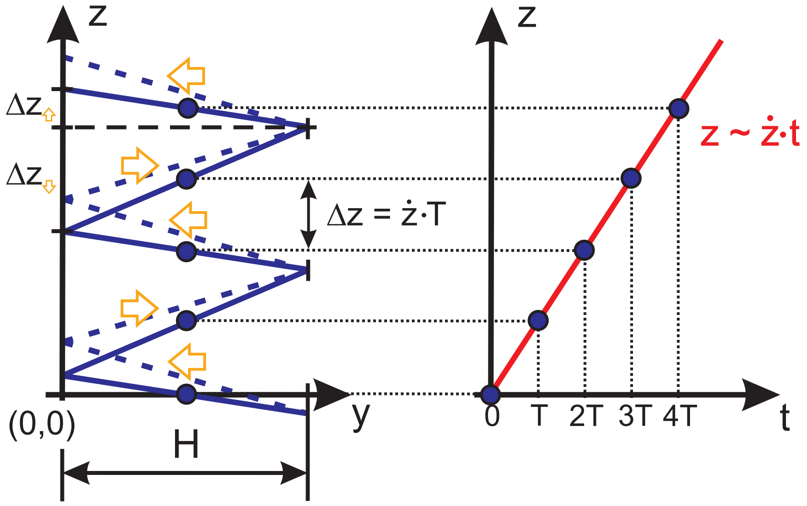

Figure 2.15: *Vertical drift correction scheme in case of a tilted sample. In analogy to Fig. 2.13, line plots along the slow scan direction are depicted to the left. The average values are indicated by blue circles. The height difference between average values from consecutive up and down images still corresponds to* $\dot{z} \cdot T$*. Thus, the plot of the average values versus aquisition time reveals a constant slope of* $\dot{z}$*, independent of the sample tilt.*

up and down images along y are

$$\Delta z_{\uparrow} = \dot{z} \cdot T + H \cdot \tan\beta \tag{2.19}$$

$$\Delta z_{\downarrow} = \dot{z} \cdot T - H \cdot \tan\beta \,. \tag{2.20}$$

However, the height difference between the average values of consecutive up and down images is

$$\Delta z = \frac{1}{2}\left(\Delta z_{\uparrow} + \Delta z_{\downarrow}\right) = \dot{z} \cdot T \,. \tag{2.21}$$

Hence, the already described recipe for obtaining the vertical drift velocity is also valid for tilted samples. Furthermore, sample tilt will not be corrected if the drift velocity is derived from the change in average value of consecutive up and down topography images.
A single topography image consists of N lines with M pixel per line. Thus it can be written as $(N \times M)$ matrix Z of height values z_{ij}

$$Z = (z_{ij})_{i=1\ldots N,\, j=1\ldots M} \,. \tag{2.22}$$

The vertical drift correction (vdc) of a forward down image is accomplished by

$$z_{ij}^{\mathrm{vdc}} = z_{ij} - \dot{z} \cdot \frac{T}{2\,M\,N} \cdot (j + 2\,M \cdot i) \tag{2.23}$$

in a FDC system as introduced in Fig. 2.12. For backward direction images replace j by $-j$ and for up images additionally replace i by $-i$ in the preceeding formula.

Measurement and correction of lateral drift

Lateral drift can be corrected by tracking a stationary feature in consecutively obtained images. Thus, the recipe presented here[9] is not limited to images revealing periodic structures of known size and angle. Note that all images are processed in a FDC system as Gwyddion uses this coordinate system.
For simplicity, we consider only linear drift with the constant drift velocity components $\dot{x}$ and $\dot{y}$. We define the drift velocity values to be positive if consecutively obtained images appear to move in x and y direction as depicted in Fig. 2.16(a). Accordingly, stationary features appear to move to the upper left as indicated in Fig. 2.16(b) and (c). The position of a stationary feature has to be measured either in two consecutive up or in two consecutive down images. Then, the drift velocities $\dot{x}$ and $\dot{y}$ are obtained by

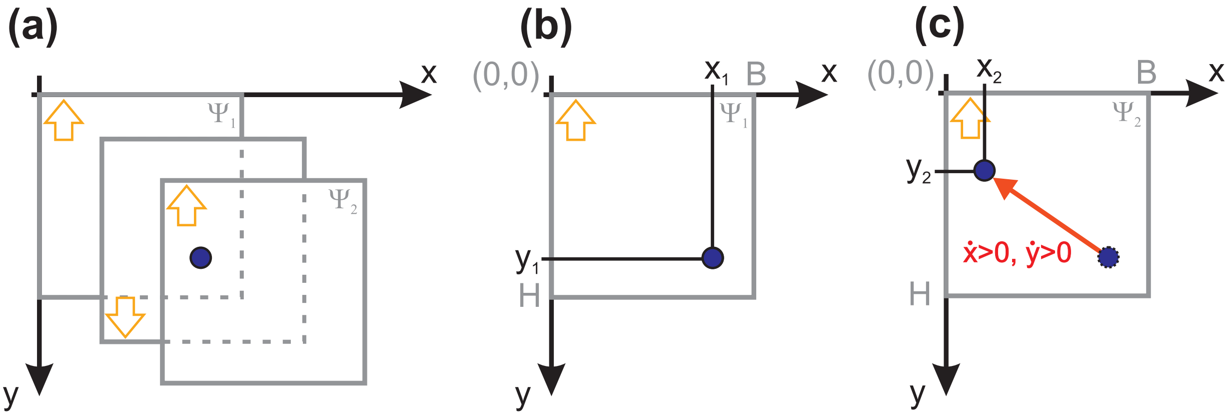

Figure 2.16: *Lateral drift velocity values can be obtained by tracking a stationary feature in consecutive up (or down) images. Here, a stationary feature (blue circle) can be identified in consecutive up images Ψ_1 and Ψ_2. The images appear to move to the lower right in this example (a). Accordingly, the feature appears to move to the upper left ((b) and (c)). We define the drift velocity values, resulting from this situation to be positive.*

$$\dot{x} = \frac{x_1 - x_2}{\triangle t} \tag{2.24}$$

$$\dot{y} = \frac{y_1 - y_2}{\triangle t}\,. \tag{2.25}$$

The difference in time $\triangle t$ has to be calculated according to

$$\triangle t_{\uparrow} = 2\,T + (y_1 - y_2)\,\frac{T}{H} \tag{2.26}$$

$$\triangle t_{\downarrow} = 2\,T - (y_1 - y_2)\,\frac{T}{H}\,, \tag{2.27}$$

depending on whether the positions of the stationary feature were obtained from consecutive up or down images. Note that the drift velocities obtained from up as well as from

---

[9] The recipe presented here emerged from a cooperation with P. Rahe (Universität Osnabrück, Osnabrück (2008)) and is based on ideas presented in [35].

down images are identical. Hence, for a reliable lateral drift correction, at least two up and two down images are necessary.

For the drift correction procedure, we first define two systems: The system Ψ as already introduced in Fig. 2.16 represents the image as acquired in the experiment. The system Σ represents the image corrected for lateral drift. Positions in Ψ and in Σ are measured in the same FDC system as introduced in Fig. 2.12 and are indicated by indices $\binom{x_\Psi}{y_\Psi} \in \Psi$ and $\binom{x_\Sigma}{y_\Sigma} \in \Sigma$, respectively. Therefore, the acquired image is rectangular with the width B and the height H. The corrected image is a parallelogram. The distortion induced by linear drift correction can be described by two parameters as introduced in Fig. 2.17: The angle α, which shears the image due to drift in x direction and the difference $H - H'$, representing a height compression due to drift in y direction. The width of the corrected image is still B and the scan lines are still parallel to the x direction. Compression in x direction and shearing of each single scan line is neglectible, as the aquisition time for a single scan line is smaller by a factor of 1000 compared to the aquisition time of a whole image.

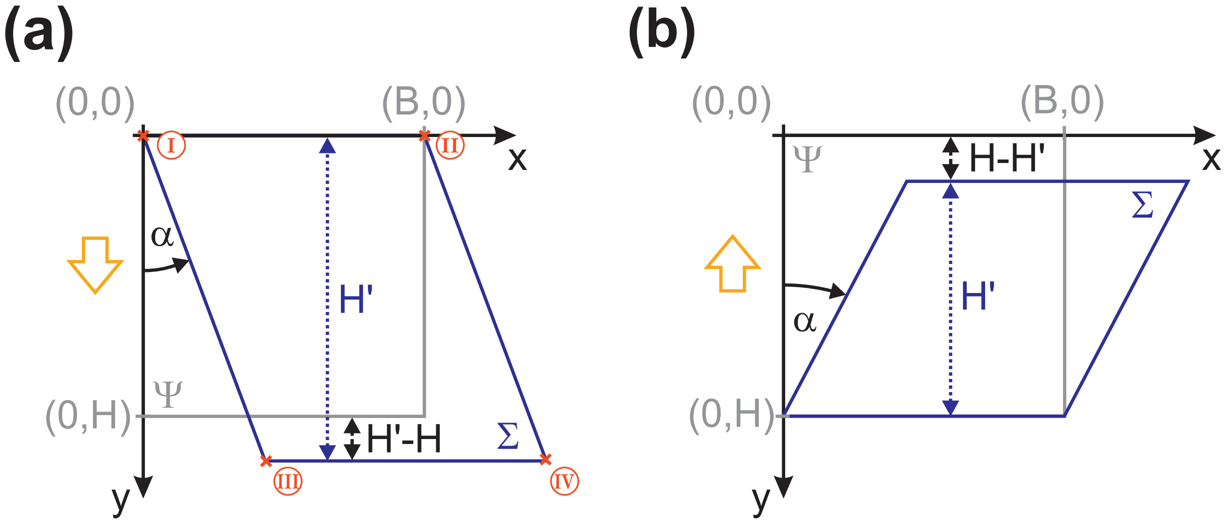

Figure 2.17: *Scheme indicating the distortion of a down (a) and an up (b) image by correction for lateral drift. The acquired image (Ψ) is indicated by a rectangular grey box of width B and height H. The image corrected for lateral drift (Σ) is indicated by a blue parallelogram. The effects of positive drift velocities $\dot{x}$ and $\dot{y}$ are shown. The images are sheared by an angle α due to drift in x direction. Drift in y direction is represented by the height difference $H - H'$. The width of the corrected image is still B and the scan lines are still parallel to the x direction after drift correction, as compression in x direction and shearing of each scan line is neglected.*

The parameters α and $H - H'$ are related to the drift velocities by simple geometry according to

$$\dot{x}T = H' \tan\alpha \tag{2.28}$$

$$\dot{y}T = H - H' \tag{2.29}$$

for an up image, and

$$\dot{x}T = H' \tan\alpha \tag{2.30}$$

$$\dot{y}T = H' - H \tag{2.31}$$

for a down image. The orientation of the angle is depicted in Fig. 2.17. Note that α is different in up and down images. The parameter T is the aquisition time as introduced in Eq. 2.17.
The drift correction will be carried out by a polynomial distortion according to the ansatz

$$x_\Psi = P_x(x_\Sigma, y_\Sigma) = a_0 + a_1 x_\Sigma + a_2 y_\Sigma \tag{2.32}$$

$$x_\Psi = P_y(x_\Sigma, y_\Sigma) = b_0 + b_1 x_\Sigma + b_2 y_\Sigma\,. \tag{2.33}$$

The coefficients a_i, b_i have to be calculated for up and down images separately.
To derive the coefficients a_i, b_i in Eq. 2.32 and 2.33 for a down image, we consider the corner points I to IV as marked in Fig. 2.17(a):

$$\begin{array}{ll}
\text{Point I:} & P_{x,\downarrow}(0,0) = a_0 = 0 \\
& P_{y,\downarrow}(0,0) = b_0 = 0 \\
\text{Point II:} & P_{x,\downarrow}(B,0) = a_1 B = B \\
& \quad \Rightarrow a_1 = 1 \\
& P_{y,\downarrow}(B,0) = b_1 B = 0 \\
& \quad \Rightarrow b_1 = 0 \\
\text{Point III:} & P_{x,\downarrow}(H'\tan\alpha, H') = H'\tan\alpha + a_2 H' = 0 \\
& \quad \Rightarrow a_2 = -\tan\alpha \\
& P_{y,\downarrow}(H'\tan\alpha, H') = b_2 H' = H \\
& \quad \Rightarrow b_2 = \frac{H}{H'}
\end{array}$$

Point IV serves as a crosscheck:

$$P_{x,\downarrow}(B + H'\tan\alpha, H') = B + H'\tan\alpha - H'\tan\alpha = B \quad \checkmark$$

$$P_{y,\downarrow}(B + H'\tan\alpha, H') = \tfrac{H}{H'} H' = H \quad \checkmark$$

Using Eq. 2.30 and 2.31 the final result for the polynoms are:

$$x_\Psi = P_{x,\downarrow}(x_\Sigma, y_\Sigma) = x_\Sigma - \tfrac{\dot{x}T}{H+\dot{y}T}\, y_\Sigma \tag{2.34}$$

$$y_\Psi = P_{y,\downarrow}(x_\Sigma, y_\Sigma) = \tfrac{H}{H+\dot{y}T}\, y_\Sigma\,. \tag{2.35}$$

The coefficients for the correction of up images can be calculated in complete analogy.
The resulting polynomial equations are

$$x_\Psi = P_{x,\uparrow}(x_\Sigma, y_\Sigma) = \tfrac{-\dot{x}TH}{H-\dot{y}T} + x_\Sigma + \tfrac{\dot{x}T}{H-\dot{y}T}\, y_\Sigma \tag{2.36}$$

$$y_\Psi = P_{y,\uparrow}(x_\Sigma, y_\Sigma) = \tfrac{H}{H-\dot{y}T}\,(y_\Sigma - \dot{y}T)\ . \tag{2.37}$$

In Gwyddion, a polynomial distortion tool is implemented. The coordinates in this tool are defined on the interval $[0,1]$. Thus, to use the polynoms presented in Eq. 2.34 to 2.37, they have to be modified by the substitutions $H \rightarrow 1$ and $B \rightarrow 1$. Furthermore, $\dot{x}$ and $\dot{y}$ has to be normed to $[0,1]$. This is accomplished by the substitutions $\dot{x} \rightarrow \frac{\dot{x}}{B}$ and $\dot{y} \rightarrow \frac{\dot{y}}{H}$. Lateral drift correction with the polynomial distortion tool of Gwyddion is then carried out according to:

$$P_{x,\downarrow}(x,y) = x + \frac{-T\frac{\dot{x}}{B}}{1+T\frac{\dot{y}}{H}}\,y \tag{2.38}$$

$$P_{y,\downarrow}(x,y) = \frac{1}{1+T\frac{\dot{y}}{H}}\,y \tag{2.39}$$

$$P_{x,\uparrow}(x,y) = \frac{-T\frac{\dot{x}}{B}}{1-T\frac{\dot{y}}{H}} + x + \frac{T\frac{\dot{x}}{B}}{1-T\frac{\dot{y}}{H}}\,y \tag{2.40}$$

$$P_{y,\uparrow}(x,y) = \frac{-T\frac{\dot{y}}{H}}{1-T\frac{\dot{y}}{H}} + \frac{1}{1-T\frac{\dot{y}}{H}}\,y \tag{2.41}$$

3 Rutile titanium dioxide

Rutile is the most common natural form of titanium dioxide (TiO_2). Other important polymorphs are anatase and brookite. The most stable face of rutile titania is the (110) surface [1]. In the following, a brief introduction to the surface structure of $TiO_2(110)$ is given. The focus of this chapter is on the appearance of the surface in atomically resolved NC-AFM images. It will be discussed how the observed contrasts can be understood in terms of tip-sample interaction.

3.1 Introduction to rutile $TiO_2(110)$

Titanium dioxide, crystallized in the rutile form, has a tetragonal structure with

$$\begin{aligned} a = b &= 458\,\mathrm{pm} \\ c &= 296\,\mathrm{pm}. \end{aligned}$$

The bulk unit cell is depicted in Fig. 3.1(a). The main building block is an octahedron with a titanium atom in the center, coordinated with six oxygen atoms at the edges. Oxygen is threefold coordinated in the bulk. The Ti-O bond lengths are 195 pm and 198 pm, respectively [1]. The Ti-O bond has iono-covalent character. The electron transfer has been estimated to be in the order of 0.35 per bond. This results in a formal charge of about -1 for oxygen and approximately $+2$ for titanium [36].

Surface structure

The (110) surface consists of parallel rows of protuding, twofold coordinated oxygen atoms (referred to as bridging oxygen), in-plane, threefold coordinated oxygen atoms and in-plane, fivefold coordinated titanium atoms as shown in Fig. 3.1(c). The bridging oxygen rows are separated by 649 pm and the interatomic spacing along the row is 296 pm. The vertical distance between bridging oxygen and fivefold coordinated titanium has been measured to be approximately 110 pm. The monatomic step height is 325 pm [1].

Titania is known to become reduced upon sputtering and annealing in UHV. The sputter yield for oxygen is higher than for titanium. During the subsequent annealing procedure, titanium diffuses into the bulk to reoxidize the surface [13]. In turn, the bulk becomes reduced. There is an ongoing discussion about how reduction manifests in the bulk. Most probably titanium interstitials exist in the bulk [37]. These interstitials are observed to diffuse to the surface when the reduced sample is heated in oxygen atmosphere to be converted to new titania layers [13]. However, it has been proven by a number of carefully performed experiments that bulk reduction manifests as bridging oxygen vacancies at the rutile surface [9, 38, 39]. Therein, water from the residual gas has been observed to adsorb dissociatively at vacancy sites. The hydroxyl group fills the vacancy, the proton adsorbs

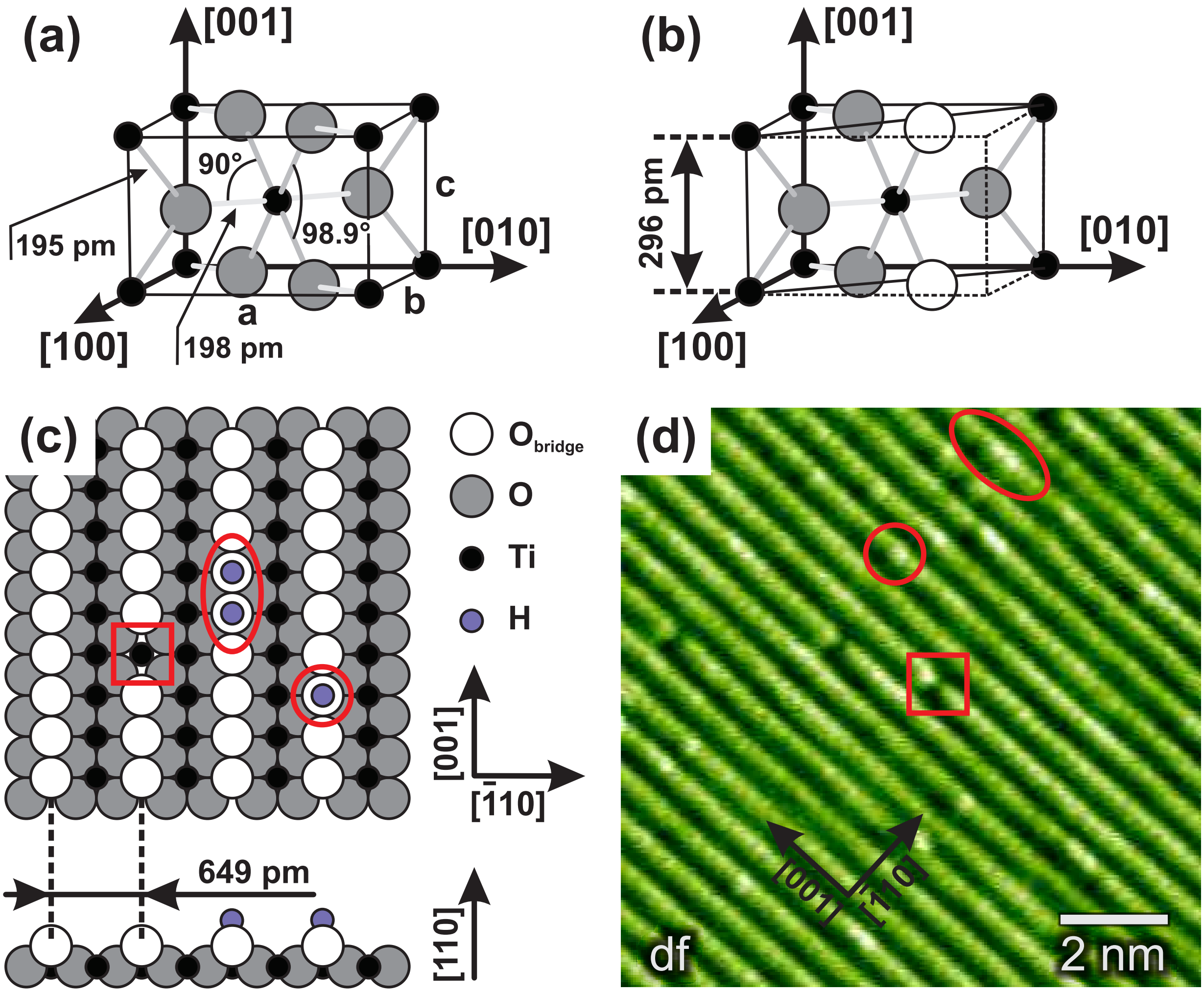

Figure 3.1: *The bulk unit cell of rutile titania is depicted in (a) (taken from [1]). The lattice structure of the (110) surface of rutile titanium dioxide is sketched in (b) and (c). The predominant defect species on the surface are bridging oxygen vacancy, double hydroxyl and single hydroxyl as indicated by a red square, ellipse and circle, respectively. In (d) a representative NC-AFM detuning image is shown, illustrating one possible appearance of the surface and of the three defect species. Alternating rows of bridging oxygen and titanium atoms aligned along the [001] direction lead to the typical stripe-like pattern in scanning probe microscopy images.*

on top of an adjacent bridging oxygen atom. The resulting formation of two hydrogens adsorbed on neighboring bridging oxygens is usually called double hydroxyl. Double hydroxyls split into single hydroxyls by diffusion. Thus, vacancies and double hydroxyls are only present at the freshly prepared surface for a few hours or even less, depending on the partial pressure of water in the UHV chamber. Eventually all vacancies will be saturated and only single hydroxyls will be observable at the surface.
In conclusion, three defect species are typically observed on the freshly prepared $TiO_2(110)$ surface

- bridging oxygen vacancy
- double hydroxyl

- single hydroxyl

as depicted in Fig. 3.1(c) by a red square, ellipse and circle, respectively. Note that all three defect species are exclusively situated in the bridging oxygen rows.

As already mentioned, consecutive preparation further reduces the titania sample. In [9], Wendt et al. report on a linear dependency of the defect density on the preparation history. The latter is defined as annealing duration times annealing temperature. To give an impression of the typical defect density in our experiments, we conducted a similar series of measurements [40]. The graph in Fig. 3.2 shows the percentage of monolayer single hydroxyls (1 ML corresponds to one hydroxyl per unit cell) against the product of annealing time and annealing temperature. Note that also images with three different types of defects have been included in this graph. The numbers of both, oxygen vacancies and double hydroxyls have been multiplied by a factor of two before adding to the number of single hydroxyls, as one oxygen vacancy transforms into two single hydroxyl defects as described above. The grey area in Fig. 3.2 corresponds to the typically observed hydroxyl density of

$$[\mathrm{OH}] = (0.45 \pm 0.30)\,\frac{\%\,\mathrm{ML}}{10^3\,\mathrm{h}\cdot\mathrm{K}}. \tag{3.1}$$

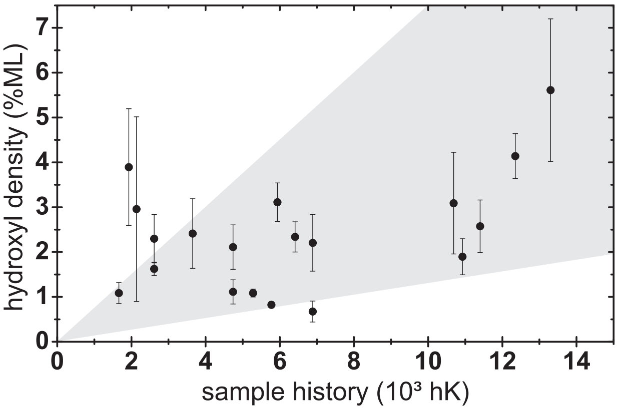

Figure 3.2: *Hydroxyl density as a function of sample history, taken from [40]. The percentage of monolayer single hydroxyls is shown (1 ML corresponds to one hydroxyl per unit cell) against the product of annealing time and annealing temperature. The data shown here were obtained from NC-AFM images collected from five different samples. An overall trend of increasing hydroxyl density upon increasing sample history can be seen, illustrated by the grey area and corresponding to typically observed hydroxyl densities.*

Preparation procedure

Oxide surfaces are usually cleaned by repeated cycles of sputtering and subsequent annealing under UHV conditions to achieve extended, atomically flat terraces. The $TiO_2(110)$ samples used for this PhD study were crystals of highest quality available from MTI (Richmond, USA). Fresh samples were prepared in UHV by at least five cycles of sputtering and subsequent annealing prior to the first NC-AFM experiment and by one or two additional cycles prior to following experiments, respectively. The samples were sputtered with an ISE 10 ion source (Omicron NanoTechnology GmbH, Taunusstein, Germany) using Ar^+ ions

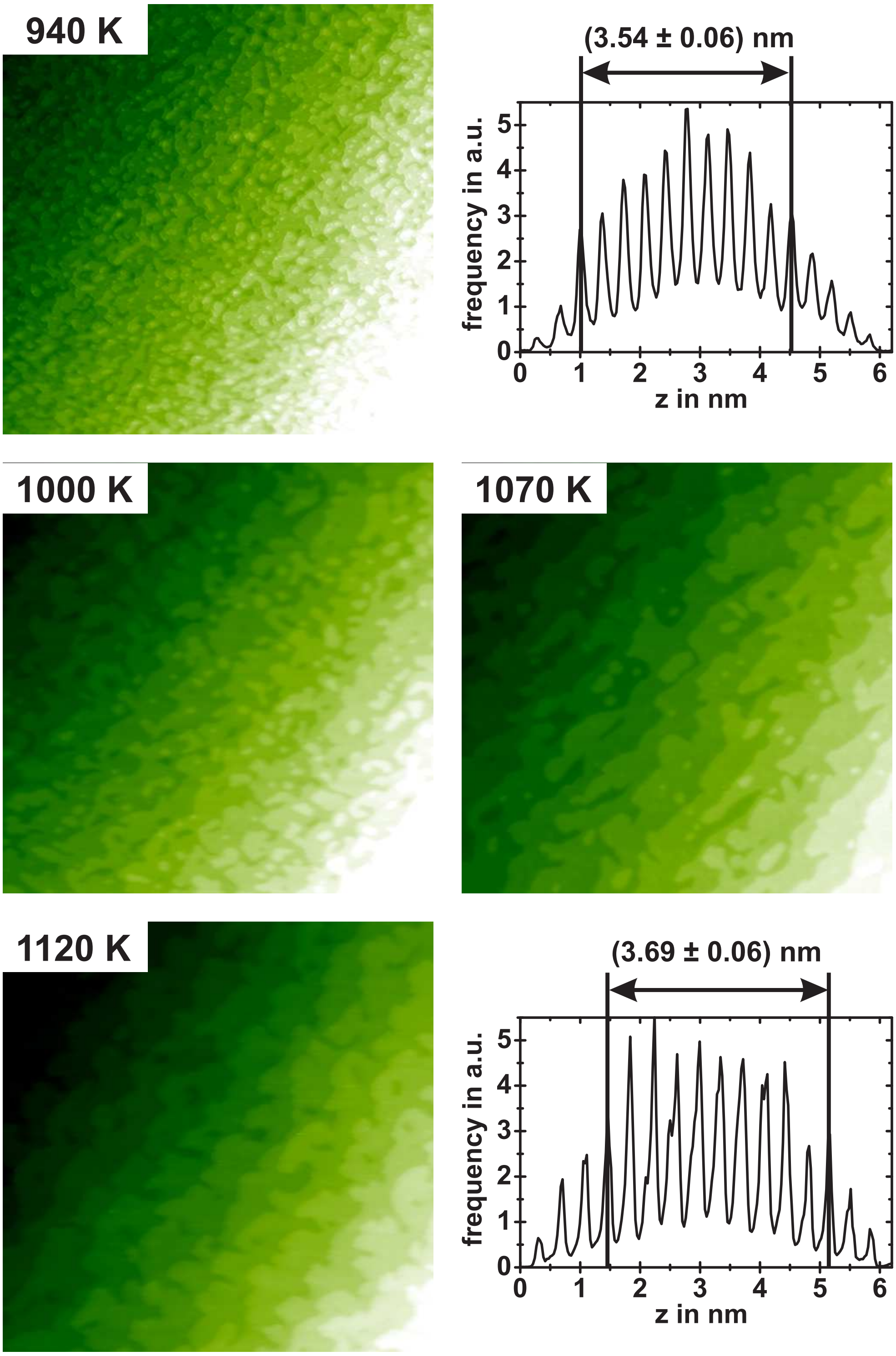

Figure 3.3: *NC-AFM topography images of equal size ($440 \cdot 440\,\mathrm{nm}^2$) obtained on the very same sample after preparation cycles with different annealing temperatures. All images are presented with identical color scale. After annealing at 940 K the terraces are rather perforated and a lot of small islands can be identified on the terraces. Annealing at 1120 K results in extended terraces free from islands. For two of the images histograms are shown, revealing 16 and 17 monatomic steps of equal height in the images, respectively. The apparent monatomic step height as indicated by the arrows is (360 ± 10) pm on average.*

at an argon partial pressure of $3 \cdot 10^{-6}$ mbar and a kinetic energy of 1 keV. The angle of incidence was 50°; the sputter time was 15 min. Subsequently, the samples were annealed by resistive heating of a stripe of doped silicon, directly attached to the backside of the sample. The temperature was held at 1100 K for 15 min. The annealing temperature was estimated using a Sensortherm MS09 pyrometer (Sensortherm GmbH, Frankfurt am Main, Germany) operated in ambient. It detects infrared light from the hot sample through a glas view port. This measurement is well reproducible at our system but rather delicate to compare to measurements of other groups. The transparency of the view port and the exact position of the pyrometer have a significant influence on the measured values. Thus, the absolute values of annealing temperatures reported here and from the literature should not be taken too literally. Usually, temperatures in the range of 900 K [10] to 1100 K [41] are reported for the preparation of titania. Temperatures higher than 1100 K are reported to result in reconstruction of the surface [41–43].

To eventually identify the best annealing temperature, we[1] successively increased the temperature in consecutive preparation cycles and checked the resulting surface morphology by NC-AFM. In Fig. 3.3 NC-AFM topography images of equal size are shown, obtained at the very same sample after preparation cycles with different annealing temperatures. At the atomic scale, all surfaces exhibited an unreconstructed, (1 × 1) unit cell (not shown). The number of terraces in a single image is determined by the miscut of the sample and therefore identical in all images. For evidence, all images are presented with identical color scale. Furthermore, for two of the images histograms are shown in Fig. 3.3 exhibiting about 16 to 17 terraces in each image. However, the number of small islands on the terraces decreases rapidly with increasing temperature. While annealing at 940 K results in rather perforated terraces covered by numerous small islands, extended, atomically flat terraces are achieved by using an annealing temperature of about 1100 K.

Height of monatomic steps

The two histograms in Fig. 3.3 furthermore indicate an average monatomic step height of (360 ± 10) pm. This uncalibrated value is slightly larger than the monatomic step height of titania as can be expected from the unit cell (325 pm). The ratio between expected and measured step height is 0.90 ± 0.02, which is identical within the error with the rescaling factor for lateral dimensions C_{lateral} as introduced in Eq. 2.18.

3.2 Rutile TiO_2(110) imaged by NC-AFM

Alternating rows of bridging oxygen and titanium atoms aligned along the [001] direction lead to the typical stripe-like pattern in scanning probe microscopy images as already depicted in Fig. 3.1(d). The typical defect species, namely oxygen vacancies as well as single and double hydroxyls are exclusively situated in the bridging oxygen rows. This fact can be used to identify the bridging oxygen row in NC-AFM images. Contrast modes on titania obtained with NC-AFM are usually classified by the appearance of defects with respect to the bridging oxygen rows. In the following, four contrast modes are presented that were obtained on rutil TiO_2(110) with NC-AFM at room temperature. As these

---

[1] in cooperation with J. Schütte and P. Rahe, Universität Osnabrück, Osnabrück (2007)

contrast modes depend on the tip termination, they emerge unintended and occasional contrast changes between all of them were observed.

3.2.1 Hole mode and protrusion mode

Two contrast modes are well-established on titania so far, namely hole mode and protrusion mode as introduced by Lauritsen et al. in 2006 [10]. The hole mode has already been observed in 1997 by Fukui et al. [8].
In protrusion mode, titanium atoms appear bright while bridging oxygen rows are dark. The defect species are imaged as bright features protruding the dark oxygen rows. An example is given in Fig. 3.4, where all three defect species can be distinguished. A vacancy is revealed as faint, bright feature (marked by a red square) while the hydroxyl species (indicated by a red circle and an ellipse) even protrude the titanium rows. Single and double hydroxyls can be distinguished by their apparent length in [001] direction.

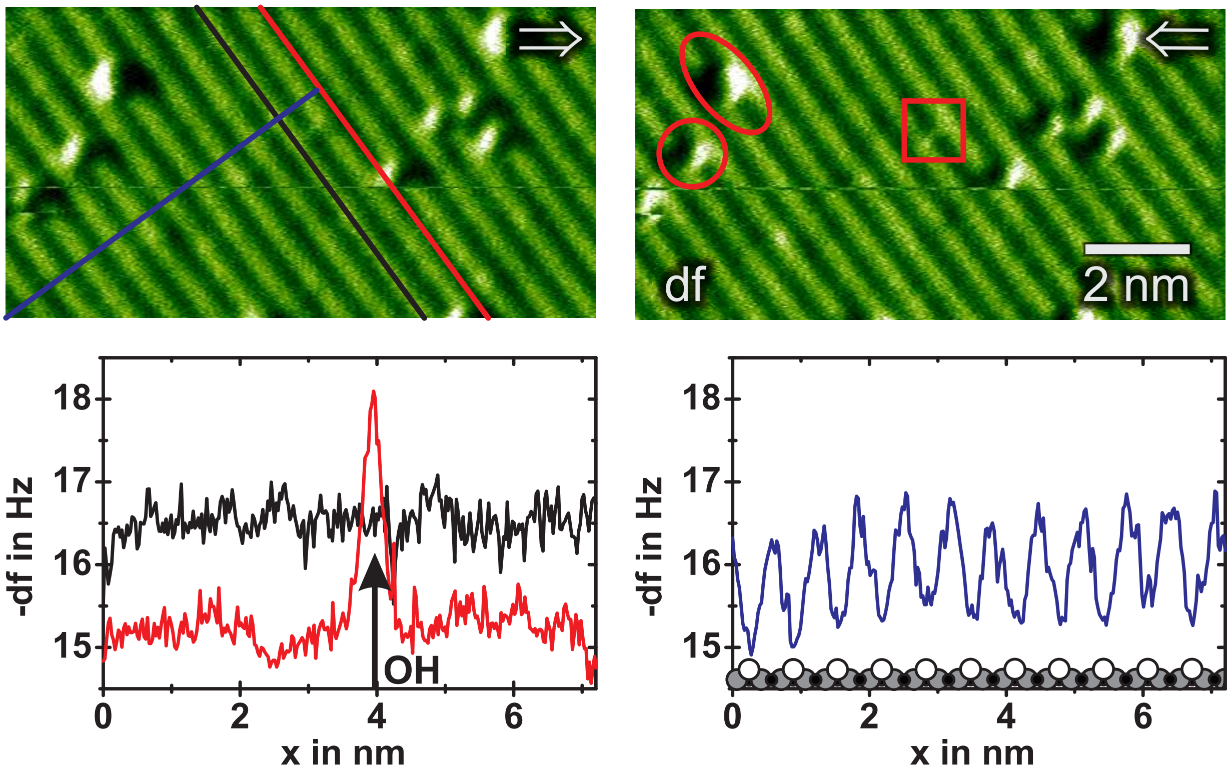

Figure 3.4: *Forward and backward NC-AFM detuning images obtained on $TiO_2(110)$. The defects appear as protrusions in dark bridging oxygen rows while titanium is imaged bright. Hence, these images represent the protrusion mode. Double hydroxyls (red ellipse) are more extended in [001] direction than single hydroxyls (red circle). Vacancies (red square) are only faint bright. The shadow at the right (left) side of protruding features in the image obtained in forward (backward) fast scan direction is a scan artifact. It is caused by slow distance feedback loop settings as described in [25]. The line profiles (3 pxl average) along titanium row (black) and oxygen row (red) as well as perpendicular to the [001] directon (blue) depict a detuning corrugation of about 1.5 Hz measured between oxygen and titanium. The detuning difference between titanium and hydroxyl (OH) sites is measured to be approximately 1.5 Hz in this case.*

In hole mode, the contrast appears inverted compared to the protrusion mode; i.e. titanium is dark and bridging oxygen rows are imaged bright as shown in Fig. 3.5. The defect species appear as holes in the bridging oxygen rows. Although Fig. 3.5 exhibits only one defect species, consequently assigned to single hydroxyl, it has been proven that all defect species appear as holes in this mode [10].
The line profiles along titanium row (black line), oxygen row (red line) as well as perpendicular to the [001] direction (blue line) that are shown in Fig. 3.4 and Fig. 3.5 depict typical detuning corrugations in the two contrast modes, respectively. The qualitative appearance of the surface sites as discussed above are reflected in the graphs, however, the absolute detuning values strongly depend on the exact structure of the tip.

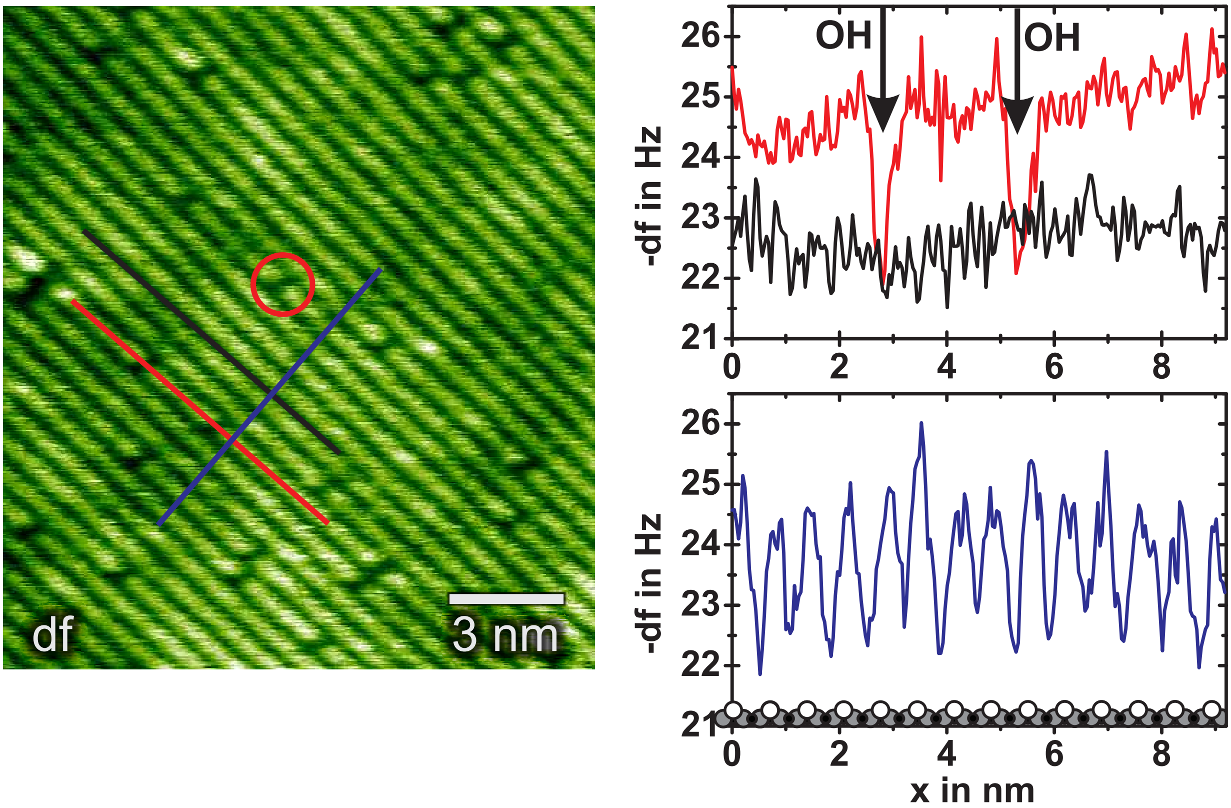

Figure 3.5: *NC-AFM detuning image of* TiO_2*(110) showing bright bridging oxygen rows and dark titanium. Defects appear as holes in bright rows, therefore this contrast is called hole mode. In this particular case, only hydroxyls (red circle) are supposed to exist. From the line profiles (3 pxl average) the detuning corrugation can be estimated to be about 2.5 Hz between titanium and oxygen as well as between hydroxyl (OH) species and oxygen.*

These two contrast modes might be explained by pure electrostatic interaction as reported by Lauritsen et al. [10]. Titanium sites and hydroxyls are supposed to be positively charged while oxygen has a negative charge. Hence, a positively charged tip would be attractive to oxygen, solely, while a negatively charged tip is only attractive to titanium and hydroxyl sites. A magnesium oxide (MgO) cube has been used as model tip in that work, which can be oriented to have either a positive (Mg^{2+}) or negative (O^{2-}) tip apex.
Note that neither protrusion mode nor hole mode represent the real topography of the surface, but rather reflect the local charge distribution.

3.2.2 Neutral mode and all-inclusive mode

Neutral mode

Recently, a third contrast mode has been reported, where bright defects protude bright oxygen rows while titanium appears dark [44]. Only one type of defects has been observed in that particular study, consequently assigned to hydroxyl species. This contrast mode has been introduced as neutral mode, as it is not possible to explain this contrast by pure electrostatic interaction. The image depicted in Fig. 3.6 shows dark titanium and bright oxygen with protrusions on the oxygen rows. Thus, this image represents an example for

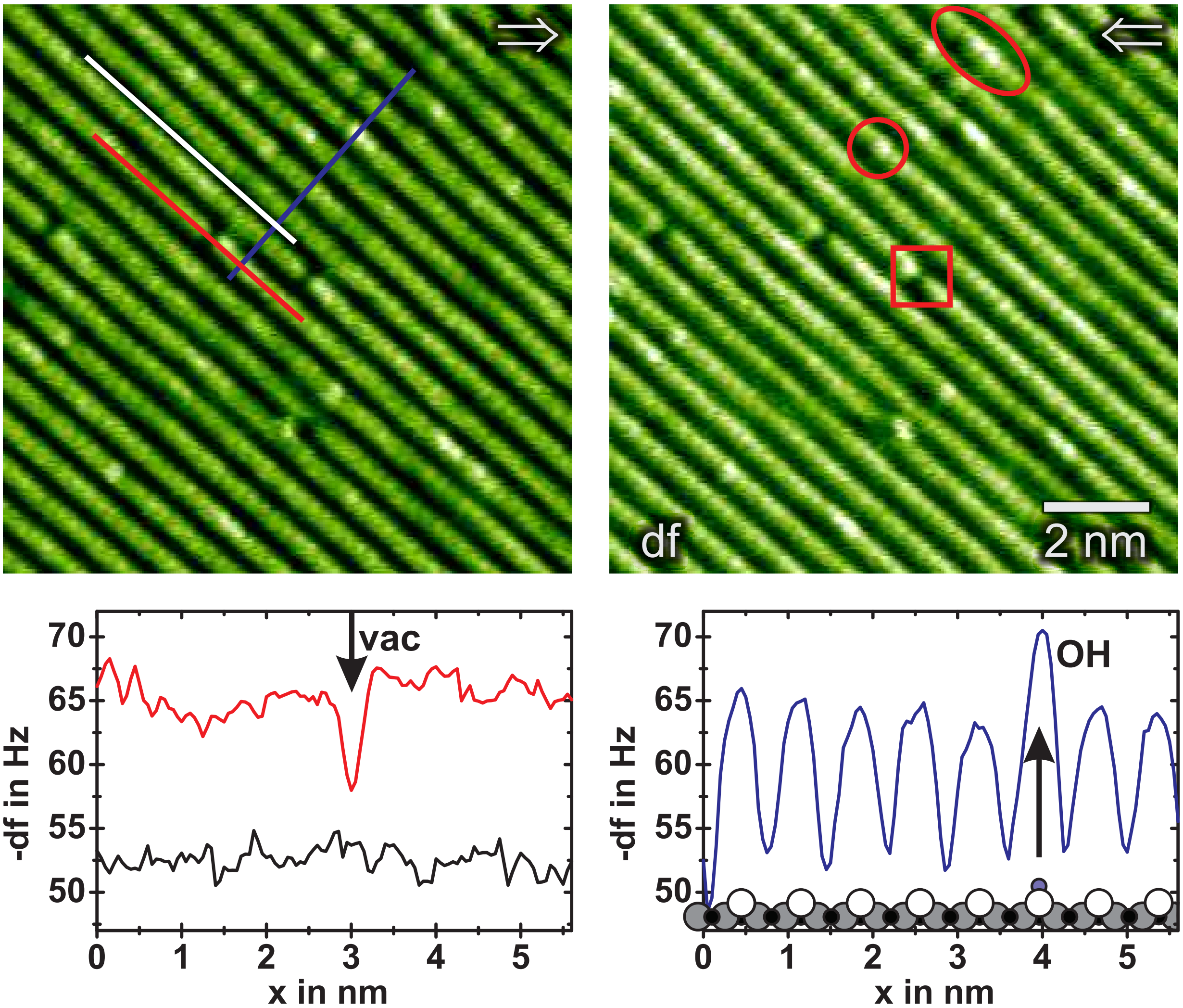

Figure 3.6: *Forward and backward NC-AFM detuning image obtained on $TiO_2(110)$ in neutral mode. The color scale is identical for both images. Titanium rows are dark. Hydroxyls appear as protrusions in bright bridging oxygen rows. Double hydroxyls (red ellipse) are more extended in [001] direction than single hydroxyls (red circle). Vacancies (red square) appear as holes. Both graphs, presenting line profiles along titanium (white) and bridging oxygen (red) row as well as perpendicular (blue) reveal a detuning corrugation of approximately 12 Hz measured between titanium and oxygen. The detuning at hydroxyl (OH) and vacancy (vac) sites differ by about -5 Hz and 7 Hz from that of oxygen, respectively.*

the neutral mode. However, this image also contains holes in the bridging oxygen rows. In the presented line profile along the bridging oxygen row (red line) the vacancy (vac) appears as dip. A hydroxyl (OH) is imaged as peak at a bridging oxygen site in the line profile perpendicular to the [001] direction (blue line). In conclusion, three defect species can be distinguished in Fig. 3.6. Protuding hydoxyl species that are distinguishable by their elongation in [001] direction and oxygen vacancies that appear as holes. Hence, this contrast resembles the real topography of the surface.
However, it does not show the titanium rows.

All-inclusive mode

Here, I introduce a fourth contrast mode, which reflects the real topography and images all surface species simultaneously. Hence, this mode is referred to as *all-inclusive mode*.

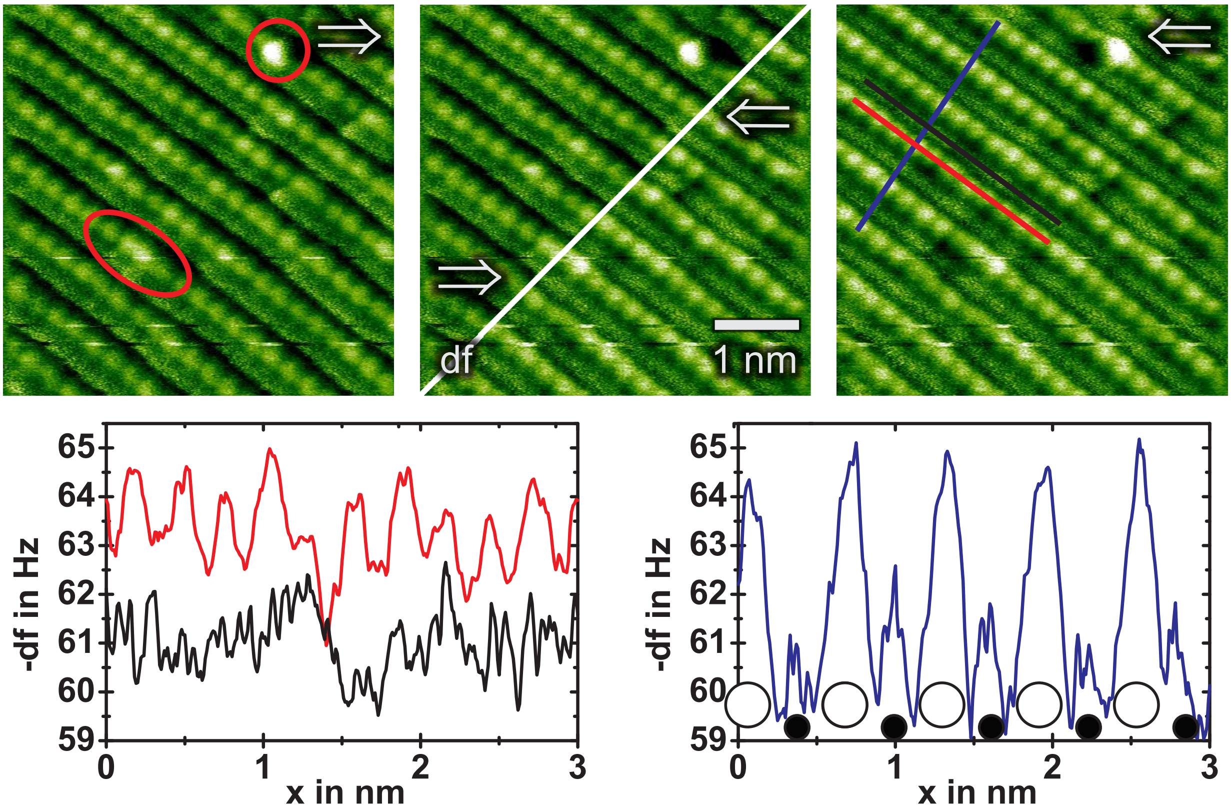

Figure 3.7: *Forward and backward NC-AFM detuning image obtained on TiO_2(110). Bridging oxygen atoms appear bright while titanium rows are imaged faint bright. The thin dark lines in between are assigned to in-plane oxygen atoms. The observed contrast is independent of the scan direction as indicated by the image in the middle which is an assembly of the images shown at the left and the right. The color scales of the images are identical. The slight difference in overall detuning is approximately 0.5 Hz and can be explained by an inert distance feedback loop (Fig. 3.9 and explanation in the text). Single and double hydroxyl appear as protrusions as indicated by red circle and ellipse, respectively. The other defects are shown in Fig. 3.8. The line profiles (3 pxl average) reveal a detuning corrugation of 1.5 Hz along the oxygen row (red line). The detuning difference between in-plane oxygen and titanium and between titanium and bridging oxygen is about 2 Hz and 3.5 Hz, respectively (blue line).*

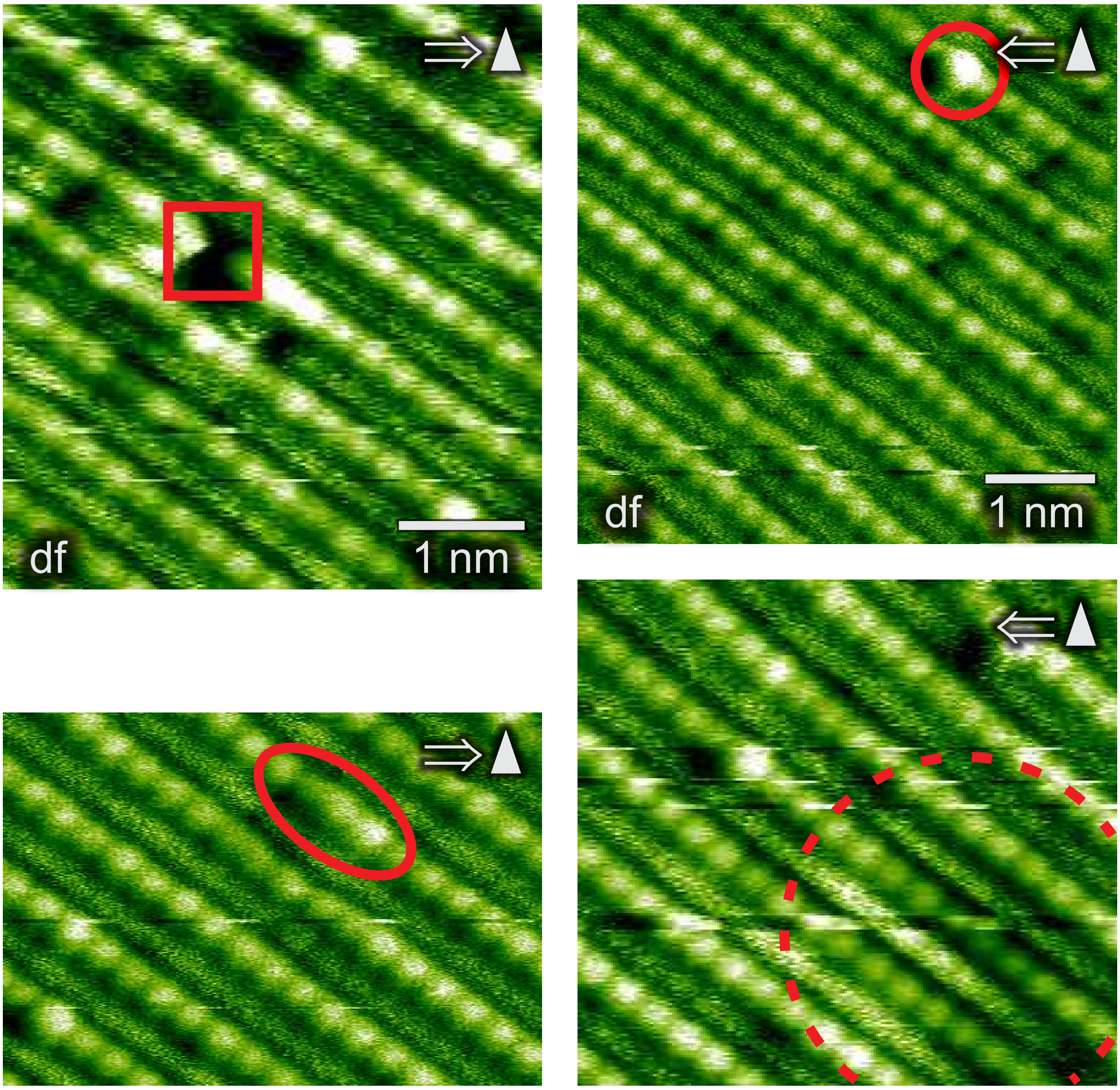

Figure 3.8: *NC-AFM detuning images obtained on TiO_2(110) in all-inclusive mode presented with identical color scale. Four representative images corrected for linear lateral drift are shown, imaging the four observed defect species in detail. Single hydroxyls (red circle) are imaged as atomic size protrusions. The double hydroxyl (red ellipse) appears as protrusion as well, but is extended over two neighboring oxygen atoms. The vacancy (red square) appears as hole in the bridging oxygen row. The fourth defect species (red dashed circle) has been introduced as subsurface impurity by Batzill et al. [45]. This defect appears usually as extended, nearly circular region. Here, the defect manifests as region where the bridging oxygen rows appear lowered. A detailed discussion of this species follows in Fig. 3.10.*

As can be seen from Fig. 3.7, bridging oxygen atoms appear bright and titanium rows are imaged as faint, bright lines in all-inclusive mode. These bright lines are clearly separated by dark lines, representing the in-plane oxygen atoms (see Fig. 3.1(c)). The defects appear qualitatively similar to the neutral mode. As indicated in Fig. 3.8, hydroxyl species protrude bridging oxygen while vacancies appear as holes. The obvious difference between neutral mode and all-inclusive mode is the additional faint bright row assigned to in-plane titanium. This cannot be explained by a peculiar tip shape, as atomic size defects are present in the oxygen rows. None of them has a duplicate at a titanium row. Furthermore, the observed contrast is independent of the scan direction as indicated in Fig. 3.7.
The forward and backward images presented in Fig. 3.7 are depicted with identical color scale. Obviously, they reveal a slightly different overall detuning. The detuning difference between backward and forward image was approximately 0.5 Hz. This difference most likely results from a hysteretic scanner movement due to slow distance feedback loop settings. The sample was measured to be tilted by an angle of about 0.7 ° as shown in Fig. 3.9. This tilt angle corresponds to a total tilt of 60 pm of the images presented in Fig. 3.7. Thus, true constant height measurement was impossible. Consequently, the distance feedback loop was allowed to compensate for the tilt and also for vertical thermal drift. This was achieved by using a very slowly reacting feedback to maintain quasi-constant height conditions at the atomic scale. A slowly reacting feedback is inert and does per default not exactly follow a given topography.

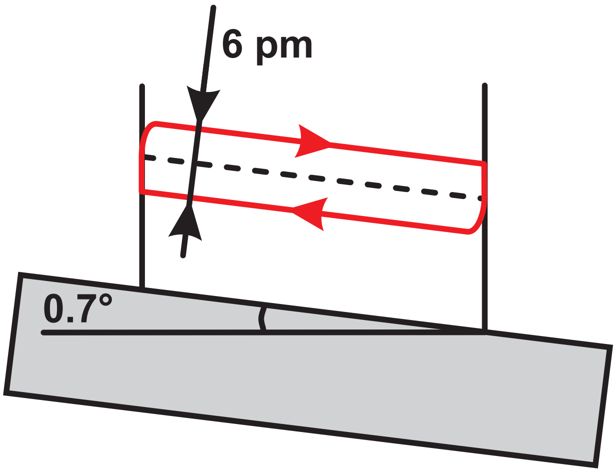

Figure 3.9: *The tip-sample distance in Fig. 3.7 is different in the forward and the backward image by about 6 pm. This is caused by a tilted sample and slow distance feedback loop settings. The inert feedback is not able to keep the initial tip-sample distance (indicated by dashed line) constant. Instead, the tip-sample distance is larger in forward and smaller in backward direction (red line). The tilt angle of 0.7° corresponds to a total tilt of 60 pm of the images in Fig. 3.7. Tilt angle and width of hysteresis are drawn exaggerated in the sketch.*

In the images depicted in Fig. 3.7, the sample was tilted as shown in Fig. 3.9. Thus, the scanner was further away from the sample while scanning in forward direction and closer to the surface in backward direction. The difference in height was measured to be about 6 pm. This resulted in an overall difference in detuning of 0.5 Hz. Note that although the tip-sample distance is different in forward and backward direction, each single image is scanned in quasi-constant height mode, respectively.

Subsurface impurity

Fig. 3.8 reveals a fourth defect species that has been introduced as subsurface impurity in an STM study of Batzill et al. [45]. The nature of this defect is unclear so far. This defect type has been furthermore reported by Zhang et al. and Enevoldsen et al. in STM and NC-AFM studies, respectively [39, 44]. The defect is imaged in STM as a circular region, where the titanium rows are brighter than usual. This led to the assumption that the subsurface impurity is a positive charge, which leads to a higher tunneling current in that region [45]. The NC-AFM image obtained by Enevoldsen et al. in neutral mode revealed protruding oxygen rows at the defect site [44].

Here, I present images that show the consequences of the subsurface impurity on both, the oxygen as well as the titanium rows, simultaneously. In my images, the subsurface defect manifests as regions, where the bridging oxygen atoms appear lowered and titanium rows protrude the bridging oxygen rows. A detailed investigation is depicted in Fig. 3.10. Line profiles along neighboring titanium and bridging oxygen rows above a subsurface defect site exhibit a contrast inversion at that site. The detuning on the bridging oxygen row is lowered by about the same value as the detuning increases on the titanium row. An overall electrostatic offset as suggested in [45] would change the detuning in the same direction at all sites within the circular region. Thus, a charge patch could hardly be the origin of the observed circular phenomenon.

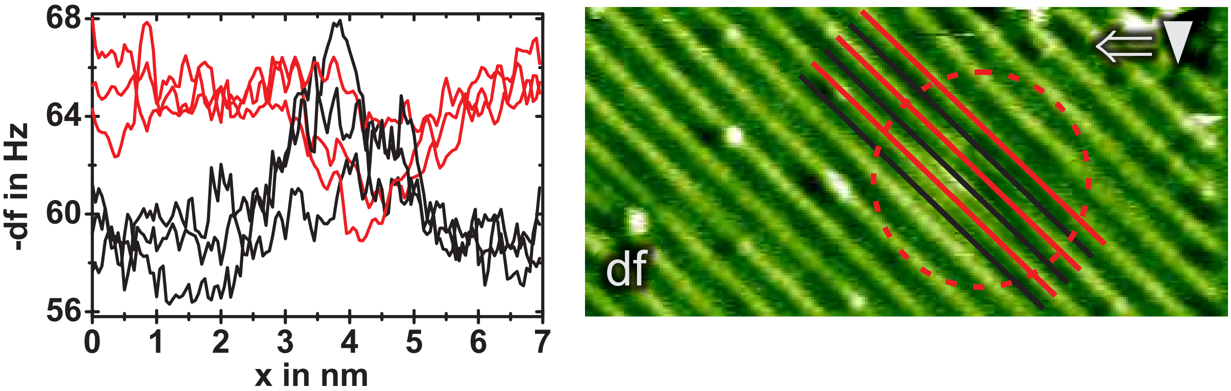

Figure 3.10: *NC-AFM detuning image obtained on $TiO_2(110)$ in all-inclusive mode. A subsurface impurity is marked by a red dashed circle. Line profiles at neighboring bridging oxygen rows (red lines) as well as titanium rows (black lines) are shown in the graph. The detuning at bridging oxygen sites is lowered by about 5 Hz above the center of the defect. At titanium sites the detuning is increased by approximately 7 Hz. Thus, an overall electrostatic offset is hardly the origin of the observed circular phenomenon.*

Contrast changes

As already mentioned, numerous contrast changes between all four presented contrast modes were observed. Here, I will discuss a particular experimental session in detail, where 10 to 20 contrast changes between neutral and all-inclusive mode were observed.

The observed contrast changes do not coincide with dramatical changes in tip-sample distance as usually observed when the tip drops atoms or clusters to the surface or picks

up adsorbates from the sample surface. Furthermore, taking the large number of observed contrast changes into account, the two tips responsible for neutral and all-inclusive mode have to be connected by a very likely transition.
Fig. 3.11(a) shows an example of such a contrast change.

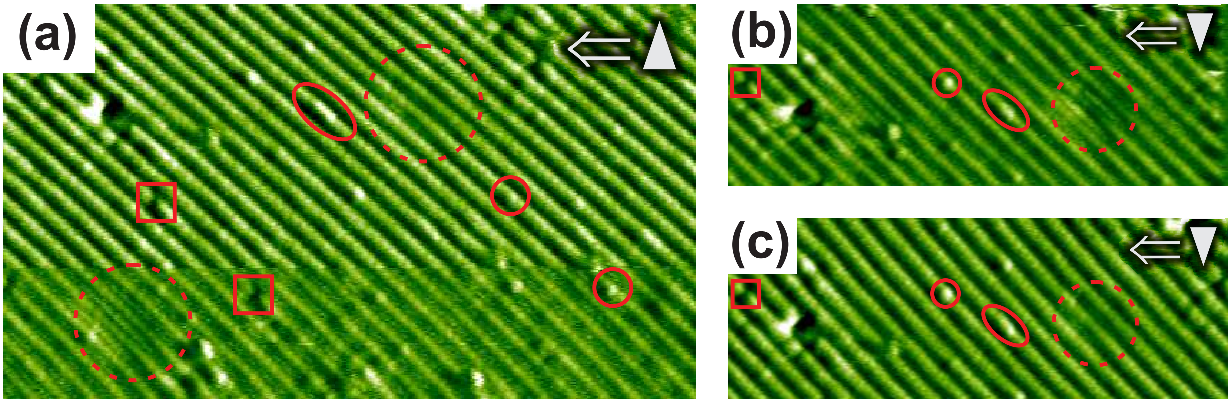

Figure 3.11: *NC-AFM detuning images observed on TiO_2(110). (a) shows a typical example of a contrast change from all-inclusive to neutral mode. In (b) and (c) consecutively obtained images are presented that show an identical surface area in all-inclusive and neutral mode, respectively. Vacancies (red squares), single (red circles) and double (red ellipses) hydroxyls as well as subsurface impurities (red dashed circles) are indicated. The images are presented in identical color scale, revealing that the overall detuning as well as the qualitative contrast between bridging oxygen and the four defect species are the same in both modes.*

The lower part of the image reveals the all-inclusive contrast, in the upper part the neutral mode is observed. In Fig. 3.11(b) and (c) consecutively obtained images are presented that show an identical surface area in all-inclusive and neutral mode, respectively. All presented images contain all four defect species that were discussed so far. Hence, the appearance of all surface sites in both contrast modes can be directly compared from this images. The images are depicted with identical color scale. As already mentioned, the appearance of bridging oxygen and defect sites is qualitatively the same in neutral and all-inclusive mode.
In Fig. 3.12 line profiles perpendicular to the [001] direction before and after a contrast change from neutral to all-inclusive mode are presented. They clearly show that the detuning at oxygen sites remaines virtually unchanged upon contrast change. However, the detuning at the titanium site changes dramatically by about 8 Hz.
The detuning values for titanium, bridging oxygen, vacancy and hydroxyl sites in both contrast modes observed in consecutively recorded images in this particular session are given in Tab. 3.1. A careful analysis reveals that the detuning at vacancy and hydroxyl sites slightly changes upon contrast change.

site	neutral mode	all-inclusive mode	difference
Ti	-53 Hz (0 Hz)	-61 Hz (-8 Hz)	8 Hz
$O_{bridging}$	-65 Hz (-12 Hz)	-65 Hz (-12 Hz)	0 Hz
vac	-58 Hz (-5 Hz)	-57 Hz (-4 Hz)	-1 Hz
OH	-70 Hz (-17 Hz)	-68 Hz (-15 Hz)	-2 Hz

Table 3.1: *Measured detuning values in neutral and all-inclusive mode for titanium (Ti), bridging oxygen ($O_{bridging}$), vacancy (vac) and hydroxyl (OH) sites, obtained from a series of consecutively recorded images. The values in brackets represent the detuning due to short-range interaction. They are obtained by substracting an offset that is supposed to be due to long-range interaction (see Fig. 3.13) of -53 Hz. The error of the detuning values is 1 Hz.*

The absolute detuning values at various surface sites are in the range of -50 Hz to -70 Hz. However, the corrugation is less than 20 Hz. Thus, the main contribution to the detuning is very likely due to long-range interaction which is specific for the macroscopic shape of the particular tip but of less importance for the comparison of the two contrast modes. To eventually separate the detuning due to site-specific short-range interaction from the overall detuning offset, the distance-dependent detuning corrugation was analyzed. Therefore, in Fig. 3.13 the very first image of this experimental session is shown. The length of a scan line was decreased from 500 nm in the lower part of the image to 20 nm in the upper part, while the tip-surface distance was successively decreased. In the line profile along the slow scan direction the resulting increase in overall detuning can be followed.

In the lower half of the image, only step edge sites are resolved, while the terraces are uncorrugated. The typical row structure is first observed after an increase of the detuning to about -50 Hz as indicated by the red dashed line. Thus, the detuning due to long range interaction might be estimated to be at least -50 Hz. As the interaction between neutral tip and titanium site (measured detuning value -53 Hz) is assumed to be negligible, the long-range offset can in good approximation be assumed to be -53 Hz in this particular experiment. Hence, the detuning values measured in this experiment were corrected for

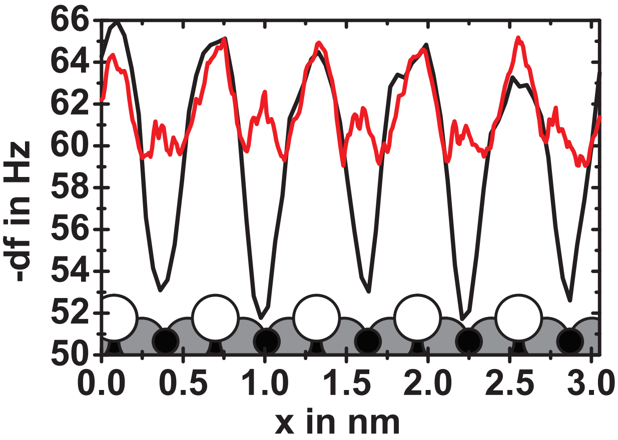

Figure 3.12: *Line profiles from consecutive NC-AFM detuning images obtained on $TiO_2(110)$ in neutral (black) and all-inclusive (red, 3 pxl average) mode. The detuning at oxygen sites remain unchanged upon contrast change. The detuning at titanium site changes by about 8 Hz.*

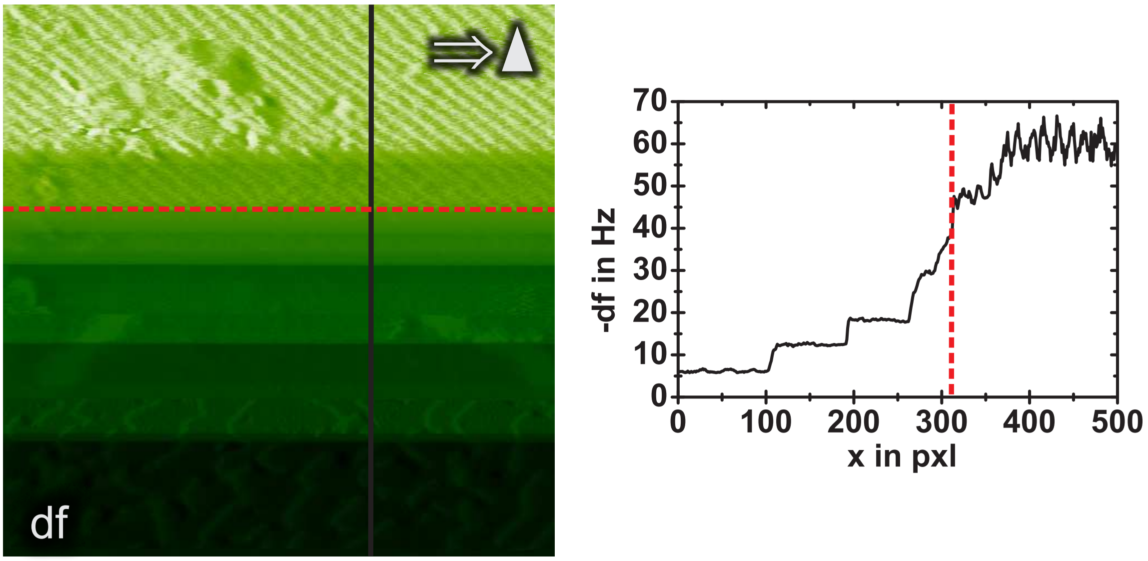

Figure 3.13: *NC-AFM detuning image obtained on* TiO_2*(110). This image represents the very first image of the discussed session, revealing the tip-sample distance dependency on detuning and detuning corrugation. The scan line length was decreased from 500 nm in the lower part of the image to 20 nm in the upper part. At the same time, the tip-surface distance was successively decreased. The line profile along the slow scan direction reveals the resulting increase in detuning. The initial appearance of atomic structures (indicated by red dashed line) coincides with an increase in detuning to about -50 Hz.*

this offset in Tab. 3.1.

The corresponding dissipation image to the detuning image presented in Fig. 3.11(a) is shown in Fig. 3.14. Besides the change in detuning contrast, also a small change in dissipation is observed as indicated by the line profiles.

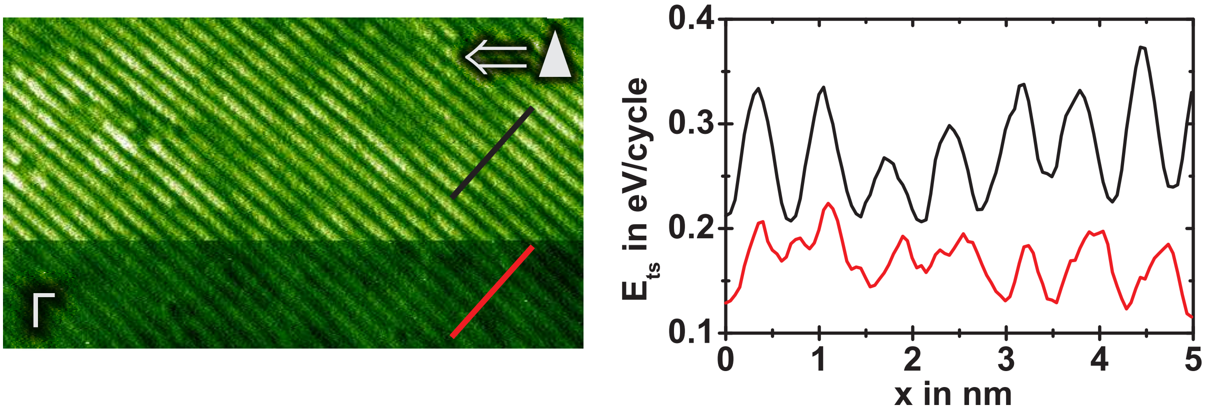

Figure 3.14: *NC-AFM dissipation image corresponding to the detuning image presented in Fig. 3.11(a). The line profiles depict the site specific energy dissipated due to tip-sample interaction* E_{ts} *in all-inclusive (red line) and neutral (black line) mode.* E_{ts} *was calculated according to Eq. 2.4 with* $k = 30\,\frac{N}{m}$, $A = 10\,nm$ *and* $Q = 21,200$. *The dissipation of the freely oscillating cantilever was measured to be* $\Gamma_0 = (1.5 \pm 0.1)\,V$, *corresponding to an internal energy loss of about 2.78 eV per oscillation cycle.*

Upon contrast change from all-inclusive (red line) to neutral (black line) mode the energy dissipated due to tip-sample interaction E_{ts} changed as follows. In all-inclusive mode E_{ts} was measured to be about 0.13 eV at the titanium site and 0.19 eV at the bridging oxygen site per oscillation cycle, respectively. At the change to neutral mode, E_{ts} at titanium and bridging oxygen site was measured to be increased to 0.21 eV per cycle and 0.33 eV per cycle, respectively. Thus, E_{ts} is found to be increased by 0.09 eV per cycle in average in neutrale mode and the corrugation was twice as large as in all-inclusive mode. Note for comparison that the freely oscillating cantilever dissipated 2.78 eV per oscillation cycle.

Based on the detailed detuning and dissipation data presented here, neutral and all-inclusive mode contrasts can now be simulated by a theoretical approach. In order to gain detailed insight into the nature of the tips responsible for these two contrasts, a co-operation with C. González, P. Jelínek [2] and R. Pérez[3] was started to model reliable pairs of tips by density-functional theory calculations. From this interplay between experiment and theory the observed contrast as well as changes between different contrast modes can be understood in great detail.

---

[2] both from the Institute of Physics, Academy of Sciences of the Czech Republic, Prague, Czech Republic

[3] Departamento de Física Teórica de la Materia Condensada, Universidad Autónoma de Madrid, Spain

4 Doped titanium dioxide

Photocatalysts find highly important applications in the degradation of toxic compounds [46] and in the production of hydrogen fuel [47–49] free from CO_2 release when driven by solar light. Wide band gap photocatalyst like TiO_2 are sensitized to visible light by doping with foreign elements [50]. Non-metallic dopants including carbon [51], nitrogen [52], fluorine [53], phosphorus [54] and sulfur [55] have been examined and found to be active in visible-light induced reactions. Despite the successful sensitization, the nature of visible-light absorption is still under discussion. Band gap narrowing [52], electronic transition from mid-gap states localized on dopants [53, 56], and formation of oxygen anion vacancies as color centers [57, 58] have been proposed to induce the visible-light absorption.

Doping with transition metals has been reported to provide visible-light absorption more intense than with non-metalic dopants [59]. The formation of oxygen vacancies has again been proposed with doping transition metals. With Cr^{3+} dopants substituting Ti^{4+} cations, oxygen vacancies have been supposed to appear to balance the ionic charge in the doped TiO_2 [47]. On the other hand, experimental evidence for dopant-induced formation of oxygen vacancies has not been provided so far.

Although chromium-doped titania has revealed high visible-light absorption in reflection spectroscopy measurements [60], it has been found to be photocatalytic inactive. Photoinduced electrons and holes have been suggested to readily recombine at Cr^{6+} and oxygen vacancy sites. In contrast, chromium and antimony codoped titania has revealed both, visible-light absorption as well as photocatalytic activity, when the antimony concentration at least equals the concentration of chromium. This has been explained by the creation of an equal amount of Cr^{3+} and Sb^{5+} cations balancing the charge with no need for the creation of oxygen vacancies or Cr^{6+} species [60, 61].

In order to gain insight into the physico-chemical mechanisms of transition metal doping, a detailed knowledge of doping-induced structural changes is mandatory. In this chapter, I report on NC-AFM investigation of chromium and antimony-doped $TiO_2(110)$. The main interest of this study was to investigate the influence of transition metal doping on the surface structure of rutile $TiO_2(110)$.

Experimental details

Three $TiO_2(110)$ samples of the same kind as those, used for the study of pristine titania were doped[1] with chromium and antimony at different dopant ratios. For this purpose, the samples were sent to the lab of Prof. Hiroshi Onishi at Kobe University, Japan. The samples were doped with chromium and antimony by calcining them together with Cr_2O_3 and Sb_2O_3 powder, respectively, in a crucible at 1420 K for 10 h in ambient conditions as described in [60]. The following dopant ratios were produced:

---

[1] doping was performed by Mitsunori Kitta, Department of Chemistry, Kobe University, Kobe, Japan

- $TiO_2(110)$ sample doped with chromium solely
- $TiO_2(110)$ sample codoped with chromium and antimony of equal amounts
- $TiO_2(110)$ sample doped with antimony solely

After shipping the samples back to Osnabrück, each sample was mounted to an Omicron sample holder, transferred into the load-lock chamber and baked at approximately 400 K overnight to remove water from sample and sample holder. After insertion into the UHV, the samples were prepared by repeated cycles of Ar^+ ion sputtering and subsequent annealing. Five initial cycles of preparation consisting of sputtering and subsequent annealing were applied to all samples prior to the respective first AFM measurement session. For comparability, the samples were treated exactly the same way as the pristine titania samples. In consecutive preparation cycles, annealing temperature and duration were varied as shown in Tab. 4.1 to investigate the influence of the annealing procedure on the observed surface structure.

cycle	Cr	Cr + Sb	Sb
1^{st} to 5^{th}	15 min at 1100 K	15 min at 1100 K	15 min at 1100 K
6^{th}	15 min at 1100 K -	15 min at 930 K 1 h at 930 K	15 min at 1100 K -
7^{th}	15 min at 1100 K - -	1 h at 500 K 1 h at 930 K 13 h at 930 K	15 min at 1100 K - -
8^{th}	1 h at 930 K	16 h at 500 K	1 h at 930 K
9^{th}	-	1 h at 930 K	-

Table 4.1: *Annealing duration and temperature for the doped titania samples. Each cycle starts with 15 min of Ar^+ ion sputtering with a kinetic energy of 1 keV at an argon partial pressure of $3 \cdot 10^{-6}$ mbar.*

Photographs of the samples before and after vacuum treatment were taken. They are shown in Fig. 4.1. For comparison, a fresh and a vacuum prepared pristine titania sample (Fig. 4.1(a)) are shown as well. Titanium dioxide has a band gap of about 3 eV [62] and is, therefore, transparent. However, it is known to become dark blue [1] upon reduction when prepared under vacuum conditions [13]. Obviously, chromium doping also changes the color of the sample to a brownish appearance, confirming the measured visible-light absorption. On the other hand, the freshly doped antimony sample appears virtually identical to the fresh pristine sample. This strongly indicates that the doping procedure does not reduce the bulk per default. The slightly bluish color of the vacuum-treated antimony-doped sample furthermore points to a reduction process upon UHV treatment of the doped samples, similar to what is observed at the pristine titania sample. Unfortunately, the codoped sample was not photographed before UHV treatment, but had a quite similar color as after preparation as depicted in Fig. 4.1(d).

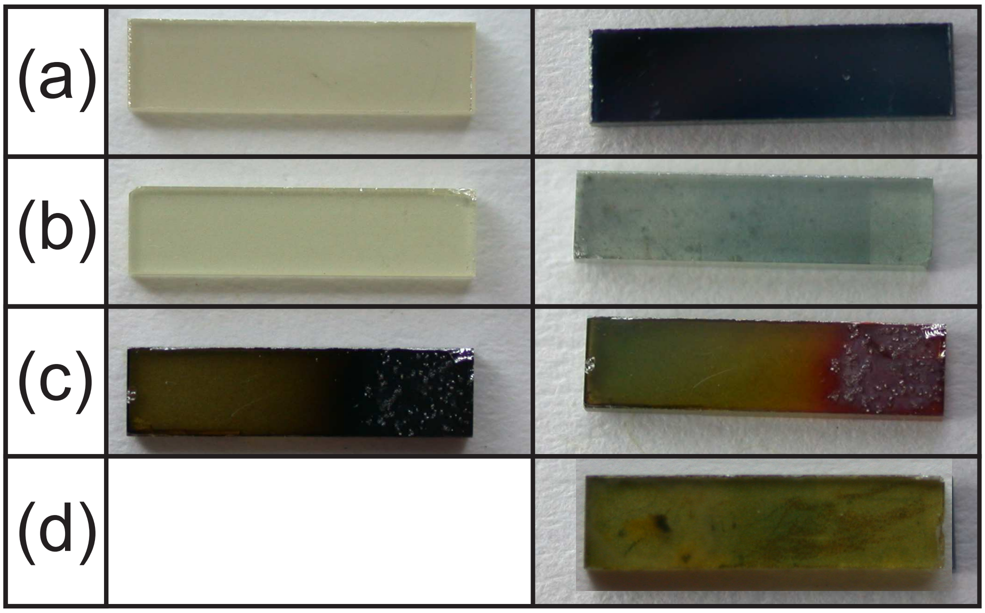

Figure 4.1: *Photographs of the pristine (a), antimony-doped (b), chromium-doped (c) and the codoped (d)* TiO_2*(110) sample before (left) and after (right) preparation in UHV. The pristine sample was treated by about 30 cycles of sputtering and annealing. The doped samples were treated as depicted in Tab. 4.1.*

The total amount of chromium and antimony in the doped samples is difficult to quantify. The concentration is expected to be highly inhomogeneous over the cross section of the sample. With increasing depth, the dopant concentration most likely drops to zero. However, in the upper few micrometers of the sample, the dopant concentration might be expected to be similar to what has been found in doped titania powder. There, the chromium and antimony concentration is known to be in the order of 2 to 3 atom percent, each [61], when using the same doping recipe. The dopant ratio in the codoped sample is intended to be close to unity with a small amount of excess antimony.

4.1 Chromium-doped TiO_2(110)

The first sample discussed here is the chromium-doped TiO_2(110) sample. As already mentioned, the chromium concentration is expected to be 2 to 3 atom percent in the upper few micrometers. The morphology of the surface at the micrometer length scale after annealing at 1100 K is depicted in Fig. 4.2(a) and (b). In contrast to the equally stepped surface of pristine TiO_2(110) prepared in identical manner, the doped surface is rather inhomogeneously stepped. Pristine titania usually exhibits terraces of rather similar width. Here, flat terraces extending over several 100 nm and step bunching, resulting in steep slopes of more than 10 nm of height (Fig. 4.2(c)) coexist side by side. This finding holds for both annealing recipes applied to this sample (see Tab. 4.1). Thus, a lack of thermal energy does not seem to be responsible for the inhomogeneous morphology. The terraces are covered by a dense layer of protruding stripe-like features as shown in Fig. 4.2(d).

Fig. 4.3 shows a series of topography images recorded subsequently upon decreasing the

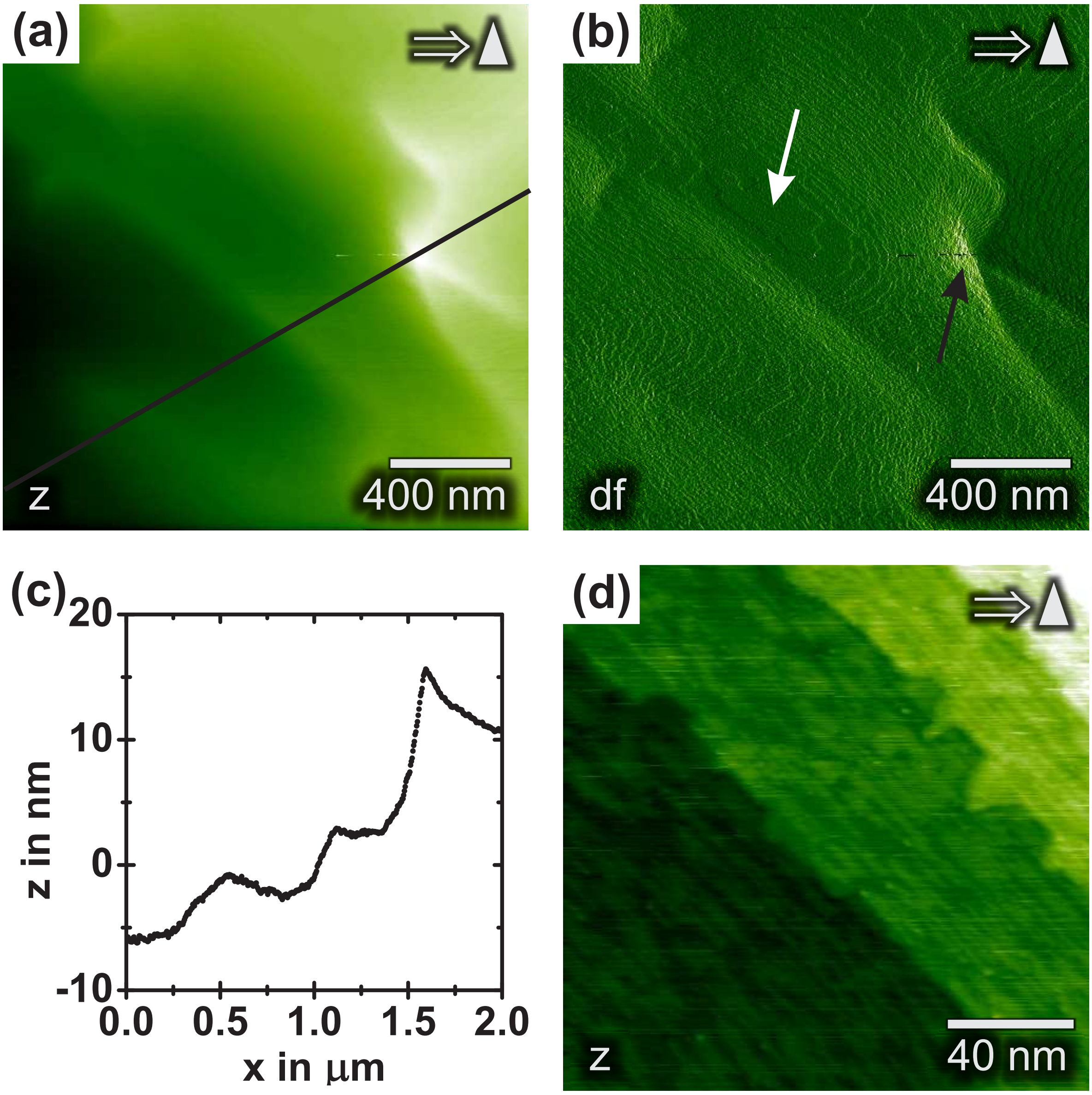

Figure 4.2: *NC-AFM images of chromium-doped* $TiO_2(110)$ *after annealing at 1100 K. A typical topography image (a) and the corresponding detuning image (b) of large frame size is shown to receive an impression of the surface corrugation. The images reveal the coexistence of flat terraces that extend over several 100 nm (white arrow) and steep slopes due to step bunching (black arrow) of more than 10 nm of height as indicated by the height profile along the black line (c). All terraces are found to be covered by a dense layer of stripes (d). The images are obtained after the 5th preparation cycle.*

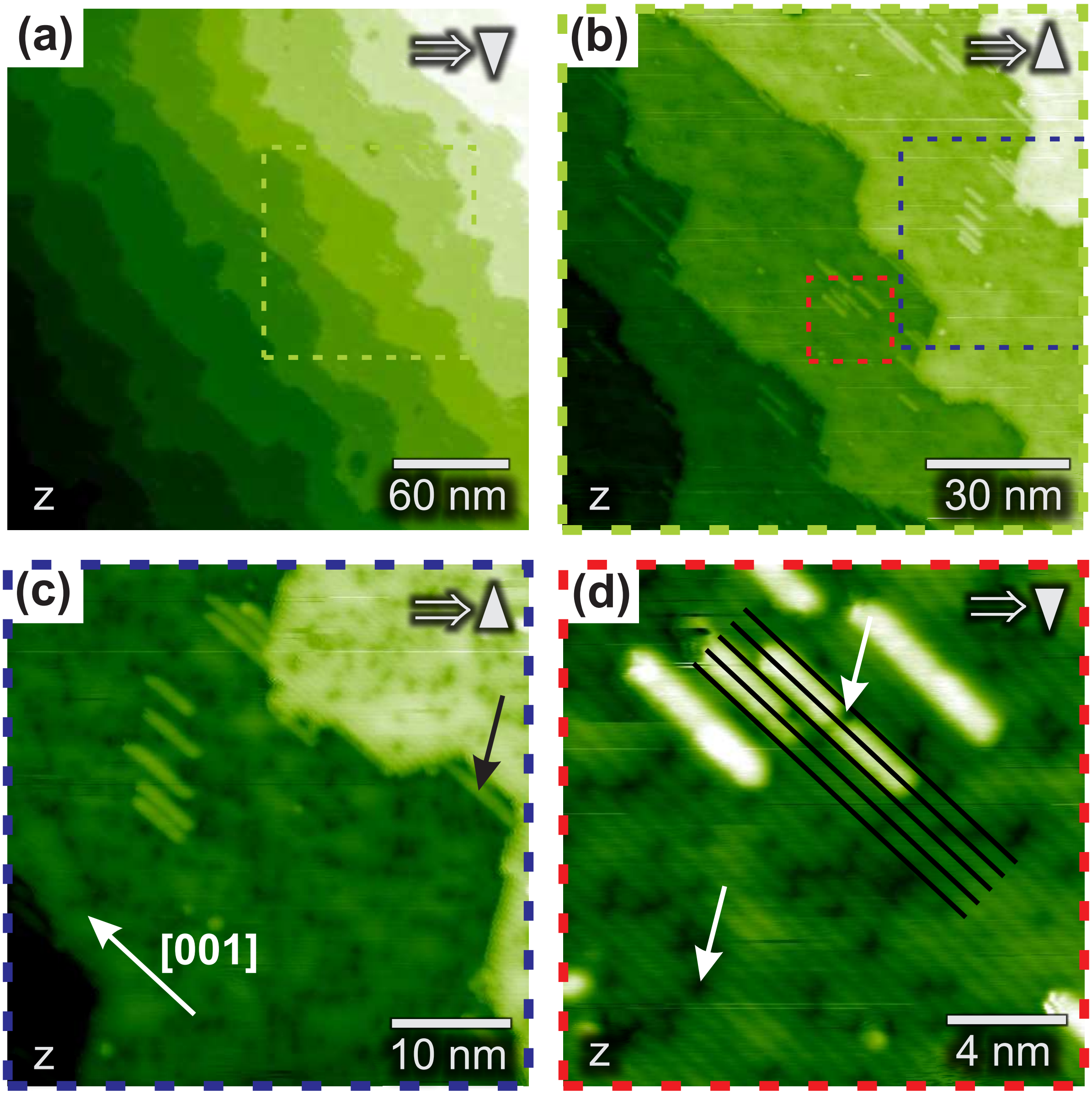

Figure 4.3: *Subsequently taken topography images of chromium-doped* $TiO_2(110)$*. In (a) the step height was measured to be (340 ± 30) pm. All stripes are aligned in [001] direction (b). Although some stripes are growing from step edges or even connect them (black arrow), the majority of stripes is found on the terraces (c). In images of small size (d), a large number of hydroxyls can be identified as dark features in bright oxygen rows. Two of them are indicated by white arrows; one interrupting a stripe feature and one on the bare terrace. The stripes are centered on titanium rows. The images are obtained after the 7th preparation cycle.*

frame size. At medium frame size (Fig. 4.3(a)), the typical appearance of pristine TiO_2(110) is observed. The step height was measured to be (340 ± 30) pm, which is within the error identical to what was found on undoped titanium dioxide. Besides the typical TiO_2(110) appearance, a number of additional stripes can be identified in Fig. 4.3(b). In Fig. 4.2, obtained after the 5th preparation cycle, they emerged as dense layer of stripes on all terraces. Here, after the 7th preparation cycle they emerge as groups of few. These stripes appear as protrusions and are exclusively aligned along [001] direction. They are observed to have a length of 5 to 10 nm. Although few stripes grow from step edges, the majority of the stripes are found on the terraces.
At small frame sizes (Fig. 4.3(c)), the substrate atoms become visible as bright rows. These rows are disrupted by dark features originating from atomic size defects (Fig. 4.3(d)). This contrast mode has been reported before and referred to as hole mode [10]. Based on this assignment, the bright rows can be identified as bridging oxygen atoms, the dark rows as titanium atoms and the dark defects in the bright rows as hydroxyls. See for comparison Fig. 3.5. The distance of the bridging oxygen rows was measured to be (630 ± 20) pm. Within the error, this corresponds to the lattice distance of TiO_2(110) (see Fig. 3.1).

Stripe feature

From Fig. 4.3(d) it is obvious that the bright stripes are always centered on titanium rows overlapping the neighboring oxygen rows. One probable explanation for the stripes could be that they consist of reduced titania Ti_2O_3 as observed on samples that have been annealed at higher temperatures [42]. These Ti_2O_3 rows have been reported to be precursors of the (1×2) reconstructed surface. Although the appearance of the stripes presented here is very similar to the known Ti_2O_3 rows, three strong arguments exist against this assumption.

First of all, the annealing temperature in the present experiments was exactly the same as in our previous experiments on pristine titania, which never resulted in the formation of reduced Ti_2O_3 rows.
Second, when reducing the tip-sample distance to obtain better resolution it was often observed that the stripe features were moved on the substrate. This points towards a rather weak interaction of the stripes with the substrate, contradictory to what is expected for Ti_2O_3 on top of TiO_2.
Third, the fact that the density of stripes is reduced upon further preparation is the strongest argument against the assignment of the rows being Ti_2O_3. Titanium dioxide is known to become slightly reduced by sputtering and annealing under vacuum conditions. Further reduction would lead to an increasing amount of material consisting of reduced titania, eventually resulting in a (1×2) reconstructed surface. In contrast, in the experiment presented here, the number of stripe features on the doped surface was observed to be massively reduced by repeated preparation. In Fig. 4.4 four images of a doped sample, subjected to increasing number of preparation cycles are presented for evidence. While the surface exhibits a dense layer of stripes after the 5th cycle (Fig. 4.4(a)), only few remained after 8 preparation cycles (Fig. 4.4(d)).
Hence, the stripes are hardly Ti_2O_3 features. It will be found that these stripes most likely consist of Cr_2O_3 as discussed later.

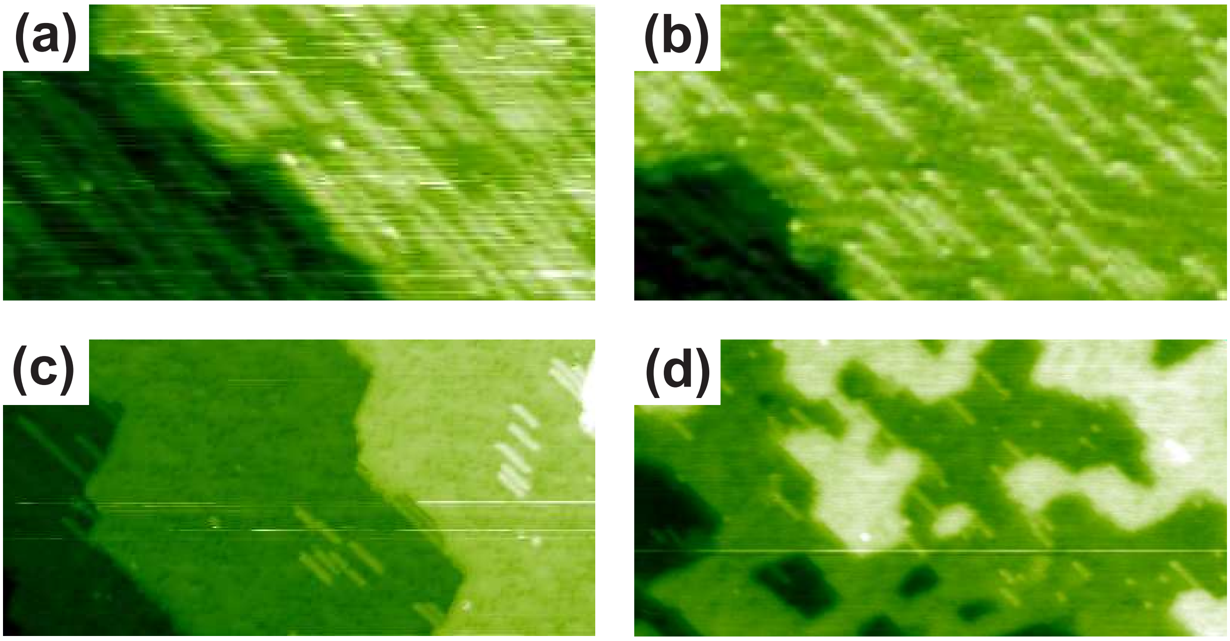

Figure 4.4: *NC-AFM topography images obtained on chromium-doped* TiO_2*(110). The frame size is 88 nm by 44 nm. The images were recorded after the* 5^{th} *cycle (a),* 6^{th} *(b),* 7^{th} *(c) and* 8^{th} *(d) preparation cycle. Obviously, the density of stripes is massively decreased upon UHV preparation.*

Hydroxyl density

Now, I will take a detailed look at the density of the dark holes within the bright oxygen rows, which can be assigned to single hydroxyl defects. These hydroxyls are known to evolve from oxygen vacancies. From one oxygen vacancy, two hydroxyls are created upon water adsorption [9]. As indicated in Fig. 4.3(d) the hydroxyls are observed to be homogeneously distributed. From a statistical analysis I quantified the density of hydroxyls to be (4.9 ± 0.6) %ML after seven cycles of sputtering and annealing (100 %ML corresponds to one hydroxyl per surface unit cell). As two hydroxyls are formed from one oxygen vacancy, the measured hydroxyl density corresponds to an initial oxygen vacancy density of (2.45 ± 0.30) %ML. This value can be compared to what we usually observe on undoped TiO_2(110). From an extended defect density study in dependence on preparation duration accomplished on pristine titanium as presented in Fig. 3.2, the vacancy density is expected to be in the order of (0.45 ± 0.30) %ML after seven cycles of preparation [40]. Thus, in the present experiments the vacancy density is strikingly larger than what is commonly observed on pristine TiO_2(110). Even when considering the rather large error bars of the density measurement, the present vacancy density remains to be at least 1.40 %ML too high. Thus, the additional defects cannot be explained by the sample preparation procedure, but must be associated with the calcination process. Note that calcination in air during the doping procedure does not per default reduce the bulk as indicated by the appearance of the antimony-doped sample in Fig. 4.1.

Before I present a simple model that explains the reason for the creation of extra oxygen vacancies during the calcination process, the oxidation state of chromium dopants in chromium-doped TiO_2 has to be considered. The oxidation state of chromium is most

likely either Cr^{3+} or Cr^{6+}. Chromium atoms replace Ti^{4+} in the titanium dioxide bulk. If either Cr^{3+} or Cr^{6+} exists solely in the doped sample, the crystal would be negatively or positively charged, respectively. Hence, the oxidation state of chromium has to be heterogeneous in chromium-doped TiO_2. This fact has been proven by Ikeda et al. [60].
Charging could be easily avoided without the creation of oxygen vacancies as illustrated by

$$3\ \mathrm{Ti}^{4+} \longrightarrow \mathrm{Cr}^{6+} + 2\ \mathrm{Cr}^{3+}.$$

This formula[2] indicates that one out of three chromium atoms replacing titanium atoms needs to be in Cr^{6+} state for maintaining charge neutrality. The other two chromium atoms are in the oxidation state Cr^{3+}. As the sum of oxidation states is equal $(3 \cdot 4 = 6 + 2 \cdot 3)$ before and after the replacement, the crystal remains uncharged upon doping.
Nevertheless, charge compensation is only one requirement for crystal stability. Another very important issue is minimization of stress due to lattice mismatch. For the situation illustrated above, a mean ionic radius of 55.7 pm can be estimated for the three chromium dopants from the ionic radii given in Tab. 4.2.

cation	ionic radius
Ti^{3+}	67.0 pm
Ti^{4+}	60.5 pm
Cr^{3+}	61.5 pm
Cr^{6+}	44.0 pm

Table 4.2: *Ionic radii of metal ions [63].*

The dopants replace Ti^{4+} with an ionic radius of 60.5 pm, resulting in a mean ionic radius mismatch of about 8 %. Even so these numbers must not be taken too literally, this model does, indeed, indicate that the situation above might be unfavorable although the charge is fully compensated.
It can be directly seen from Tab. 4.2 that the ionic radii of Cr^{3+} and Ti^{4+} are very similar. Hence, the lattice mismatch results from the fact that the ionic radius of Cr^{6+} is much smaller than that of Ti^{4+}. To compensate for this small ionic radius, a species with an ionic radius larger than that of Ti^{4+} is needed. Obviously, Ti^{3+} is such a candidate. Considering the creation of Ti^{3+} during the calcination process, the formula introduced above has to be modified as follows to maintain charge neutrality

$$3\ \mathrm{Ti}^{4+} \longrightarrow \mathrm{Cr}^{6+} + \ (2-\mathrm{n})\,\mathrm{Cr}^{3+} + \ \mathrm{n}\ \mathrm{Ti}^{3+}$$

where $n \in [0, 2]$. This formula shows that Ti^{3+} instead of Cr^{3+} or a mixture could be responsible for charge compensation.
In the bulk, Ti^{3+} might be formed by charge redistribution from chromium to bulk titanium. In the surface layer, Ti^{3+} can also be created by loss of oxygen. A single oxygen vacancy is created by the loss of a neutral oxygen atom, reducing the two adjacent titanium atoms from Ti^{4+} to Ti^{3+} state. As these two Ti^{3+} are intrinsically tied to one vacancy,

---

[2] The arrow (→) in this and all following formulas means ”is replaced by”.

n Ti^{3+} in the preceeding formula represent $\frac{\mathrm{n}}{2}$ vacancies (vac) in the surface layer. Thus, one ends up with

$$3\ \mathrm{Ti}^{4+} \longrightarrow \mathrm{Cr}^{6+} +\ (2-\mathrm{n})\,\mathrm{Cr}^{3+} +\ \frac{\mathrm{n}}{2}\ \mathrm{vac.}$$

The mean ionic radius mismatch of this situation can be estimated according to the values from Tab. 4.2 as a function of the parameter n. The result is given in Fig. 4.5. To be more illustrative, I do not plot the ionic radius mismatch against n itself, but against the ratio of vacancy density to chromium density $[\mathrm{vac}]/[\mathrm{Cr}] = \frac{\mathrm{n}}{2(3-\mathrm{n})} \in [0,1]$. At a given n, also the ratio $[\mathrm{Cr}^{3+}]/[\mathrm{Cr}^{6+}] = (2-\mathrm{n})$ is a fixed value for maintaining charge neutrality. This curve is also given in Fig. 4.5.

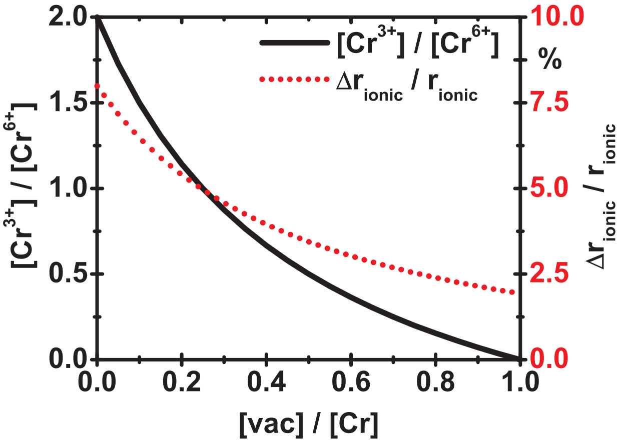

Figure 4.5: *Atom concentration ratio of chromium atoms of different oxidation state* $[\mathrm{Cr}^{3+}]/[\mathrm{Cr}^{6+}]$ *(black, solid line) and mean ionic radius mismatch (red, dotted line) in dependence on the [vac]/[Cr] ratio. The whole range of possible mixtures maintaining charge neutrality is shown.*

Now, two extreme situations can be distinguished: $n = 0$ (no Ti^{3+}) and $n = 2$ (no Cr^{3+}). It is obvious from Fig. 4.5 that the ionic radius mismatch is maximal (approximately 8 %) in the absence of Ti^{3+}. Thus, this is the most unlikely situation. However, lattice stress will be reduced by increasing the amount of Ti^{3+}. As a result, the amount of Cr^{3+} decreases to maintain charge neutrality.

This simple model predicts that all chromium atoms should be in 6+ state for minimizing the lattice stress, although it is known from spectroscopy that this is not the case [60]. Still, this model indicates why additional oxygen vacancies are created during the calcination process in the chromium-doped sample. Moreover, my model allows for giving a rough estimation for the vacancy concentration. Assuming a tolerable lattice mismatch of 3 % at highest, the model predicts that the concentration of vacancies should be of the same order of magnitude as the total amount of chromium: $[\mathrm{vac}]/[\mathrm{Cr}] \geq 0.5$, which is equivalent to $n \geq 1.5$. Interestingly, the prediction of this simple model exactly matches the findings of the experiment. While the total amount of chromium is expected to be in the order of 2 to 3 atom percent (at least in the upper few layers), the vacancy density of the freshly doped sample was found to be at least 1.4 %ML. This corresponds to a ratio [vac]/[Cr] of more than 0.5, as predicted by the model.

Another fact strongly supporting the presented model is the finding that no enhanced density of oxygen vacancies was observed on the surface of $\mathrm{TiO}_2(110)$ codoped with chromium

and antimony as will be shown in the next section. In that sample, the charge neutrality is provided by equal amounts of Cr^{3+} and Sb^{5+}. The ionic radii of these ions are 61.5 pm and 60.0 pm, respectively [63]. Both values are very close to the radius of Ti^{4+}, resulting in virtually no mismatch. Eventually, charge redistribution to titanium is not necessary, therefore no additional oxygen vacancies are found on that surface.
Assuming the presented model to be correct, what happens if the sample is prepared in UHV? Sputtering and annealing under UHV conditions is known to reduce titanium dioxide [9], which leads to an even higher oxygen vacancy concentration. To maintain charge neutrality, an equal amount of Cr^{3+} has to leave the bulk, restoring the ratio $\frac{[Cr^{3+}]+[Ti^{3+}]}{[Cr^{6+}]} = 2$. This explains why Cr_2O_3 features are found on the surface. These Cr_2O_3 stripes are favorably sputtered during following preparation cycles. Consequently, two parallel processes are taking place at the same time. First, the density of oxygen vacancies is increased by sputtering and annealing. A vacancy concentration of 2.45 %ML was already reached in the experiment. Second, as a direct result, the amount of chromium is decreased upon following sputtering cycles, as Cr_2O_3 is removed from the surface. Both processes will lead to the situation where the density of vacancies and the density of chromium dopants near the surface is equal, which corresponds to $[vac]/[Cr] = 1$ in Fig. 4.5. Hence, all chromium atoms in the upper bulk layers will be in the 6+ state. Then, seggregation of Cr^{3+} to the surface will end and following preparation cycles will remove the remaining Cr_2O_3. This explains why the density of Cr_2O_3 stripes decreases upon further preparation as indicated in Fig. 4.4.

Summary

In conclusion, I have investigated the (110) surface of rutile TiO_2 doped with 2 to 3 atom percent chromium by NC-AFM. The surface lattice parameters were observed to be very similar to that of pristine titanium dioxide. Nevertheless, two main differences were observed: First, a number of stripe-like features centered on top of titanium rows and aligned in [001] direction were found. These stripes can be assigned to Cr_2O_3 that evolves from Cr^{3+} segregating to the surface as a direct result from bulk reduction by UHV preparation. Second, the density of oxygen vacancies was found to be drastically increased compared to pristine TiO_2, indicating that oxygen vacancies are created during the calcination process. A simple model is presented that accounts for these experimental findings. The model is based on reducing lattice stress while maintaining charge neutrality at the same time. As a result, only a minority of chromium atoms in chromium-doped TiO_2 can be in the 3+ state. It has to be discussed whether this fact is also responsible for the lack of photocatalytic activity of chromium-doped titanium dioxide as Cr^{3+} has been suggested to be responsible for visible light absorption in chromium-doped TiO_2 [60].

4.2 TiO_2(110) codoped with chromium and antimony

In this section, I report on the surface structure of TiO_2(110) codoped with antimony and chromium. The concentration of the two metals are intended to be equal and the concentration is expected to be about 2 to 3 atom percent, each. This order of magnitude was confirmed by an X-ray photoelectron spectroscopy (XPS) measurement of the freshly calcined wafer[3]. The dopant ratio was estimated from the XPS data to be about [Cr] / [Sb] = 3/5. Thus, the total dopant concentration [Cr] + [Sb] can be estimated to be in the range of 3 to 8 atom percent.

Fig. 4.6 shows a series of NC-AFM images of decreasing frame size as typically obtained on the codoped surface after preparation in UHV. At large frame size (Fig. 4.6(a) and (b)), steplike structures with a typical height of 1 nm up to 10 nm are observed. The regions in between these steps are rather furrowed areas with a lot of troughs as can be seen in Fig. 4.6(c). The depth of the troughs is typically three to six times as large as a single monatomic step height on TiO_2(110). Extended, atomically flat terraces were never observed. Fig. 4.6(d) reveals that the surface consists of numerous atomically flat facets. Each facet covers an area of typically 40 nm^2. Thus, a typical facet consists of only a few hundred unit cells. This is in contrast to the evenly stepped surface usually observed on similar prepared TiO_2(110), where terraces exhibit monatomic step height and terrace areas are larger by at least a factor of thousand.

To exclude that the surface roughness is only a result of inadequate preparation parameters, I systematically varied the annealing temperature from 500 K to 1100 K and annealing duration from 15 min up to 16 h (see Tab. 4.1). Fig. 4.7 shows three representative sets of images corresponding to three selected annealing recipes. The observed surface roughness and faceting is found to be virtually independent of the annealing parameters. Neither high temperature nor drastically increased annealing duration led to extended, atomically flat terraces. Thus, this special morphology seems to be intrinsically tied to the codoped titania surface.

---

[3] The XPS measurement was carried out by order of H. Onishi at Ion Engineering Research Institute, Osaka, Japan (2008).

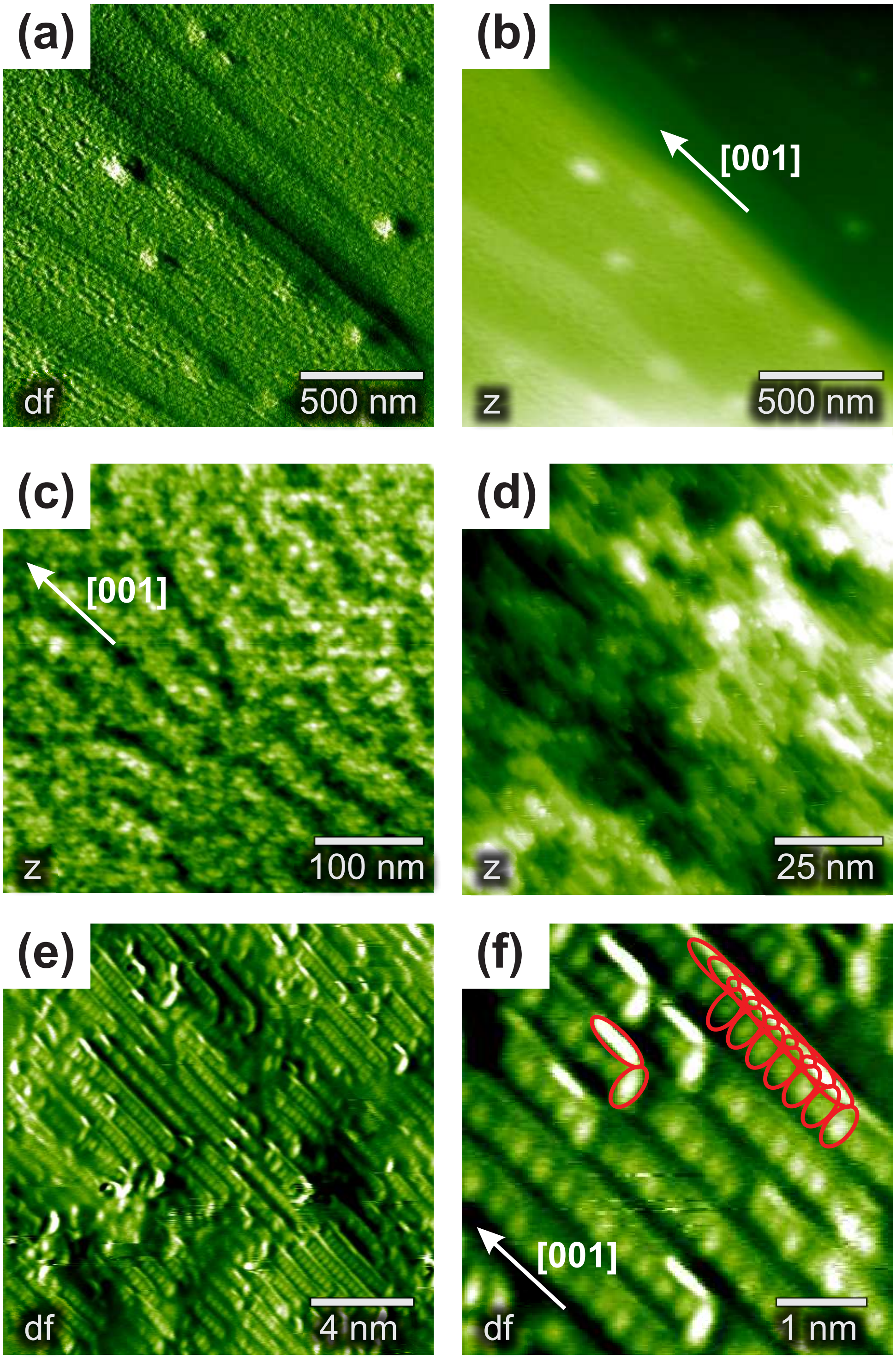

Figure 4.6: *NC-AFM topography (z) and detuning (df) images of a* $TiO_2(110)$ *sample doped with chromium and antimony. (a) and (b) show an overview revealing high steps aligned in [001] direction. The regions in between are rough areas with many troughs (c). In (d) small, atomically flat facets become distinguishable. True atomic resolution can be obtained on each facet, revealing bright atomic rows and protruding defects (e). In this particular case, an L-shaped tip results in additional bright lines next to each atomic row as indicated in (f) by red ellipses.*

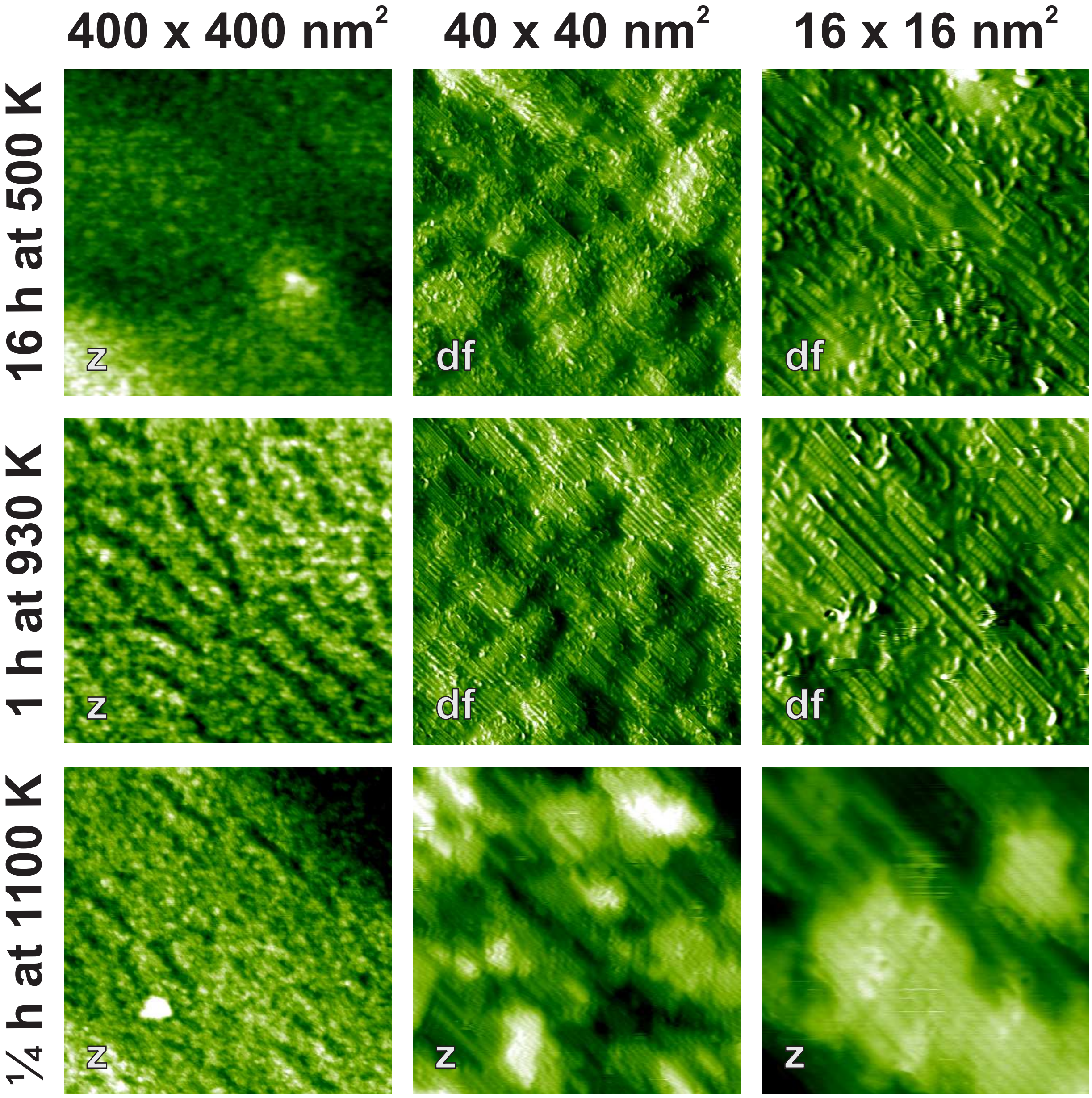

Figure 4.7: *NC-AFM topography (z) and detuning (df) images of a codoped* $TiO_2(110)$ *sample representing three annealing recipes. Images of equal size reveal qualitatively similar appearance. Hence, changing annealing temperature and duration does not change the observed surface roughness and faceting.*

Surface reconstruction

At the atomic scale (Fig. 4.6(e) and (f)), rows of bright atoms divided by thin, bright lines become visible. These thin, bright lines can be explained by a peculiar tip shape that images all surface species in a characteristic L-shape as indicated in Fig. 4.6(f). True atomic resolution has been obtained on nearly all facets simultaneously, although typically several monatomic steps exist in a single image.

Single defects appear as protrusions on the atomic rows. Thus, the bright atoms are attributed to bridging oxygen atoms. Furthermore, I conclude that the observed protrusions most likely can be attributed to hydroxyl species as usually observed on the pristine surface [1, 8–10]. The density of protrusions was estimated to be (0.5 ± 0.3) % ML. From a previous defect density study on pristine titania presented in Fig. 3.2 the density of hydroxyls can be expected to be (0.9 ± 0.6) % ML [40] on a similarily treated pristine sample, which is in good agreement with the findings on the surface of codoped titania presented here. Hence, dopant-induced bulk reduction as reported for chromium-doped $TiO_2(110)$ is not observed on the codoped surface.

At a first glance, the atomic structure of the doped surface resembles the structure of pristine $TiO_2(110)$. Fig. 4.8 shows subsequently recorded detuning images with true atomic resolution on several facets. The images were carefully corrected for linear lateral drift using identical drift velocity values for all images as described in Sec. 2.3. The drift velocity values

$$\dot{x} = (3.87 \pm 0.05)\,\tfrac{\mathrm{pm}}{\mathrm{s}}$$
$$\dot{y} = (1.56 \pm 0.05)\,\tfrac{\mathrm{pm}}{\mathrm{s}}$$

were obtained from a series of nine consecutively recorded images in total.

Determining the surface unit cell in the images in Fig. 4.8(a - d), it is found that the surface unit cell is not rectangular as for pristine $TiO_2(110)$ but shows a surface reconstruction, indicating a firm integration of the dopant atoms into the titanium dioxide crystal structure. The surface unit cell is sheared by an angle of 7° ± 1° with respect to the surface unit cell of rutile. This shearing results in an appearance that closely resembles a (1×4) reconstruction as indicated in Fig. 4.8(e). The findings are identical for up and down scanned images. Thus, scan artifacts or inadequate drift correction can be excluded to be the origin of the observed shearing. As mentioned, this surface reconstruction is a strong evidence for the integration of the dopant atoms into the titania crystal although the three species cannot be directly distinguished from the NC-AFM images.

The observed small size of facets on the codoped titania surface compared to the large terraces observed on pristine titania may result from stress between the reconstructed surface layer and underlying layers. Thus, the roughness of the surface might be intrinsically tied to the codoping and can, therefore, not be overcome by any preparation recipe.

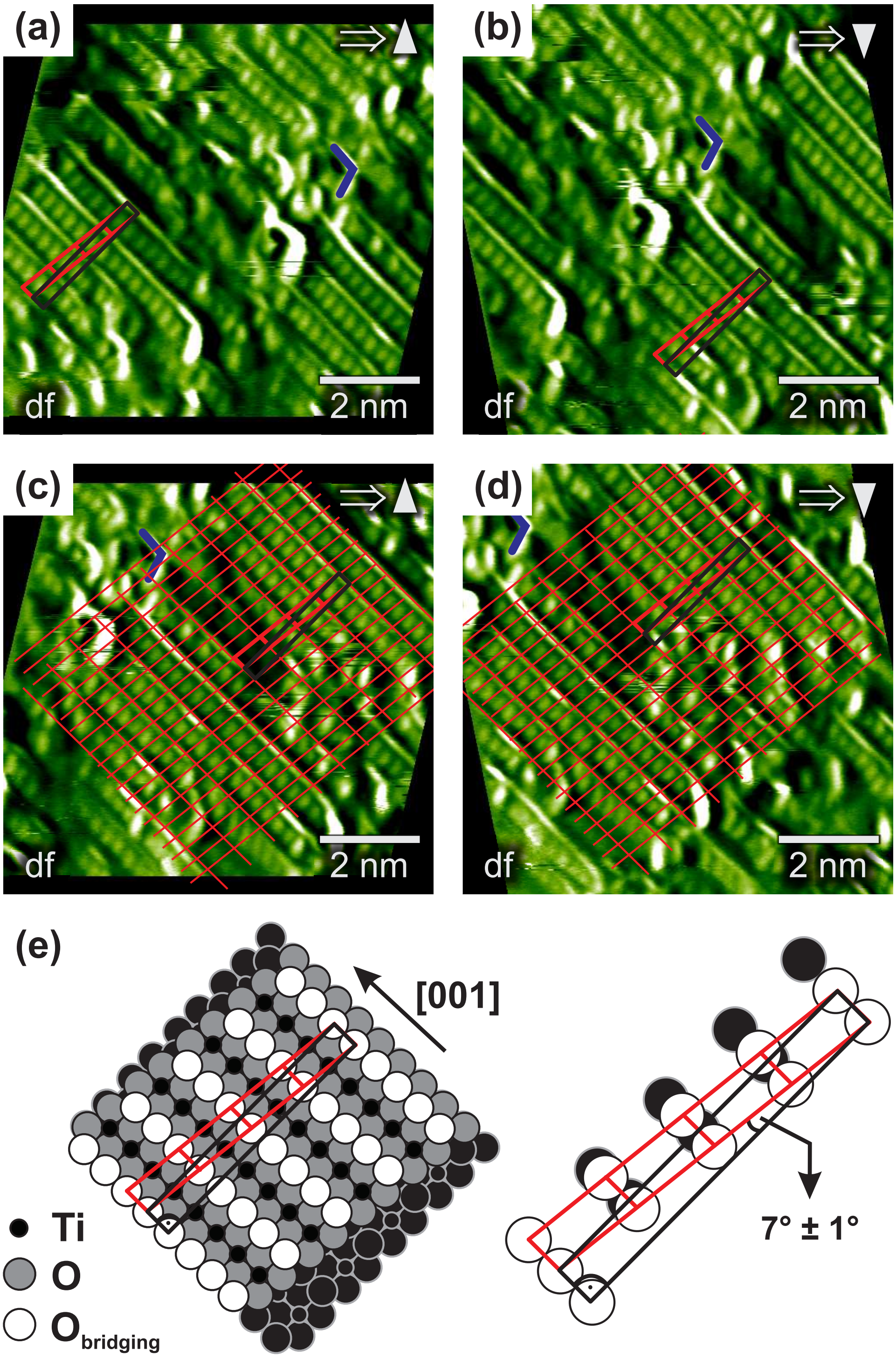

Figure 4.8: *Subsequently recorded NC-AFM detuning images obtained on codoped* $TiO_2(110)$ *(a - d), corrected for linear lateral drift as described in Sec. 2.3 using identical drift velocity values for all images. A stationary feature is marked by a blue check. The observed surface unit cell (indicated by red grid) is sheared by 7° ± 1° with respect to the surface unit cell of rutile* $TiO_2(110)$ *(indicated by black rectangle). In (e) the reconstructed surface is sketched corresponding to the findings in the experiment. The nonrectangular unit cell closely resembles a (1 × 4) reconstruction. The black rectangle indicates four unit cells of pristine* $TiO_2(110)$*.*

Facet orientation

Besides the surface unit cell reconstruction, another peculiarity of the codoped titania surface was detected: A careful analysis of the topography images revealed the existence of at least two types of facets on the surface. The majority is oriented with their surface normal vectors in [110] direction. However, few facets are observed, which are oriented in vicinal directions.

The topography images, corrected for linear vertical drift as described in Sec. 2.3, do not contain information on the atomic scale due to slow distance feedback loop settings. However, the orientation of the facets can be identified from these images. To eventually combine the information of facet orientation (topography image) and atomic resolution (detuning image), I multiplied both images pixelwise. The results are shown in Fig. 4.9 and Fig. 4.10. The first image (Fig. 4.9) shows three facets of different height, each separated by a monatomic step height. All three facets are parallel to the image plane as indicated by the respective color. Thus, they are exclusively oriented in [110] direction.

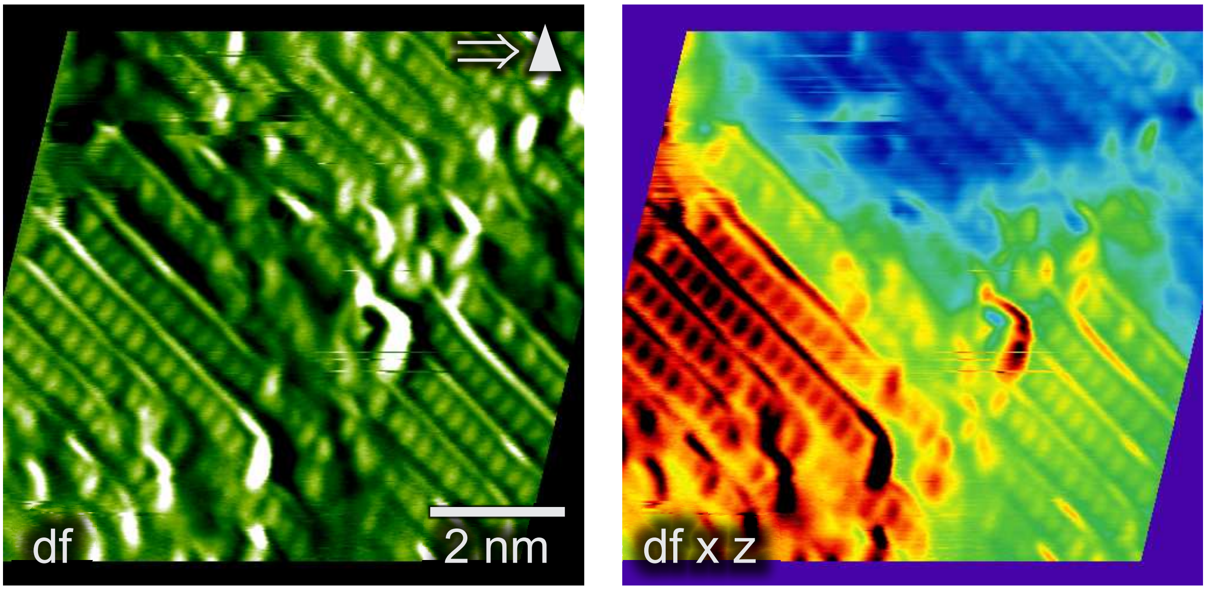

Figure 4.9: *NC-AFM image obtained on codoped $TiO_2(110)$ showing three facets that are separated by monatomic steps. Besides the detuning (df) also the product of topography and detuning ($df \times z$) is shown. The topography image was corrected for linear vertical drift. Additionally, all images were carefully corrected for linear lateral drift. The values of the drift velocity were obtained from a series of nine consecutively recorded images in total. The hybrid image clearly indicates that all facets are oriented with their surface normal vector in [110] direction.*

In contrast, the facets in the image shown in Fig. 4.10 are oriented in different directions. The presented height profiles indicate a facet oriented in [110] direction as well as a vicinal oriented facet. The surface normal vectors of the indicated facets enclose an angle of about 4°. The tilt of the vicinal facet resembles a [670] orientation of the surface normal vector.

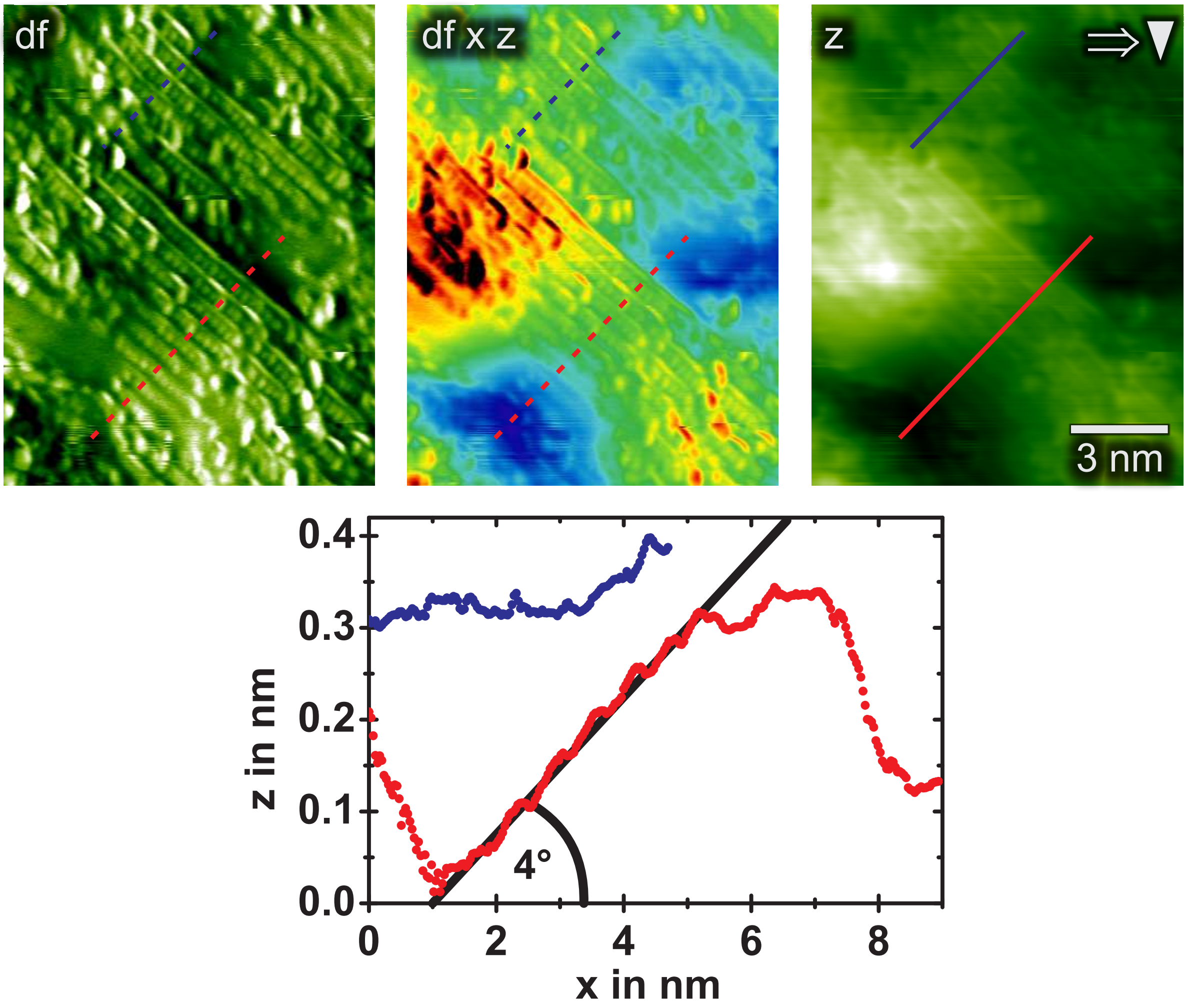

Figure 4.10: *NC-AFM image obtained on codoped* $TiO_2(110)$ *showing the detuning (df) the topography (z) and additionally the product of topography and detuning* ($df \times z$)*. The topography was corrected for linear vertical drift in analogy to Fig. 4.9. The hybrid image clearly indicates that at least one facet exists that is not oriented in [110] direction. The depicted height profiles perpendicular to the [001] direction (solid lines, dashed lines are for orientation only) indicate a [110] oriented facet (blue line) and a vicinal oriented facet (red line). The surface normal vector is tilted by about 4° with respect to [110], which resembles a [670] orientation.*

Reconstruction model

In the following, I will present a model, which allows to understand the observed surface unit cell reconstruction.

In doped titania, chromium and antimony are expected to exist predominantly in the oxidation states Cr^{3+} and Sb^{5+}, respectively [60]. They substitute Ti^{4+} in the lattice. As long as the dopant ratio is close to unity, charging of the crystal does not take place. The ionic radii of the three cations are given in Tab. 4.3. The values are nearly identical, pointing to a very similar ionic bond length between the three metal species and oxygen. In a purely ionic picture, codoping of rutile titania with an equal amount of antimony and chromium would, therefore, not induce stress into the bulk. Hence, no reconstruction would be expected from this point of view.

However, titania is not a purely ionic crystal and the interaction is not purely electrostatic as indicated by the formal charge of about -1 for oxygen and approximately $+2$ for titanium [36]. The covalence of the metal-oxygen bond rather strongly depends on the metal species as can be seen from the electronegativity values also given in Tab. 4.3. The electronegativity difference between oxygen (3.44) and the dopant species is much smaller especially in the case of antimony than between titanium and oxygen. This clearly indicates a more covalent interaction between the dopants and oxygen than in the pristine sample. Consequently, the covalent radii (Tab. 4.3) of chromium and antimony should be considered, which differ significantly from that of titanium.

element	electronegativity	covalent radius	oxydation state	ionic radius
Ti	1.54	160 pm	Ti^{4+}	60.5 pm
Cr	1.66	139 pm	Cr^{3+}	61.5 pm
Sb	2.05	139 pm	Sb^{5+}	60.0 pm

Table 4.3: *Electronegativity [64] (Pauling scale) and covalent radii [65] of titanium and the two dopants as well as the most probable oxidation state and the ionic radii of these metal ions [63]. The electronegativity of oxygen is 3.44.*

Exactly this discrepancy in covalence may explain the experimentally observed surface reconstruction. The correlation between doping and surface reconstruction will be discussed in the following model.

The surface unit cell of pristine $TiO_2(110)$ contains one titanium atom with a covalent radius of 160 pm (see Tab. 4.3) and two oxygen atoms with covalent radii of 66 pm [65]. The resulting covalent bond length for Ti-O is 226 pm. This simple model does not take into account that titanium is fivefold or sixfold coordinated on the titania surface. Thus, the exact bond lengths of 195 pm and 198 pm [1] are not precisely reproduced by a simple addition of the covalent radii. However, the following argumentation is independent of this discrepancy. The Ti-O bond lentgh is a measure for the space a Ti-O unit requires. Thus, this value is proportional to the square root of the surface unit cell area A_0 of rutile $TiO_2(110)$

$$\sqrt{A_0} \propto 160\,\text{pm} + 66\,\text{pm} = 226\,\text{pm}.$$

In the doped sample, antimony and chromium atoms of smaller covalent radius of only 139 pm (see Tab. 4.3) substitute some of the titanium atoms. Due to their smaller covalent radii Sb-O and Cr-O units require less space than Ti-O units. Consequently, the average covalent bond length is reduced in doped titania according to

$$(1 - [\text{Cr}] - [\text{Sb}]) \cdot 160\,\text{pm} + ([\text{Cr}] + [\text{Sb}]) \cdot 139\,\text{pm} + 66\,\text{pm} = 226\,\text{pm} - ([\text{Cr}] + [\text{Sb}]) \cdot 21\,\text{pm}$$

where [Cr] and [Sb] are the atom concentrations of chromium and antimony, respectively. Eventually, the area of the surface unit cell is expected to be smaller than that of the pristine surface. Shearing of the unit cell reduces the area of the unit cell by the cosine of the shearing angle. In analogy to the case of pristine titania, I assume the square root of the surface unit cell area A of the codoped surface to be proportional to the average covalent bond length. With the values from Tab. 4.3, I obtain for the square root of A

$$\sqrt{A} = \sqrt{A_0 \cdot \cos\alpha} \propto 226\,\mathrm{pm} - ([\mathrm{Cr}] + [\mathrm{Sb}]) \cdot 21\,\mathrm{pm}$$

where α is the shearing angle. Substituting A_0 by the above formula,

$$\cos\alpha = \left(1 - \frac{21}{226} \cdot ([\mathrm{Cr}] + [\mathrm{Sb}])\right)^2$$

is derived for the cosine of the shearing angle in dependence on the dopant concentrations. This graph is plotted in Fig. 4.11.

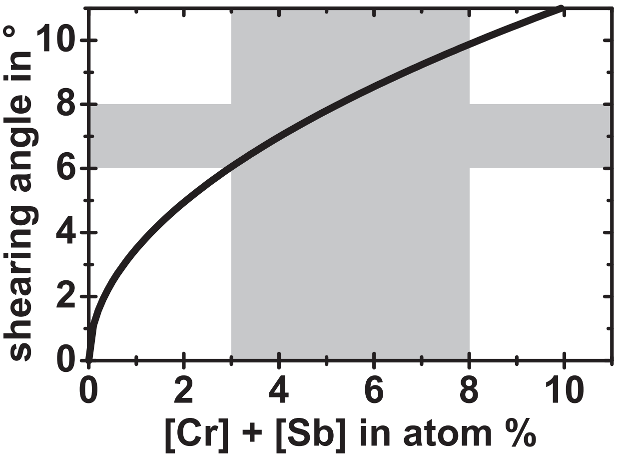

Figure 4.11: *Shearing angle of surface unit cell of doped TiO_2(110) in dependence of the total dopant concentration [Cr]+[Sb]. The calculation (solid line) only takes into account the dopant-induced reduced covalent bond length. The range of expected total dopant concentration (3 to 8 atom percent) as well as the experimentally observed shearing angle (7° ± 1°) are indicated by grey boxes.*

This simple model predicts a shearing angle of about 8° ± 2° to balance a dopant concentration of 3 to 8 atom percent in total (i.e. [Cr] + [Sb]) as present in the experiment. Within the error, this is exactly the shearing angle observed in the NC-AFM images.

The strikingly good agreement between the experimental observations and the angle derived from this simple model supports the assumption of a firm integration of the dopant atoms into the titanium dioxide crystal structure. Based on this simple picture, the observed reconstruction can be understood as a strategy to compensate for the significantly smaller covalent radii of the dopant atoms.

Note, however, that although the shearing angle of about 7° can be measured quite accurately, the resulting relative length deviation of as small as $(1 - \cos 7°) = 0.007$ is far beyond the accuracy of the lateral dimension measurement. The length deviation is definitely smaller than the error of the lateral correction factor C_{lateral} as introduced by Eq. 2.18. Thus, it is not possible from the images to decide whether the surface unit cell is compressed by the reconstruction or not. To give a possible explanation for the reconstruction, I assumed that the unit cell area becomes smaller by shearing, however, due to the very small length deviation, I cannot provide clear-cut experimental evidence for this assumption. Nevertheless, the shearing angle and therefore the reconstruction are experimental facts without any doubt, strongly supporting the presented model.

Summary

In conclusion, I have investigated the (110) surface of rutile TiO_2 codoped with 3 to 8 atom percent of chromium and antimony in total. The NC-AFM images revealed a very rough surface consisting of numerous atomically flat facets of very small size. Although the majority of facets is oriented in [110] direction, several facets are found revealing a tilted surface normal vector. True atomic resolution was obtained on nearly all facets. The defect density was found to be identical to what we observed on an equally treated pristine surface. Additional charge transfer resulting in vacancy creation as observed in chromium-doped TiO_2(110) was not observed, as chromium and antimony with formal oxidation states of 3+ and 5+, respectively, exist in equal amounts in the investigated sample.

The surface unit cell of the codoped sample was observed to be sheared by an angle of $7^\circ \pm 1^\circ$ with respect to the unit cell of rutile titania, closely resembling a (1×4) reconstruction. This reconstruction indicates a firm integration of antimony and chromium atoms into the lattice structure.

The shearing is explained by comparing the covalent radii of the dopant atoms with that of titanium. The observed reconstruction can be understood as a strategy to compensate for the significantly smaller covalent radii of the dopant atoms.

Stress between the surface layer and underlying layers that might be expected from this reconstruction may explain why no extended terraces were observed. Thus, small facets and therefore an extremely high step edge density seem to be intrinsically tied to TiO_2(110) codoped with equal amounts of antimony and chromium.

Step edge sites are known to be excellent adsorption sites in particular for educts of a potential photocatalytic reaction. Hence, the faceting of codoped titania might be of importance when discussing the photocatalytic activity of transition metal doped TiO_2(110).

4.3 Antimony-doped $TiO_2(110)$

For comparison, also an antimony-doped $TiO_2(110)$ sample was investigated, although this system is not directly relevant for photocatalytic applications. However, the implications of antimony excess on the photocatalytic activity of codoped TiO_2 have attracted considerable attention [60, 61]. In titania, antimony most likely exists in the oxidation states Sb^{3+} and Sb^{5+} [60]. Thus, an equal amount of both cations can be expected to substitute for Ti^{4+} in the antimony-doped titania sample to maintain charge neutrality. The need for antimony trivalent cations with a comparatively large ionic radius of 76.0 pm compared to that of Ti^{4+} (60.5 pm) and Sb^{5+} (60.0 pm) [63] has been suggested to result in a deformed TiO_2 lattice, which in turn results in the creation of recombination centers for photoinduced electrons and holes [60].

Here, the investigation of a $TiO_2(110)$ sample doped with an antimony concentration of 2 to 3 atom percent is presented. The surface structure of antimony-doped titania at the atomic scale is shown in Fig. 4.12. The surface is found to be covered by a dense layer of 5 to 6 % of a monolayer of protruding adsorbates (1 ML corresponds to one adsorbate per unit cell). The adsorbates appear to have a much larger diameter than the typical defect species. The apparent height of the adsorbates was measured to be in the order of 100 pm. It is very unlikely that these adsorbates represent the typical hydroxyl or vacancy species as such a high density would correspond to a heavily reduced sample, which is tied to a dark blue color of the entire crystal. In contrast, the crystal is found to be transparent after calcination and only slightly bluish after UHV treatment as shown in Fig. 4.1(b).

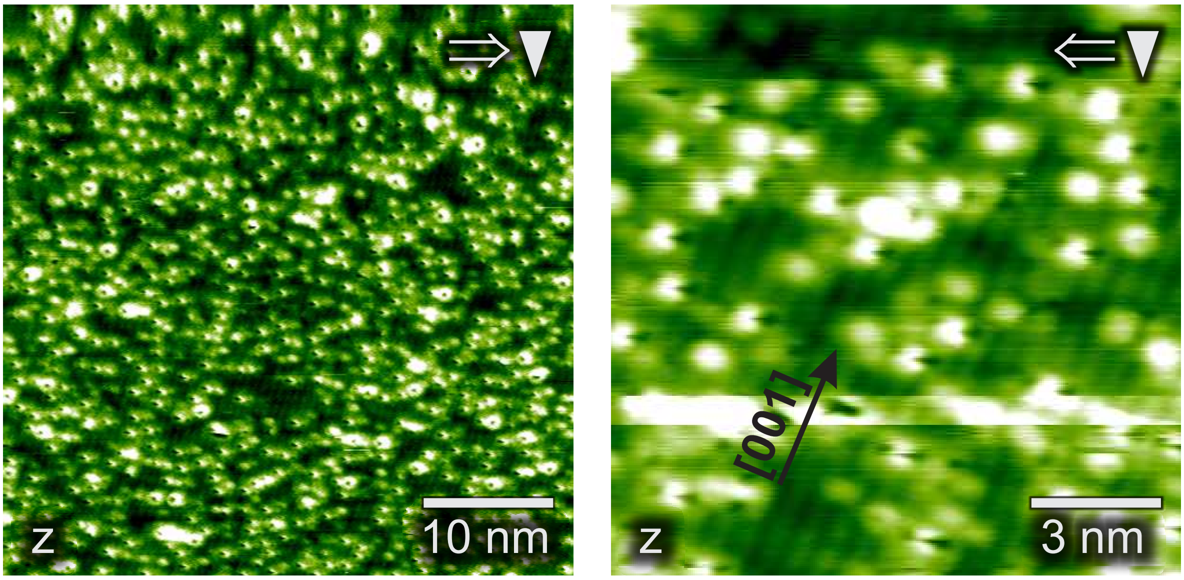

Figure 4.12: *NC-AFM topography images obtained on antimony-doped $TiO_2(110)$ after annealing at 1100 K. The surface is found to be covered by a dense layer of protruding adsorbates. The dark spot in the center of each adsorbate is a scan artifact, which can be explained by slow distance feedback loop settings as described in [25]. Besides the adsorbates, a row pattern resembling the $TiO_2(110)$ surface can be identified in both images. The periodicity perpendicular to [001] was measured to be (660 ± 30) pm.*

Besides the adsorbates, the typical row pattern of the $TiO_2(110)$ surface is also visible in the images in Fig. 4.12. The periodicity perpendicular to the [001] direction was measured to be (660 ± 30) pm, which is within the error identical to the surface unit cell length of the pristine titania surface.

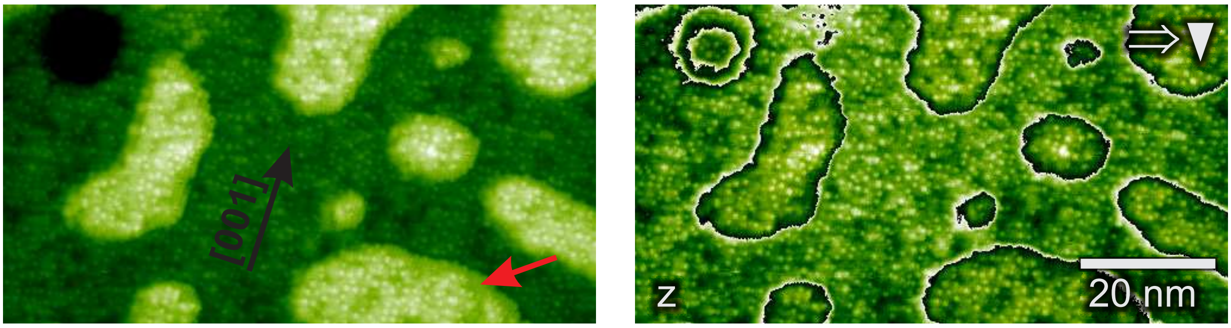

Figure 4.13: *NC-AFM topography image obtained on antimony-doped* TiO_2*(110) annealed at 930 K. The identical image is presented in normal color scale (left) and in repeated color scale (right). The adsorbates cover all terraces. However, the regions on the islands near the step edges are found to be free from adsorbates as indicated by the red arrow. There, the typical row pattern known from the pristine surface is visible.*

Fig. 4.13 reveals that the adsorbates cover all terraces and islands of the surface. Interestingly, the adsorbates seem not to adsorb in close proximity to the step edges. In a thin stripe at the edges of the islands (indicated by red arrow), the line pattern of the surface is visible. From a Fourier transformation of this image (not shown), the lines are measured to be separated by (670±30) pm similar to what was obtained from Fig. 4.12.
The findings at the atomic scale are independent of the applied annealing recipes. Especially, the density of adsorbates was found to be virtually identical after each preparation cycle (see Tab. 4.1).

Holes

A typical image of large frame size obtained on the antimony-doped titania surface is presented in Fig. 4.14. The terraces are found to be formed similar to what is typically observed on pristine TiO_2(110) (compare Fig. 3.3). The uncalibrated, monatomic step height was measured to be (360 ± 20) pm, which is identical to what is found on pristine titania. Furthermore, there are two deep holes visible in Fig. 4.14(a) with a diameter of about 50 nm. The depth of these holes cannot be obtained from NC-AFM measurements as explained in the following. The line profiles presented in Fig. 4.14 show a horizontal scan line in forward direction of the topography (c), the detuning (d) and the amplitude (e) image. At the beginning of the hole the detuning drops to zero, indicating a too large tip-sample distance. The topography signal shows that the scanner approaches the sample at the hole site by more than 10 nm, but the detuning remains zero. Apparently, the ground of the hole was not reached by the tip. At the end of the hole, the tip strongly interacts with the backside of the hole, which is indicated by large negative and even positive detuning values. This coincides with a decrease in amplitude of about 10 %, indicating highly dissipative interaction. This behaviour was observed at all hole sites, even with fastest distance feedback loop settings available. From various attempts to scan such holes at small frame size (not shown), the typical depth can be assumed to be definitely larger than 30 nm. Assuming an aspect ratio of the tip of typically two at highest, which corresponds to a cone angle of the tip apex of at least 90°, the depth of a 50 nm wide hole is - as a matter of principle - not accessible if the depth is larger than 25 nm.

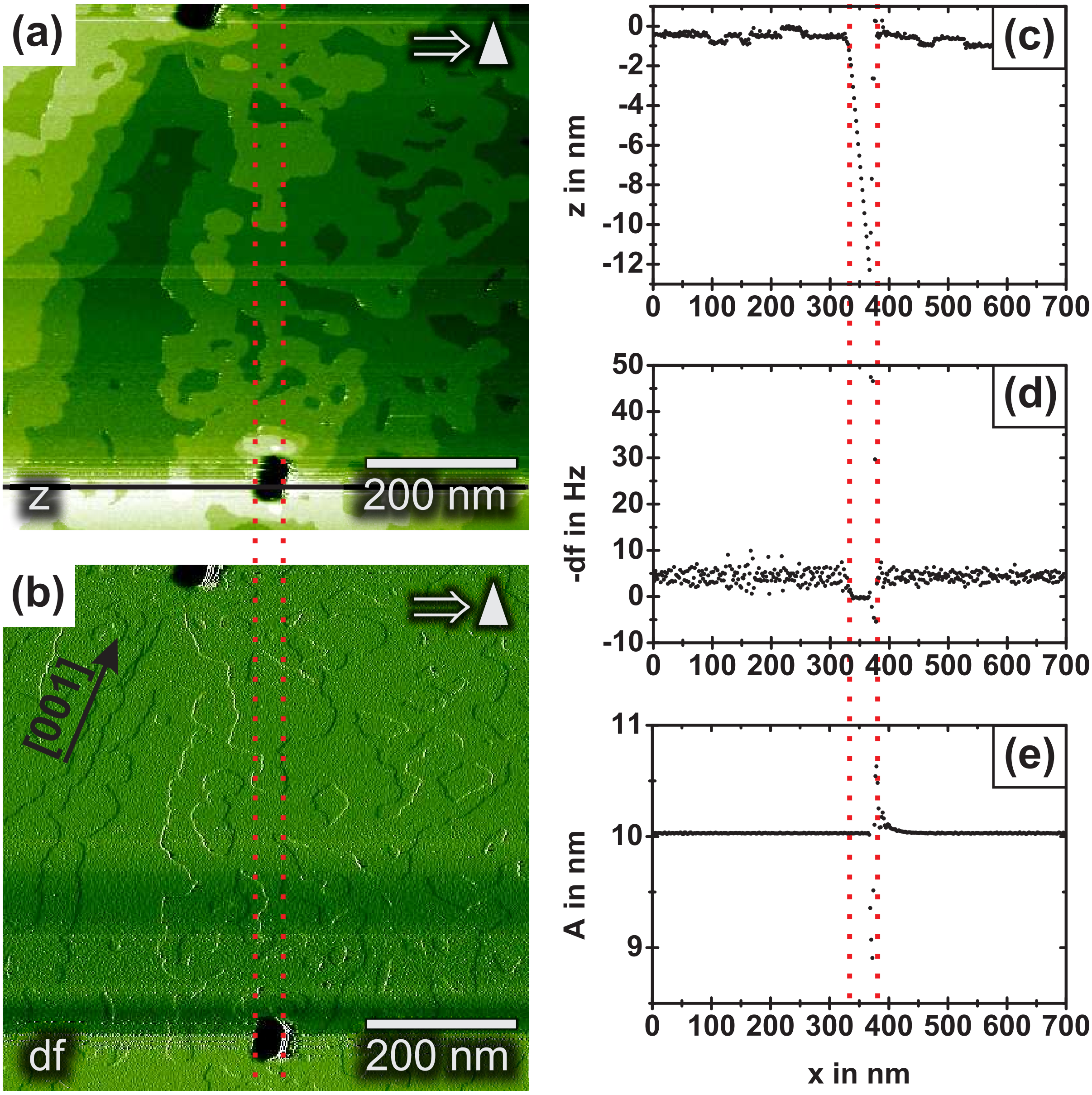

Figure 4.14: *NC-AFM topography (a) and detuning (b) image obtained on antimony-doped* TiO_2*(110). Two holes can be identified with a diameter of about 50 nm. Line profiles depict a horizontal scan line in forward direction of the topography (c), the detuning (d) and the amplitude (e) signal at a hole site (indicated by black line). The line profiles indicate that the hole must be deeper than 12 nm as the detuning remains zero within the hole while the scanner approaches the surface. At the backside of the hole, the tip strongly interacts with the sample as the scanner cannot retract the tip fast enough. This is indicated by even positive detuning values and a decrease in amplitude.*

The holes are found to be rather homogeneously distributed at the surface as indicated by Fig. 4.15. The mean distance between neighboring holes was measured to be about 1 µm. Interestingly, all holes are found to be surrounded by small islands as depicted by the detail images in Fig. 4.15, resembling volcano-like crater.

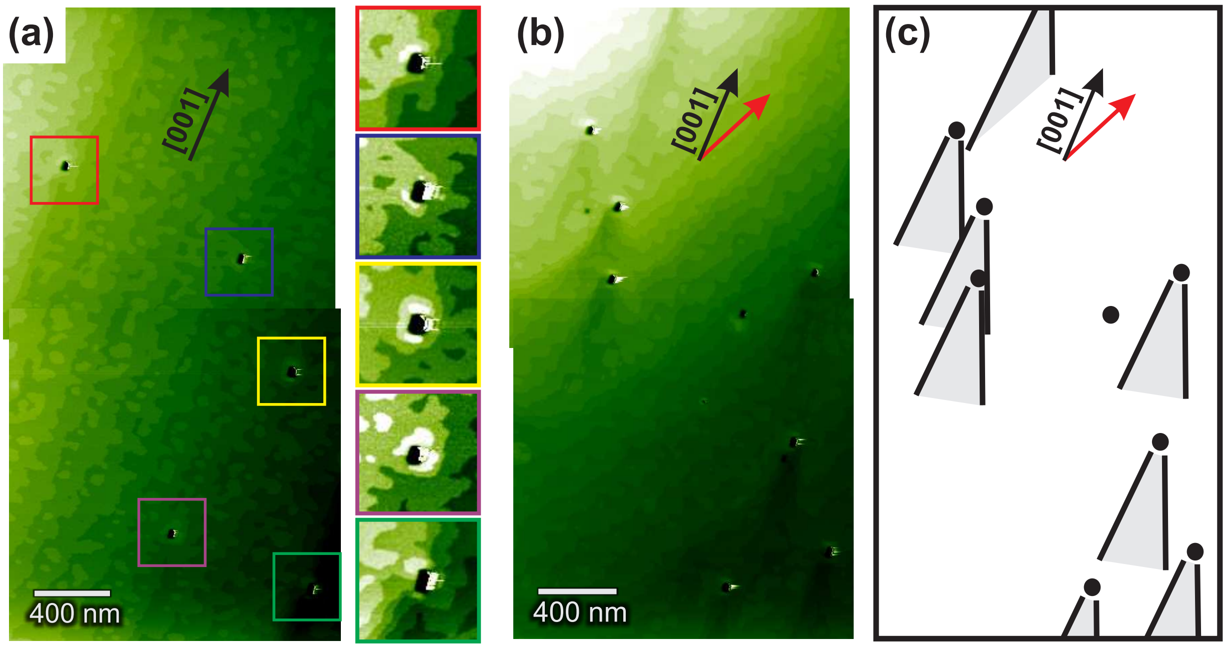

Figure 4.15: *NC-AFM topographic images of antimony-doped $TiO_2(110)$ obtained after annealing at 1100 K. In total, 13 holes are visible with a mean distance of about 1 µm. The cut-outs extracted from (a) reveal that all holes are surrounded by small islands. This results in an appearance that resembles a volcano-like shape. The step edges can be found to run either parallel to the [001] direction (a) or enclose an angle with the [001] direction (b) as indicated by the red and black arrows. Cone-shaped troughs located at the hole sites and aligned in [001] direction are, therefore, only observed in case of step edges that are not parallel to [001]. The holes (black circles) and cone-shaped troughs (grey triangles) identified in (b) are sketched in (c) for illustration.*

All holes in Fig. 4.15(b) appear at the sharp end of a cone-shaped trough located at each hole. For illustration, these troughs are sketched in Fig. 4.15(c). The holes in Fig. 4.15(a) have no troughs. This difference can be explained by differently oriented step edges in the two images as explained in the following. In Fig. 4.15 two typical images are presented, either showing step edges running parallel to the [001] direction (a) or step edges that enclose an angle with the [001] direction (b), as indicated by the red and black arrows. The cone-shaped troughs are also aligned in [001] direction. Assuming that the terraces are growing in [001] direction during annealing, the observed troughs might be explained by shadowing at hole sites.

Influence of annealing temperature

The images presented in Fig. 4.15 were obtained after annealing at 1100 K for 15 min. For comparison similar images obtained after annealing at 930 K for 1 h are shown in Fig. 4.16. The terraces appear perforated and covered by small islands as already observed on pristine $TiO_2(110)$ annealed at the same temperature (Fig. 3.3). In contrast to the high-temperature prepared, doped surface, here, a large number of small pits exist besides the large, deep holes. These small pits have a typical depth of 1 to 2 nm and an average nearest-neighbor distance of about 50 nm.

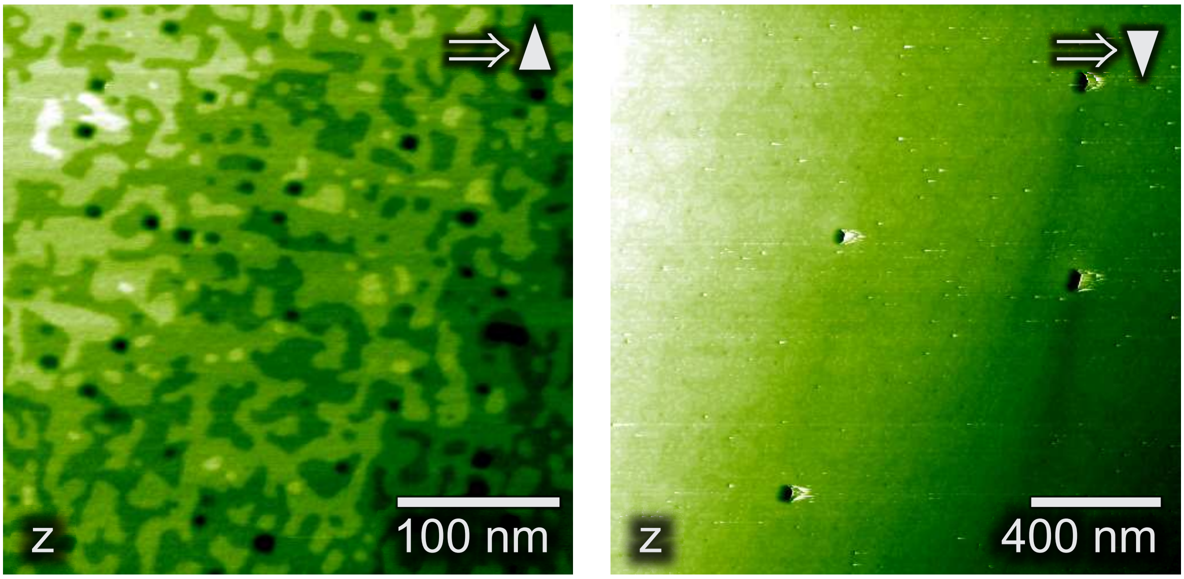

Figure 4.16: *NC-AFM topographic images of antimony-doped $TiO_2(110)$ obtained after annealing at 930 K. The terraces are perforated and numerous small islands exist, similar to the pristine surface when annealed at the same temperature. Besides few large and deep holes, which appear identical as observed after annealing at 1100 K, a large number of small pits is present here. These pits are typically less than 2 nm deep and less than 10 nm wide.*

Besides the two already discussed types of holes, another type of hole was observed seldom after annealing at 1100 K. The holes of this type are typically less than 10 nm deep, but extend over several hundred nanometer. Two of this kind are shown in Fig. 4.17. A detailed analysis of the flat holes revealed that the typical surface structure with step edges of monatomic height can be found at the bottom of the holes as indicated by Fig. 4.18. Besides these flat, extended holes also deep holes with their cone-shaped trough as introduced in Fig. 4.15(b) and (c) exist in the surrounding surface region.

The images presented in Fig. 4.15(b) and Fig. 4.17 are obtained after the very same preparation cycle at macroscopical different surface areas. However, size and number of holes are different. Taking the form and flattness of terraces as reference for the annealing temperature and assuming large, island-free terraces to result from higher temperature preparation as discussed in Fig. 3.3, the situation found in Fig. 4.17 might be explained by an annealing temperature slightly lower than 1100 K. Due to different thermal contact to the silicon stripe used for resistive heating of the sample, slightly different annealing temperatures at macroscopically different sample sites are conceivable.

Obviously, the number as well as the size of the holes and pits crucially depend on the exact annealing procedure. Thus, it might be possible to control the size and density of the pits by properly tuned annealing parameters. This could be of interest for creating nanopatterned surfaces.

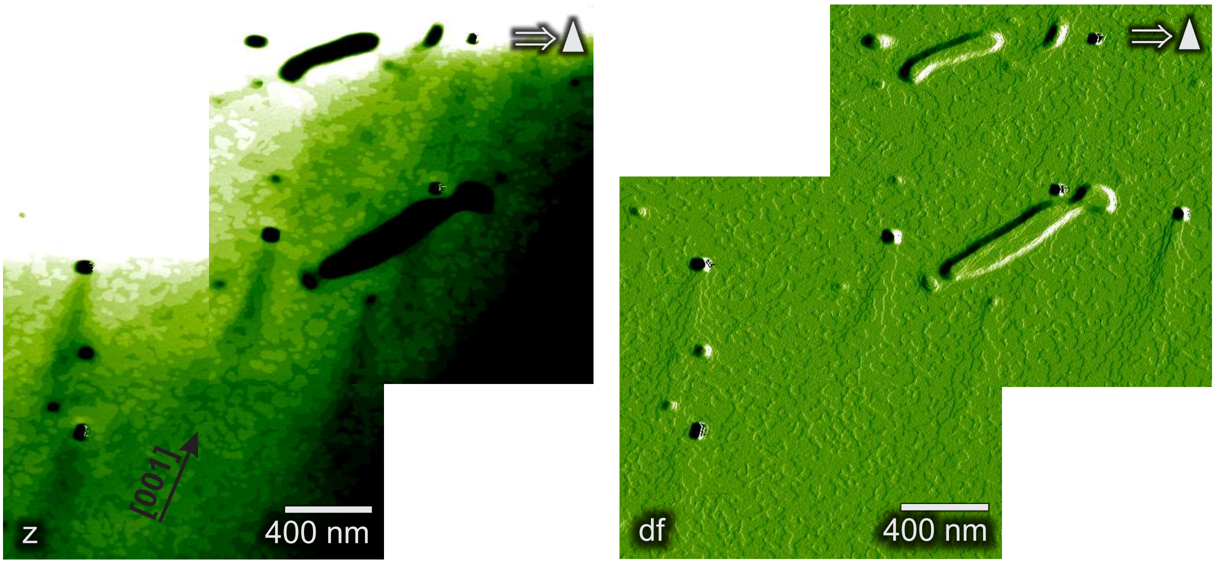

Figure 4.17: *NC-AFM topography and detuning images of antimony-doped* $TiO_2(110)$*. The images represent seldom observed flat holes that extend over several hundred nanometer. Besides, also deep holes with their cone-shaped trough as introduced in Fig. 4.15 can be observed in the surrounding area.*

Summary

In conclusion, I have studied the surface structure of antimony-doped $\text{TiO}_2(110)$. The surface was found to exhibit terraces, steps and a row pattern as observed on pristine titania. The terraces are covered by a dense layer of adsorbates. As the typical defects, namely hydroxyls and oxygen vacancies, can be excluded as explanation for the adsorbates, their nature has to be explained by antimony-rich clusters.

Holes with a depth ranging from a few up to more than hundred monatomic steps are observed. Width and depth of the holes were found to crucially depend on the annealing procedure. The deepest holes are surrounded by small islands resembling a volcano-like shape.

All findings draw a picture of weakly integrated antimony in antimony-doped titania. In the following, I will outline a possible scenario for explaining the observed structural characteristics. Antimony induces large lattice stress in the titania crystal as already suggested by the too large ionic radius of Sb^{3+}. Upon vacuum annealing, antimony can seggregate to the surface, forming seggregation channels that appear as nanosized volcanos. At low annealing temperature, only antimony from the upper layers might have enough thermal energy to reach the surface. Thus, a large number of small, flat pits is created.

At higher annealing temperature the mobility of antimony dopants is increased. Hence, also material from deeper layers can seggregate to the surface. Furthermore, more material seggregates on a shorter time scale. The large and the deep holes, created upon high-temperature annealing indicate that the sample surface is almost exploding as soon as antimony gets enough thermal energy to leave the bulk. Then, instead of numerous small pits, only few large seggregation channels establish, to reduce the surface energy. These holes are rather homogeneously distributed. Cone-shaped troughs are observed to

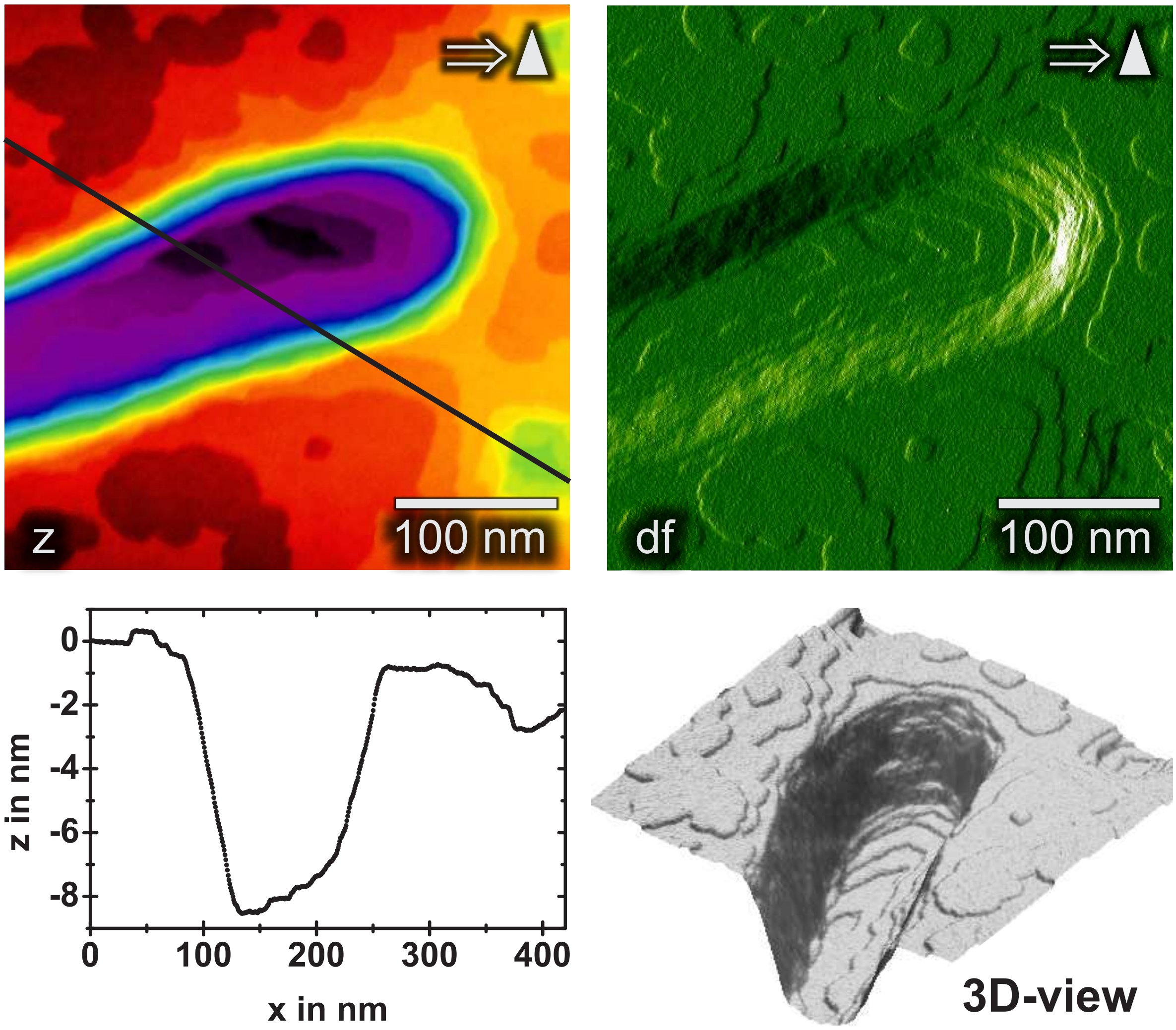

Figure 4.18: *NC-AFM topography and detuning image of antimony-doped* TiO_2*(110) presenting a detail of the flat extended hole introduced by Fig. 4.17. The images as well as the three-dimensional plot of the topography image reveal that the surface at the bottom of the extended holes appears normal. From the height profile (position indicated by black line) the depth of this particular hole is measured to be about 8 nm.*

exist close to hole sites, which might result from shadowing at these holes. A possible explanation is that terraces growing during annealing are distorted at the holes.
Erupted material consisting of TiO_2 forms new islands around the holes resulting in the volcano-like appearance. Antimony erupted through the holes adsorbes as clusters on top of the surface.
Although an excess of antimony is unfavorable for photocatalytic applications, the presented study revealed another interesting phenomenon: It seems to be possible to create nanosized holes in a controlled way by tuning the annealing parameters of antimony doped TiO_2(110). This might be an appropriate strategy for creating nano-patterned surfaces with macroscopic techniques.

5 Conclusion

In the present thesis, I report on an NC-AFM study of the (110) surface of rutile titanium dioxide. Both, pristine as well as transition-metal-doped samples were investigated at the atomic scale.

In the first part of the thesis, prior to the surface studies, essential improvements of the commercial VT AFM 25 were described. Parts of the detection system as well as electronic components were analyzed with respect to their contribution to the total noise level. I optimized the setup of the microscope, resulting in an increase of the signal-to-noise ratio by almost one order of magnitude. Additionally, the minimum detectable force gradient was massively reduced, while the maximum detectable force was increased. With these improvements, highest-resolution NC-AFM imaging became possible and true atomic resolution on insulating samples is now accessible on a routine basis.
In cooperation with P. Rahe, a recipe was developed to correct the obtained images for linear vertical and lateral drift.

In the following chapter, I reported on contrast formation in NC-AFM imaging of the pristine titania (110) surface at the atomic scale.
First, the two well-established contrast modes, namely hole mode and protrusion mode were reproduced. These modes are explained by imaging the surface in a purely electrostatic manner. Thus, neither hole nor protrusion mode is capable of imaging all surface species at the same time. Furthermore, I presented images in the so-called neutral mode. Here, for the first time, single and double hydroxyls as well as vacancies could be investigated in this mode. The appearance of the surface in neutral mode resembles the real topography of the rutile surface. This points to an interaction mechanism that is mainly based on chemical forces. However, even in the neutral mode, titanium atoms are invisible.
Finally, I introduced a new contrast mode - the all-inclusive mode. In this new contrast mode, all surface atoms were imaged simultaneously. The surface appearance closely resembles the real topography, pointing to a purely chemical contrast formation mechanism. For the first time, titanium as well as bridging and in-plane oxygen could be distinguished from a single scanning probe microscopy frame. Besides, also all typical defect species are distinguishable. Additional subsurface impurities are imaged at the same time. It became obvious from the all-inclusive images that, in contradiction to former assumptions, this defect type does not originate from charge patches.
Neutral and all-inclusive mode were found to be closely related as numerous contrast changes from one to the other were observed. A cooperation with C. González, P. Jelínek[1] and R. Pérez[2] was started to model reliable pairs of tips by density-functional theory

---

[1] both from the Institute of Physics, Academy of Sciences of the Czech Republic, Prague, Czech Republic

[2] Departamento de Física Teórica de la Materia Condensada, Universidad Autónoma de Madrid, Spain

calculations, which are related by a very likely transition and give the right neutral and all-inclusive contrast, respectively.

In the last chapter, the influence of transition-metal dopants, namely chromium and antimony on the surface structure of $TiO_2(110)$ was reported. Chromium doping is known to sensitize titania to visible-light absorption. Thus, this system is interesting for photocatalytic applications. Although Cr^{3+} cations are supposed to be solely responsible for the band gap reduction of titania, only titania codoped with chromium and antimony has been found to be photocatalytically active.
In a first approach, a chromium-doped titania sample was investigated. I observed the surface lattice of the (110) surface to be very similar to that of pristine titanium dioxide. Nevertheless, two main differences were observed: First, a number of stripe-like features centered on top of the titanium rows and aligned in [001] direction were seen, which I assigned to Cr_2O_3. Second, I found experimental evidence for a drastically increased density of oxygen vacancies compared to pristine TiO_2, indicating that oxygen vacancies are created during the calcination process. A simple model was presented that is based on reducing lattice stress while maintaining charge neutrality at the same time. The model explains the creation of vacancies to be necessary for compensating the small ionic radius of Cr^{6+} species.
In the next step, I investigated the rutile titania surface, codoped with chromium and antimony. The NC-AFM images revealed a very rough surface, consisting of numerous atomically flat facets of very small size. Although the majority of facets was found to be oriented in [110] direction, several facets were identified revealing a tilted surface normal vector. True atomic resolution was obtained on nearly all facets. The defect density was found to be identical to what is observed on an equally treated pristine surface. Additional charge transfer resulting in vacancy creation as observed in chromium-doped $TiO_2(110)$ was not found here. The surface unit cell of the codoped sample was observed to be sheared with respect to the unit cell of rutile titania, closely resembling a (1×4) reconstruction. This reconstruction indicates a firm integration of antimony and chromium atoms into the lattice structure. The shearing could be explained by comparing the covalent radii of the dopant atoms with that of titanium. Hence, the observed reconstruction can be understood as a strategy to compensate for the significantly smaller covalent radii of the dopant atoms. Stress between the surface layer and underlying layers, which can be expected from this reconstruction might explain why no extended terraces were observed.
For comparison, I additionally studied the surface structure of antimony-doped $TiO_2(110)$. The surface was found to exhibit terraces, steps and a row pattern as observed on pristine titania. Upon vacuum annealing, antimony was found to seggregate to the surface, forming seggregation channels that appear as nanosized volcanos. Erupted material either forms new islands around the holes resulting in a volcano-like appearance or adsorbes as clusters on top of the surface forming an adsorbate layer. All findings draw a picture of weakly integrated antimony due to its too large ionic radius. As a matter of principle, this cannot be compensated by a similar strategy as described for the chromium-doped system. Nevertheless, it seems to be possible to create nanosized holes in a controlled way by tuning the annealing parameters of antimony-doped $TiO_2(110)$. This might be an appropriate strategy for creating nano-patterned surfaces with macroscopic techniques.

This work demonstrates that NC-AFM is capable of true atomic resolution, even on rough and highly corrugated surfaces. The present thesis, thus, constitutes a step towards investigating more realistic, application-oriented systems using NC-AFM, revealing detailed insights into the implications of transition-metal doping on the surface structure of $TiO_2(110)$.

References

[1] U. Diebold: The surface science of titanium dioxide.
Surface Science Reports **48**, 53 (2003)

[2] A. L. Linsebigler, G. Lu, J. T. Yates: Photocatalysis on TiO_2 Surfaces: Principles, Mechanisms, and Selected Results.
Chemical Reviews **95**, 735 (1995)

[3] B. O'Regan M. Grätzel: A low-cost, high-efficiency solar cell based on dye-sensitized colloidal TiO_2 films.
Nature **353**, 737 (1991)

[4] A. Fujishima K. Honda: Electrochemical photolysis of water at a semiconductor electrode.
Nature **238**, 37 (1972)

[5] C. L. Pang, S. A. Haycock, H. Raza, P. W. Murray, G. Thornton: Added row model of $TiO_2(110)$ 1×2.
Physical Review B **58**, 1586 (1998)

[6] G. S. Rohrer, V. E. Henrich, D. A. Bonnell: Structure of the Reduced $TiO_2(110)$ Surface Determined by Scanning Tunneling Microscopy.
Science **250**, 1239 (1990)

[7] U. Diebold, J. F. Anderson, K.-O. Ng, D. Vanderbilt: Evidence for the Tunneling Site on Transition-Metal Oxides: $TiO_2(110)$.
Physical Review Letters **77**, 1322 (1996)

[8] K.-I. Fukui, H. Onishi, Y. Iwasawa: Atom-Resolved Image of the $TiO_2(110)$ Surface by Noncontact Atomic Force Microscopy.
Physical Review Letters **79**, 4202 (1997)

[9] S. Wendt, R. Schaub, J. Matthiesen, E. K. Vestergaard, E. Wahlstroem, M. D. Rasmussen, P. Thostrup, L. M. Molina, E. Laegsgaard, I. Stensgaard, B. Hammer, F. Besenbacher: Oxygen vacancies on $TiO_2(110)$ and their interaction with H_2O and O_2: A combined high-resolution STM and DFT study.
Surface Science **598**, 226 (2005)

[10] J. V. Lauritsen, A. S. Foster, G. H. Olesen, M. C. Christensen, A. Kühnle, S. Helveg, J. R. Rostrup-Nielsen, B. S. Clausen, M. Reichling, F. Besenbacher: Chemical identification of point defects and adsorbates on a metal oxide surface by atomic force microscopy.
Nanotechnology **17**, 3436 (2006)

[11] H. Onishi, A. Sasahara, H. Uetsuka, T. A. Ishibashi: Molecule-dependent topography determined by noncontact atomic force microscopy: carboxylates on TiO_2 (110).
Applied Surface Science **188**, 257 (2002)

[12] Z. Zhang, O. Bondarchuk, J. M. White, B. D. Kay, Z. Dohnlek: Imaging Adsorbate O-H Bond Cleavage: Methanol on TiO_2(110).
Journal of the American Chemical Society **128**, 4198 (2006)

[13] M. Bowker: The surface structure of titania and the effect of reduction.
Current Opinion in Solid State and Materials Science **10**, 153 (2006)

[14] G. Binnig, C. F. Quate, C. Gerber: Atomic Force Microscope.
Physical Review Letters **56**, 930 (1986)

[15] S. Morita, R. Wiesendanger, E. Meyer: Noncontact Atomic Force Microscopy.
Springer, Berlin (2002)

[16] T. R. Albrecht, P. Grütter, D. Horne, D. Rugar: Frequency-Modulation Detection Using High-Q Cantilevers for Enhanced Force Microscope Sensitivity.
Journal of Applied Physics **69**, 668 (1991)

[17] F. J. Giessibl: Forces and frequency shifts in atomic-resolution dynamic-force microscopy.
Physical Review B **56**, 16010 (1997)

[18] M. Reichling C. Barth: Scanning force imaging of atomic size defects on the CaF_2(111) surface.
Physical Review Letters **83**, 768 (1999)

[19] W. Allers, A. Schwarz, U. D. Schwarz, R. Wiesendanger: Dynamic scanning force microscopy at low temperatures on a van der Waals surface: graphite(0001).
Applied Surface Science **140**, 247 (1999)

[20] H. Hölscher, W. Allers, U. D. Schwarz, A. Schwarz, R. Wiesendanger: Interpretation of "true atomic resolution" images of graphite (0001) in noncontact atomic force microscopy.
Physical Review B **62**, 6967 (2000)

[21] J. N. Israelachvili: Intermolecular & Surface Forces. Academic Press Inc, London (1994)

[22] U. Zerweck, C. Loppacher, T. Otto, S. Grafstrom, L. M. Eng: Accuracy and resolution limits of Kelvin probe force microscopy.
Physical Review B **71**, 125424 (2005)

[23] F. J. Giessibl: Advances in atomic force microscopy.
Reviews of Modern Physics **75**, 949 (2003)

[24] R. Pérez, I. Štich, M. C. Payne, K. Terakura: Surface-tip interactions in noncontact atomic-force microscopy on reactive surfaces: Si(111).
Physical Review B **58**, 10835 (1998)

[25] P. Rahe, R. Bechstein, J. Schütte, F. Ostendorf, A. Kühnle: Repulsive interaction and contrast inversion in noncontact atomic force microscopy imaging of adsorbates.
Physical Review B **77**, 195410 (2008)

[26] C. Loppacher, R. Bennewitz, O. Pfeiffer, M. Guggisberg, M. Bammerlin, S. Schär, V. Barwich, A. Baratoff, E. Meyer: Experimental aspects of dissipation force microscopy.
Physical Review B **62**, 13674 (2000)

[27] G. Meyer N. M. Amer: Novel optical approach to atomic force microscopy.
Applied Physics Letters **53**, 1045 (1988)

[28] G. Meyer N. M. Amer: Erratum: Novel optical approach to atomic force microscopy.
Applied Physics Letters **53**, 2400 (1988)

[29] S. Torbrügge: Structure and reactivity of the oxide surfaces $CeO_2(111)$ and ZnO(0001) studied by dynamic scanning force microscopy. PhD thesis, Universität Osnabrück (2008)

[30] F. J. Giessibl: Atomic resolution of the silicon (111)-(7x7) surface by atomic force microscopy.
Science **267**, 68 (1995)

[31] U. Dürig, H. R. Steinauer, N. Blanc: Dynamic force microscopy by means of the phase-controlled oscillator method.
Journal of Applied Physics **82**, 3641 (1997)

[32] F. J. Giessibl, H. Bielefeldt, S. Hembacher, J. Mannhart: Calculation of the optimal imaging parameters for frequency modulation atomic force microscopy.
Applied Surface Science **140**, 352 (1999)

[33] T. Fukuma, T. Ichii, K. Kobayashi, H. Yamada, K. Matsushige: True-molecular resolution imaging by frequency modulation atomic force microscopy in various environments.
Applied Physics Letters **86**, 034103 (2005)

[34] S. Torbrügge, J. Lübbe, L. Tröger, M. Cranney, T. Eguchi, Y. Hasegawa, M. Reichling: Improvement of a dynamic scanning force microscope for highest resolution imaging in ultrahigh vacuum.
Review of Scientific Instruments **79**, 083701 (2008)

[35] P. Rahe: Adsorptionseigenschaften von organischen Molekülen auf Titandioxid untersucht mit hochauflösender Rasterkraftmikroskopie. Diplomarbeit, Universität Osnabrück (2008)

[36] T. Albaret, F. Finocchi, C. Noguera: First principles simulations of titanium oxide clusters and surfaces.
Faraday Discussions **114**, 285 (1999)

[37] S. Wendt, P. T. Sprunger, E. Lira, G. K. H. Madsen, Z. S. Li, J. O. Hansen, J. Matthiesen, A. Blekinge-Rasmussen, E. Laegsgaard, B. Hammer, F. Besenbacher: The role of interstitial sites in the Ti3d defect state in the band gap of Titania.
Science **320**, 1755 (2008)

[38] O. Bikondoa, C. L. Pang, R. Ithnin, C. A. Muryn, H. Onishi, G. Thornton: Direct visualization of defect-mediated dissociation of water on TiO_2(110).
Nature Materials **5**, 189 (2006)

[39] Z. Zhang, O. Bondarchuk, B. D. Kay, J. M. White, Z. Dohnalek: Imaging water dissociation on TiO_2(110): Evidence for inequivalent geminate OH groups.
Journal of Physical Chemistry B **110**, 21840 (2006)

[40] J. Schütte, R. Bechstein, P. Rahe, H. Langhals, M. Rohlfing, A. Kühnle: Imaging perylene derivatives on rutile TiO_2(110) by non-contact atomic force microscopy.
accepted for publication in Physical Review B

[41] C. L. Pang, H. Raza, S. A. Haycock, G. Thornton: Imaging reconstructed TiO_2 surfaces with non-contact atomic force microscopy.
Applied Surface Science **157**, 233 (2000)

[42] H. Onishi Y. Iwasawa: Reconstruction of TiO_2(110) surface: STM study with atomic-scale resolution.
Surface Science **313**, L783 (1994)

[43] R. A. Bennett, P. Stone, N. J. Price, M. Bowker: Two (1×2) Reconstructions of TiO_2(110): Surface Rearrangement and Reactivity Studied Using Elevated Temperature Scanning Tunneling Microscopy.
Physical Review Letters **82**, 3831 (1999)

[44] G. H. Enevoldsen, A. S. Foster, M. C. Christensen, J. V. Lauritsen, F. Besenbacher: Noncontact atomic force microscopy studies of vacancies and hydroxyls of TiO_2(110): Experiments and atomistic simulations.
Physical Review B **76**, 205415 (2007)

[45] M. Batzill, K. Katsiev, D. J. Gaspar, U. Diebold: Variations of the local electronic surface properties of TiO_2(110) induced by intrinsic and extrinsic defects.
Physical Review B **66**, 235401 (2002)

[46] A. Fujishima, T. N. Rao, D. A. Tryk: Titanium dioxide photocatalysis.
Journal of Photochemistry and Photobiology C: Photochemistry Reviews **1**, 1 (2000)

[47] A. Kudo, R. Niishiro, A. Iwase, H. Kato: Effects of doping of metal cations on morphology, activity, and visible light response of photocatalysts.
Chemical Physics **339**, 104 (2007)

[48] H. Kato A. Kudo: Photocatalytic water splitting into H_2 and O_2 over various tantalate photocatalysts.
Catalysis Today **78**, 561 (2003)

[49] K. Maeda, K. Teramura, D. L. Lu, T. Takata, N. Saito, Y. Inoue, K. Domen: Photocatalyst releasing hydrogen from water - Enhancing catalytic performance holds promise for hydrogen production by water splitting in sunlight.
Nature **440**, 295 (2006)

[50] X. Chen S. S. Mao: Titanium Dioxide Nanomaterials: Synthesis, Properties, Modifications, and Applications.
Chemical Reviews **107**, 2891 (2007)

[51] H. Irie, Y. Watanabe, K. Hashimoto: Carbon-doped Anatase TiO_2 Powders as a Visible-light Sensitive Photocatalyst.
Chemistry Letters **32**, 772 (2003)

[52] R. Asahi, T. Morikawa, T. Ohwaki, K. Aoki, Y. Taga: Visible-Light Photocatalysis in Nitrogen-Doped Titanium Oxides.
Science **293**, 269 (2001)

[53] A. M. Czoska, S. Livraghi, M. Chiesa, E. Giamello, S. Agnoli, G. Granozzi, E. Finazzi, C. Di Valentin, G. Pacchioni: The Nature of Defects in Fluorine-Doped TiO_2.
Journal of Physical Chemistry C **112**, 8951 (2008)

[54] L. Lin, W. Lin, Y. Zhu, B. Zhao, Y. Xie: Phosphor-doped Titania - a Novel Photocatalyst Active in Visible Light.
Chemistry Letters **34**, 284 (2005)

[55] T. Ohno, T. Mitsui, M. Matsumura: Photocatalytic Activity of S-doped TiO_2 Photocatalyst under Visible Light.
Chemistry Letters **32**, 364 (2003)

[56] O. Diwald, T. L. Thompson, T. Zubkov, E. G. Goralski, S. D. Walck, J. J. T. Yates: Photochemical Activity of Nitrogen-Doped Rutile $TiO_2(110)$ in Visible Light.
Journal of Physical Chemistry B **108**, 6004 (2004)

[57] N. Serpone: Is the Band Gap of Pristine TiO_2 Narrowed by Anion- and Cation-Doping of Titanium Dioxide in Second-Generation Photocatalysts?
Journal of Physical Chemistry B **110**, 24287 (2006)

[58] S. Livraghi, M. C. Paganini, E. Giamello, A. Selloni, C. Di Valentin, G. Pacchioni: Origin of Photoactivity of Nitrogen-Doped Titanium Dioxide under

Visible Light.
Journal of the American Chemical Society **128**, 15666 (2006)

[59] A. Di Paola, G. Marcì, L. Palmisano, M. Schiavello, K. Uosaki, S. Ikeda, B. Ohtani: Preparation of Polycrystalline TiO_2 Photocatalysts Impregnated with Various Transition Metal Ions: Characterization and Photocatalytic Activity for the Degradation of 4-Nitrophenol.
Journal of Physical Chemistry B **106**, 637 (2002)

[60] T. Ikeda, T. Nomoto, K. Eda, Y. Mizutani, H. Kato, A. Kudo, H. Onishi: Photoinduced dynamics of TiO_2 doped with Cr and Sb.
Journal of Physical Chemistry C **112**, 1167 (2008)

[61] H. Kato A. Kudo: Visible-light-response and photocatalytic activities of TiO_2 and $SrTiO_3$ photocatalysts codoped with antimony and chromium.
Journal of Physical Chemistry B **106**, 5029 (2002)

[62] J. Pascual, J. Camassel, H. Mathieu: Fine structure in the intrinsic absorption edge of TiO_2.
Physical Review B **18**, 5606 (1978)

[63] R. D. Shannon: Revised Effective Ionic-Radii and Systematic Studies of Interatomic Distances in Halides and Chalcogenides.
Acta Crystallographica Section A **32**, 751 (1976)

[64] A. L. Allred: Electronegativity values from thermochemical data.
Journal of Inorganic & Nuclear Chemistry **17**, 215 (1961)

[65] B. Cordero, V. Gomez, A. E. Platero-Prats, M. Reves, J. Echeverria, E. Cremades, F. Barragan, S. Alvarez: Covalent radii revisited.
Dalton Transactions **21**, 2832 (2008)

Publications

The results from the present thesis are or will be published in the following articles:

- R. Bechstein, M. Kitta, J. Schütte, A. Kühnle, H. Onishi: Evidence for vacancy creation by chromium doping of rutile titanium dioxide (110).
  accepted for publication in Journal of Physical Chemistry C
- R. Bechstein, M. Kitta, J. Schütte, H. Onishi, A. Kühnle: Surface reconstruction induced by transition metal doping of TiO_2(110).
  submitted to Journal of the American Chemical Society
- R. Bechstein, C. González, P. Jelínek, J. Schütte, R. Pérez, A. Kühnle: ”All-inclusive” imaging of TiO_2(110) with NC-AFM.
  to be submitted to Physical Review Letters
- R. Bechstein, M. Kitta, J. Schütte, H. Onishi, A. Kühnle: Creation of nanoscopic pits by antimony doping of titania.
  to be submitted to Nanotechnology
- P. Rahe, R. Bechstein, A. Kühnle: Vertical and lateral drift correction of SPM images.
  in preparation

Furthermore, I substantially contributed to the following publications:

- P. Rahe, R. Bechstein, J. Schütte, F. Ostendorf, A. Kühnle: Repulsive interaction and contrast inversion in non-contact atomic force microscopy imaging of adsorbates.
  Physical Review B **77**, 195410 (2008)
- F. Loske, R. Bechstein, J. Schütte, F. Ostendorf, M. Reichling, A. Kühnle: Growth of ordered C_{60} islands on TiO_2(110).
  accepted for publication in Nanotechnology
- J. Schütte, R. Bechstein, P. Rahe, M. Rohlfing, H. Langhals, A. Kühnle: Imaging perylene derivatives on rutile TiO_2(110) by non-contact atomic force microscopy.
  accepted for publication in Physical Review B

Conference contributions

Talks[3]

- R. Bechstein, C. González, P. Jelínek, R. Pérez, A. Kühnle: "All-inclusive" imaging of titania.
  NC-AFM 2008, Madrid (Spain)
- P. Rahe, R. Bechstein, J. Schütte, F. Ostendorf, F. Loske, A. Kühnle: Repulsive interaction and contrast inversion in NC-AFM imaging of adsorbates.
  NC-AFM 2008, Madrid (Spain)
- R. Bechstein, J. Schütte, P. Rahe, A. Kühnle: Unravelling molecular contrast formation obtained by NC-AFM on titania.
  AVS 2007, Seattle (USA)
- R. Bechstein, J. Schütte, P. Rahe, A. Kühnle: High-resolution imaging of individual perylene derivatives on titania.
  NC-AFM 2007, Antalya (Turkey)
- R. Bechstein, J. Schütte, A. Kühnle: Understanding and controlling molecular interactions in self-assembly on dielectric surfaces.
  Workshop on Atomic Force Microscopy 2006, Osaka, (Japan)

Posters

- R. Bechstein, J. Schütte, P. Rahe, A. Kühnle: Unravelling molecular contrast formation obtained by NC-AFM.
  TRNM 2007, Levi (Finland)
- J. Schütte, R. Bechstein, P. Rahe, A. Kühnle: Diffusion and manipulation of perylene derivatives on TiO_2.
  NC-AFM 2007, Antalya (Turkey)
- P. Rahe, R. Bechstein, A. Kühnle: Contrast reversal of protruding adsorbates in NC AFM.
  NC-AFM 2007, Antalya (Turkey)

---

[3] presenting author is underlined

Acknowledgement

This thesis would not have been possible without the help of a number of people. Hereby, I like to thank them for their contribution.

- First of all, I owe special thanks to my supervisor **Angelika Kühnle**. You provided an exciting topic as well as an inspiring atmosphere. It was a pleasure to be your PhD student.
- A very special thank goes to **Rubén Pérez** from the Universidad Autónoma de Madrid, who accepted to be 2nd referee for my thesis and takes it upon himself to come to Osnabrück to examine my defence.
- I thank **Joachim Wollschläger** and **Johann P. Klare** who also agreed to become examiners of my defence.

During my studies, I had the honor to collaborate with

- **Hiroshi Onishi** and **Mitsunori Kitta** from Kobe University who had been so kind to provide me the doped titania samples and were available for fruitful discussions on photocatalysis.

and

- **Pavel Jelínek** and **César González** from the Academy of Sciences of the Czech Republic who decided to model the tip-sample interaction on pristine titania and spent numerous hours on discussing contrast formation mechanisms and tip stability.

I thank my colleagues **Jens Schütte** and **Philipp Rahe** for the pleasant working environment, endless hours of fruitful and stimulating discussions on NC-AFM experiment and theory, critical review of manuscripts and talks as well as answering countless questions on Latex and computer stuff in general. I owe a special thank to Jens for the cooperation on titania, for being an expert in glueing cantilevers and knowing almost everything about UHV systems. A special thank goes to Philipp for his incredible efforts in introducing Gwyddion, his input to the drift correction recipes and all kinds of ”bin-gleich-fertig” calculations and simulations.

I thank **Werner Schniederberend** and **Dirk Rathmann** for the design and construction of the new preamplifier and various other devices as well as for patient instructions to the world of electronics.

I thank all members of the groups Molecular Self-Assembly and Nanoscience for the nice working atmosphere, for entertaining excursions and conferences and for lending a hand whenever necessary. Especially, I thank **Frank Ostendorf** and **Lutz Tröger** who answered numerous questions on NC-AFM technical stuff. Special thanks to Lutz for his Latex template. I thank **Sebastian Rode** for his assistance on the spectral noise density measurement and **Felix Loske** for providing his bibstyle. Very special thanks go to **Frauke Riemann** and **Wilhelm Koslowski** for their quick and easy assistance with all kinds of administrative and technical problems, respectively.

Diese Arbeit wäre nicht möglich gewesen ohne die Unterstützung meiner Familie. Ich danke vor allem meiner Frau Stefanie dafür, daß sie Nachsicht hatte, wenn es mal wieder länger gedauert hat. Die letzten Wochen waren ein echter Härtetest. Ich danke dir, unserem Sohn Justus, Uwe und allen Freunden, die wir hier in Osnabrück gefunden haben dafür, daß sie den nötigen Ausgleich ermöglicht haben für die vielen Stunden im Labor und am Schreibtisch.
Nicht zuletzt danke ich meinen Eltern, die mich ermutigt und unterstützt haben und mir jede Möglichkeit der freien Entfaltung gegeben haben. Ohne euch wäre ich nie soweit gekommen.